Doctoral Thesis in Physics

Ab initio to Application:

Antiferromagnetic Heusler Compounds for Spintronics

Jan Balluff

1st September 2017

Bielefeld University
Department of Physics
Center for Spinelectronic Materials and Devices

Declaration

I wrote this thesis by myself and used none but the indicated resources. Text and figures were partly taken from corresponding publications, which originate directly from this work.

(Jan Balluff)

Reviewers:

Prof. Dr. Günter Reiss

Prof. Dr. Thomas Dahm

Written in LaTeX 2$_\varepsilon$ and KOMA-Script, typeface Charter 10 pt.
Printed on non-aging paper ISO 9706
Bielefeld University, Department of Physics
Center for Spinelectronic Devices and Materials

Doctoral thesis
1st September 2017

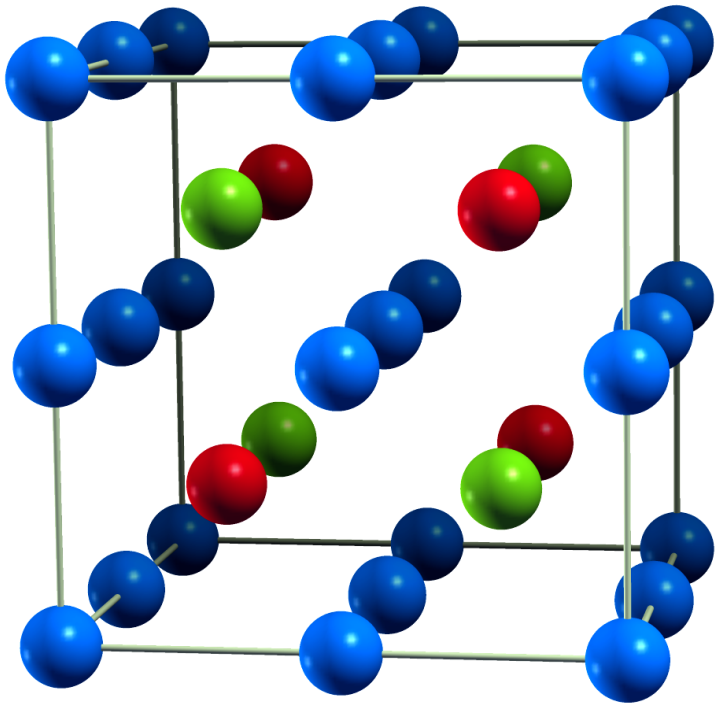

Structure of a Heusler compound

They [antiferromagnets] are extremely interesting from the theoretical viewpoint, but do not seem to have any applications.

— Louis Néel

Publications

- *Exchange bias in epitaxial and polycrystalline thin film Ru_2MnGe / Fe bilayers*
  J. Balluff, M. Meinert, J. M. Schmalhorst, G. Reiss, and E. Arenholz
  J. Appl. Phys. **118**, 243907 (2016).
  doi:10.1063/1.4939092

- *High-throughput screening for antiferromagnetic Heusler compounds using density functional theory*
  J. Balluff, K. Diekmann, M. Meinert, and G. Reiss
  Phys. Rev. Materials **1**, 034404 (2017).
  doi:10.1103/PhysRevMaterials.1.034404

- *Integration of antiferromagnetic Heusler compound Ru_2MnGe into spintronic devices*
  J. Balluff, T. Huminiuc, M. Meinert, A. Hirohata, and G. Reiss
  Appl. Phys. Lett. **111**, 032406 (2017).
  doi:10.1063/1.4985179 , arXiv:1705.08420

- *Enhancing magnetic properties in Mn_3Ge thin films by doping*
  J. Balluff, M. Meinert, J. M. Schmalhorst, E. Arenholz, and G. Reiss
  In preparation (2017).

Conference contributions

Presenting author is marked with a •.

- **03 / 2014** *Growth and magnetic properties of Heusler alloy type Ru_2MnZ (Z=Ge, Si) thin films*
  • J. BALLUFF, M. MEINERT, AND G. REISS
  Frühjahrstagung der deutschen physikalischen Gesellschaft, Dresden, Germany, Poster MA 55.93

- **03 / 2015** *High-throughput screening for antiferromagnetic Heusler compounds using density functional theory*
  • J. BALLUFF, M. MEINERT, AND G. REISS
  Frühjahrstagung der deutschen physikalischen Gesellschaft, Berlin, Germany, Talk MA 3.2

- **03 / 2015** *Exchange bias in antiferromagnetic Heusler alloy Ru_2MnGe thin films*
  • J. BALLUFF, M. MEINERT, AND G. REISS
  Frühjahrstagung der deutschen physikalischen Gesellschaft, Berlin, Germany, Poster MA 49.25

- **01 / 2016** *Exchange Bias Studies in Heusler Alloy Structures*
  • T. HUMINIUC, J. BALLUFF, M. MEINERT, G. REISS, AND A. HIROHATA
  13th Joint MMM-Intermag Conference, San Diego, CA (U.S.), Poster FR-14

- **03 / 2016** *High-throughput screening for antiferromagnetic Heusler alloys using density functional theory*
  • J. BALLUFF, M. MEINERT, AND G. REISS
  Frühjahrstagung der deutschen physikalischen Gesellschaft, Regensburg, Germany, Poster MA 17.60

- **03 / 2016** *Exchange bias in Heusler compound Ru_2MnGe / Fe bilayers*
  • J. BALLUFF, M. MEINERT, J. M. SCHMALHORST, G. REISS, AND E. ARENHOLZ
  Frühjahrstagung der deutschen physikalischen Gesellschaft, Regensburg, Germany, Poster MA 41.4

- **05 / 2016** *Heusler compounds for spintronic applications*
  A. NIESEN, M. GLAS, • J. BALLUFF, M. MÜNZENBERG, AND G. REISS
  5th HARFIR Open Workshop, Konstanz, Germany, Talk
- **09 / 2016** *Novel materials for antiferromagnetic spintronics*
  J. BALLUFF, K. DIEKMANN, G. REISS, AND • M. MEINERT
  SPICE Workshop on Antiferromagnetic Spintronics, Mainz, Germany, Poster
- **11 / 2016** *High-throughput screening for antiferromagnetic Heusler compounds using density functional theory*
  • J. BALLUFF, K. DIEKMANN, M. MEINERT, AND G. REISS
  61st Conference on Magnetism and Magnetic Materials, New Orleans, LA (U.S.), Talk FC-14
- **11 / 2016** *Antiferromagnetic Ru_2MnGe Heusler compound as a pinning layer for exchange bias devices*
  • J. BALLUFF, M. MEINERT, J. M. SCHMALHORST, E. ARENHOLZ AND G. REISS
  61st Conference on Magnetism and Magnetic Materials, New Orleans, LA (U.S.), Poster GS-05
- **11 / 2016** *Novel materials for antiferromagnetic spintronics*
  • J. BALLUFF, K. DIEKMANN, G. REISS, AND M. MEINERT
  SPR-KKR Hands on Course, Daresbury, England, Poster
- **03 / 2017** *Doping of perpendicularly magnetized ferrimagnetic Mn_3Ge thin films*
  • J. BALLUFF, M. MEINERT, AND G. REISS
  Frühjahrstagung der deutschen physikalischen Gesellschaft, Dresden, Germany, Poster MA 65.24
- **03 / 2017** *Novel materials for antiferromagnetic spintronics*
  J. BALLUFF, • K. DIEKMANN, G. REISS, AND M. MEINERT
  Frühjahrstagung der deutschen physikalischen Gesellschaft, Dresden, Germany, Poster MA 66.19
- **04 / 2017** *Doping of perpendicularly magnetized ferrimagnetic Mn_3Ge thin films*
  J. BALLUFF, • M. MEINERT, AND G. REISS
  IEEE International Magnetics Conference, Dublin, Ireland, Poster GO-11

Contents

1 Introduction

Spintronics - this is a compound word made of *spin* and *electronics*. Most of us are quite familiar with the latter: It accompanies our everyday life in many facets. We connect *electronics* with *electricity*, e.g. anything we plug in into a socket, like a coffee maker or a television. Electronics is about creation and control of electron currents via their charge, in other words *charge currents*.

The *spin*, however, is rather less known in general. Just like the charge, it is an intrinsic property of the electron, which for a long time no practical use was made of in electronics. Hence, it is suggestive to investigate the interplay between electrical currents and the electron's spin. Directly connected to the spin is a magnetic moment, which is sensitive to magnetic fields. In addition to the electric charge of the electron, the spin gives us another option to externally manipulate charge currents.

Today, the spin is crucial for some of our technologies, such as hard disc drives [1]. Here, information is stored on magnetic discs. A read-write head floats in close proximity to the magnetic layer, not touching it. The magnetic layer creates a small, but detectable magnetic field for the read head. This affects the electrical currents in the read head, which can be detected by electronics connected to it. This complex interplay between charge, spin (respectively the resulting magnetic moment), and corresponding currents we call *spintronics* [2–4]. We will discuss fundamentals of spintronics, the underlying effects and the functional principles of spintronic devices in Chapter 2.

Critical Raw Materials

Much effort is put into developing new types of memory which are non-volatile, fast and efficient. Special focus is set on further miniaturization and lowering power consumption. Promising candidates can be found among spintronic devices, i.e., magnetic RAM (MRAM) [5–10]. However, these devices usually require an antiferromagnetic material. In most cases, antiferromagnets formed by compounds of platinum group metals are used, namely IrMn or PtMn [11–13]. These materials are costly and rare. Especially Iridium is among the least abundant materials in the earth's crust [14]. Therefore, its price increased by a factor of up to almost ten in the recent years as shown in Fig. 1.1 [15]. In terms of sustainability, it is crucial to find materials with comparable properties without the use of so-called *critical raw materials* [16]. Essentially, these are either highly toxic materials or materials exhibiting a supply risk due to their economic importance and/or low abundance. Hence, future supply may not be able to satisfy upcoming demands.

Especially, as the combined properties of the IrMn compound are yet unrivaled. It can be easily fabricated in thin film structures and provides excellent magnetic properties suitable for almost any kind of application [13, 17]. Furthermore, the compound has an high corrosion resistance and thermal stability. The combination of these properties makes it a challenging task to find a suitable replacement, especially avoiding critical raw materials. For example, Meinert *et al.* recently showed [18] that the antiferromagnetic MnN compound is a promising critical-

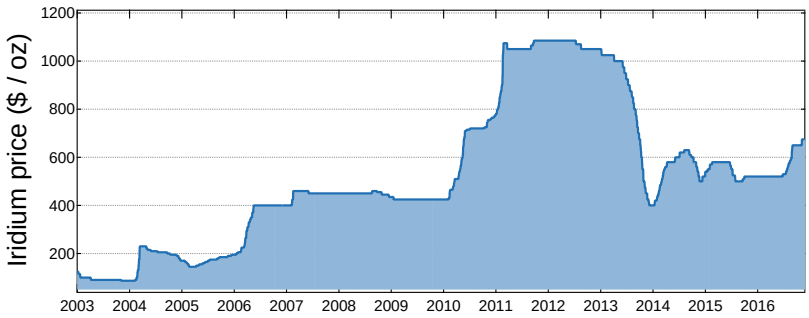

Figure 1.1. | Iridium price in $ per ounce from 2003 to 2016 [15]

material-free candidate. However, the minimum thickness, below which an application in spintronic devices is not possible, is quite high for this compound. This of course hinders miniaturization. The possible number of combinations to form *binary* compounds consisting of only two elements is limited, thus investigations among these is already quite advanced. Therefore, suitable findings among binary compounds are unlikely.

The Search for New Antiferromagnets

The major aspect of this work is to search for new antiferromagnetic materials. The *ternary* family (compounds consisting of three elements) of Heusler compounds, which is introduced in Sec. 2.3, is interesting for this task. Ternary compounds, in contrast to binary ones, lead to a huge number of possible element combinations. Hence, a suitable, systematic approach is required. From a theoretical point of view, it is possible to cope with that by means of automatic processing. On the experimental side, it is nearly impossible to check every combination manually. Therefore, a combination of theoretical work predicting materials with the desired ground state and experimental work checking this for selected candidates is the method of choice.

In the first part of this work we deal with the screening for antiferromagnetic Heusler compounds. We do this using density functional theory, which provides us the tools to theoretically investigate ground state properties of compounds. The specific methods we are using are introduced in Chapter 3. The results of this investigation predict 70 novel antiferromagnetic Heusler compounds which are presented in Chapter 5.

Experimental Investigation

One of the candidates predicted by the screening is the Ru_2MnGe Heusler compound. It was previously predicted to be antiferromagnetic [19], which was experimentally confirmed. The compound has a rather high Néel temperature slightly above room temperature, where the absolute measured values in the literature vary from $T_N = 295\,K$ to $353\,K$ [20–22]. This makes it interesting for spintronic applications. We further investigate the compound extending the

work already published, checking for temperature dependencies and applicability in spintronic devices.

The experimental methods used to prepare and analyze thin film samples and devices are outlined in Chapter 4. The synthesis and characterization of Ru_2MnGe thin films is dealt with in Chapter 6. Finally, we demonstrate the integration of this material into spintronic devices. To the best of our knowledge, this is the first report on a working spin valve device using an antiferromagnetic Heusler compound.

Alternative Materials

The "pinning" of a ferromagnetic layer in spintronic devices mediated by an antiferromagnet can also be achieved, e.g., by coupling it to another ferro- or ferrimagnetic material exhibiting a giant coercivity. Due to this, such bilayers provide similar properties as the commonly used ferromagnet-antiferromagnet systems. The Heusler-related ferrimagnetic system Mn_3Ge is such a system recently investigated [23–25]. It exhibits a large coercivity of more than 2 T which makes it interesting for this application. Its low saturation magnetization reduces stray fields, and in addition, the material has a perpendicular anisotropy. Perpendicularly magnetized systems are especially interesting for applications. Furthermore, Mn_3Ge does not contain any platinum group or rare earth metals. Improving its properties may make this system an interesting alternative to common spintronic systems based on antiferromagnets.

We investigate the Mn_3Ge compound in Chapter 7. Using density functional theory, we predict changes in its magnetic structure caused by doping with different elements. We check these predictions by experimentally preparing and investigating samples with the most promising dopants.

2 Fundamentals

Antiferromagnetic (AF) materials are often subtly hidden, as they are almost magnetically "invisible" due to their zero net magnetization. Yet they build the fundamental basis for spintronics as a pinning layer used to create a ferromagnetic (F) reference of fixed magnetization orientation [26, 27]. In the following we will discuss the underlying effect, the *exchange bias*. This effect has been known for many decades, but the microscopic mechanisms are not yet fully understood. Different kind of theories have been developed coping with several, but not all aspects at once. Nevertheless, the effect is of immense commercial relevance.

Already known for a long time [28], magnetic conductors exhibit a resistance which is dependent on their magnetic configuration. This is externally manipulable by magnetic fields, which allows a magnetoresistive device to be built. The *magnetoresistance* (MR) is a fundamental aspect of modern data storage technology. Today, there are many different kinds of magnetoresistive effects known, which will be discussed briefly. Since the discovery of the giant magnetoresistance by Fert and Grünberg in 1980 [29, 30], both rewarded with the Nobel prize in 2007, the commercial relevance of such elements has rapidly increased. As modern magnetoresistive applications often exploit the exchange bias effect mediated by AFs, the demand for those has rapidly increased as well. We will discuss how the common spintronic devices are constructed as well as recent de-

velopments, underlining the relevance of AF materials. In the last part of this chapter we will outline how *Heusler compounds* are already used in spintronics and how they are interesting for material research in general, especially for this work.

2.1. Exchange Bias

The exchange bias effect is found when a F is in contact with an AF. Historically, this was first reported by Meiklejohn and Bean in 1957 [26]. They studied Co nano particles ($\sim 20\,\mathrm{nm}$), which were exposed to air and therefore oxidized at the surface. The ferromagnetic Co was coated by a layer of antiferromagnetic CoO. After cooling the nano particles below the Néel temperature of the CoO in a magnetic field, they observed a new unidirectional magnetic anisotropy, which is absent if cooled without a magnetic field. This manifests in a broadening of the hysteresis curve as well as a shift in negative field direction. This shift is commonly referred to as the exchange bias field $H_{\mathrm{ex}} = (H^+ + H^-)/2$, where H^+ and H^- are the switching fields of the hysteresis.

Phenomenology

A necessary requirement for this effect to occur is that the Curie temperature T_{C} of the F is larger than the Néel temperature T_{N} of the AF. In an intuitive picture, as reviewed by Meiklejohn [31], the exchange bias effect can be understood as follows: When heated to a temperature $T_{\mathrm{N}} < T < T_{\mathrm{C}}$, the F material is still ordered while the AF one is in a paramagnetic state. Applying a field will align the F and induce a preferred orientation for the AF order when cooled below T_{N}. After this field-cooling (FC) process, both materials are ordered and coupled in a unidirectional way. In a magnetic field sweep, the AF is hardly affected at all. The F, however, will eventually follow the magnetic field. Due to the coupling to the AF, an additional anisotropy energy is required to switch the magnetization. In the reverse process, as the anisotropy is unidirectional, the energy is gained. All in all, this results in a shift of the hysteresis loop. This simple consideration in terms of energies, however, largely overestimates the resulting H_{ex}. Furthermore, the broadening of the hysteresis curve cannot be explained this way. A huge number of experimental investigations since the discovery of

Meiklejohn and Bean revealed a much more complex phenomenology besides the hysteresis shift in various systems containing F - AF interfaces of very different magnetic, crystallographic and interfacial structures. Especially, the effect size depends on various parameters. A detailed insight for all of those can be found in the review by Nogués *et al.* in Ref. [27].

Different temperature dependencies for both H_{ex} and the coercivity H_{c} are found. Additionally, in the general case the exchange bias field H_{ex} vanishes at a temperature $T_{\mathrm{B}} < T_{\mathrm{N}}$. This temperature, the *blocking temperature*, is related to thickness, roughness, grain size, and disorder of the AF. For thick films and single crystals, however, often $T_{\mathrm{B}} \approx T_{\mathrm{N}}$ is found [27]. Moreover, the common case is not the existence of a single, well defined T_{B} but rather a distribution. In many exchange bias systems a reduction in H_{ex} is found after several consecutive hysteresis loops, which is indicative for the involvement of non-reversible processes. Although there is no general rule for this *training effect*, it is often experimentally found that the decrease is $\Delta H_{\mathrm{ex}} \propto 1/\sqrt{n}$ [32, 33], where n is the number of field loops. Typically between the initial and second loop, a significant decrease can be observed in many systems [33]. A recovery from the training effect is reported when leaving the system to relax [34], which is accounted for by thermal relaxation processes in the AF domain structure.

The effect size is affected by the layer thicknesses t_{F} and t_{AF} of the F and AF. Where the exchange bias field H_{ex} is found to be generally inversely proportional to t_{F}, a general conclusion for t_{AF} is not found. All in common, however, is a critical minimum AF thickness required to observe exchange bias. The effect size also depends on the preparation parameters, such as starting temperature of the FC, the time exposing the sample to this temperature, and the magnetic field applied during FC. In some systems, especially for large magnetic fields during FC, even an unexpected shift in the opposite direction, referred to as positive exchange bias, can be found [35]. As a common standard procedure for measuring exchange bias as proposed by O'Grady *et al.* [36] is not yet sufficiently established, a comparison of different experiments is a difficult task.

Early models

Due to this large variety of factors and phenomena, a general theory understanding all microscopic aspects of exchange bias is still lacking. In the first intuitive

picture given by Meiklejohn as discussed above, by pure energetic considerations the inverse thickness dependence of the exchange bias field H_{ex} to the F thickness t_{F} is found [31]:

$$H_{\mathrm{ex}} = \frac{J_{\mathrm{Int}}}{M_{\mathrm{F}} t_{\mathrm{F}}} \ . \tag{2.1}$$

J_{Int} is the interface coupling constant and M_{F} the saturation magnetization of the F layer. This relation inverse proportional to t_{F} indeed roughly holds for all investigated exchange bias systems [27]. A further important result is the condition $K_{\mathrm{AF}} t_{\mathrm{AF}} \geq J_{\mathrm{Int}}$ for exchange bias to occur. K_{AF} is the anisotropy of the AF layer and t_{AF} the corresponding thickness. Thus, the anisotropy of the AF plays an important role as well.

Many exchange bias models dealing with different aspects have emerged. They are well reviewed in an article by O'Grady *et al.* in Ref. [36]. Some of the key points are summarized here. A first extended model was proposed by Néel [37]. In contrast to a rigid spin model, he proposed a more realistic one by including an uncompensated AF spin structure at the interface, which is subject to deformation and reorientation in hysteresis loops. These are irreversible processes which the training effect attributes to. Domain wall models provide a more detailed consideration, first proposed by Mauri in 1987 [38]. Here, the formation of domain walls parallel to the F - AF interface is proposed. In a reorientation process of the F this results in lowering the interfacial energy. Thus, the predicted exchange bias fields H_{ex} are more accurate.

Similar predictions are found by Malozemoff in 1987 [39], who introduced a random interface roughness, which is more realistically found in real samples. Due to the roughness, compensated and uncompensated regions at the interface are found. These induce the formation of domain walls perpendicular to the interface, e.g., accounting for the critical AF thickness required to observe exchange bias. Another explanation is found by Koon in 1997 [40], who proposed a spin-flop coupling at the interface, where the spins of the F and AF align perpendicularly, but parallel to the interface. This effect induces domain walls parallel to the interface as well as a canting of spins in the AF for a few monolayers next to the interface. An investigation of Schulthess and Butler from 1998 [41] showed that for perfectly flat interfaces Koon's model does not lead to a hysteresis shift but to an increased coercivity in the F. By the introduction of defects at the interface reasonable values for H_{ex} are found as well [42].

Domain State Model

Another important theory is the domain state model by Nowak *et al.* published in the early 2000's [43–45]. They proposed that exchange bias is based on a F in contact with a *diluted* AF. The dilutions included in the AF are in the form of non-magnetic defects, which support the formation of domain walls as the necessary energy in their vicinity is reduced. During the FC process, a domain state develops and freezes throughout the cooling. Within this model, they were able to predict several exchange bias related features such as temperature dependencies and positive exchange bias. This model is mainly applicable to epitaxial, nearly single-crystal thin film systems [36].

Granular and Polycrystalline Systems

A quite successful model on granular systems is given by Fulcomer and Charap in 1972 considering different particle shapes and sizes [46, 47]. They were able to predict correct temperature dependencies of both H_{ex} and H_{c} over a wide temperature range by assuming a distribution of particle size. This idea is picked up by O'Grady *et al.* and incorporated into an extensive theory for polycrystalline thin films [36]. Changes in the AF are thermally activated, where the required activation energy is attribute to the grain size distribution. At the beginning of the FC process, the AF is set into a defined state at an adequate temperature. Depending on the grain size different temperatures are required to set the AF grains during this initial process. This allows an understanding of the distribution of the blocking temperature T_{B}: Depending on their shape and size, grains require different temperatures to be thermally activated and lose their exchange bias. They conclude that the exchange bias crucially depends on the proportion of AF grains which are thermally stable and set. In this paradigm, they are able to explain many features of exchange bias.

All in all, the exchange bias effect has a huge variety of facets beyond the shift of the hysteresis loop. They are very sensitive to the structure, geometry and material of the system. A general theory is yet not available. Theoretical models suggest that several mechanisms lead to exchange bias, where different ones dominate depending on the system. For example, in polycrystalline thin films thermal activation dependent on the grain size distribution dominates, whereas for single-crystalline films domain wall pinning is of major importance [36].

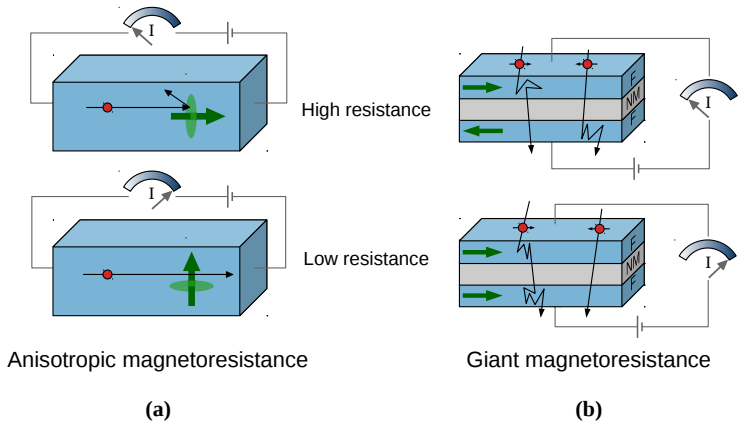

Figure 2.1. | Magnetoresistance. **(a)** AMR. Orbitals are affected by the magnetization (green arrows ⇑) due to spin-orbit coupling resulting in different scattering behavior for electrons (red dots ●). **(b)** GMR. Majority and minority electrons (indicated by arrows) are scattered differently depending on the material's relative magnetization.

2.2. Magnetoresistance & Spintronics

As already indicated, the exchange bias effect is often utilized to prepare magnetoresistive devices. Before going into detail, we will discuss some general remarks on magnetoresistive effects.

One of the longest known magnetoresistive effects is the *anisotropic magnetoresistance* (AMR), going back to Thomson (Lord Kelvin) in 1856 [28]. This effect occurs in F materials, where its electrical resistance depends on the relative orientation between its magnetization and the current direction. The AMR can be observed easily in bulk materials, however, the amplitude of the effect is rather small. Typical changes in the resistance due to the AMR are a few percent [3]. The effect arises due to spin-orbit-coupling, where the $3d$ orbitals are distorted dependent on the magnetic orientation resulting in a different scattering potential for the conduction electrons, schematically depicted in Fig. 2.1a.

Hard disc drive read heads based on the AMR, introduced by IBM in 1991, were used for many years [3]. Nowadays, however, the *giant magnetoresistance* (GMR) or *tunneling magnetoresistance* (TMR) is utilized. The GMR occurs in al-

ternating multilayers of F and non-magnetic (NM) metals. The thickness of the layers need to be of the order of the electron's spin diffusion length, i.e. the mean free path of the electron before a spin change occurs. Thus, spin-dependent electron transport can be observed in these multilayers. Due to the RKKY interaction, an antiparallel alignment of the F layers can be obtained by adjusting the NM layer thickness. Another option is the pinning to an AF via exchange bias. In the antiparallel state, spin-polarized electrons are injected from a ferromagnetic layer into another one of opposite polarization. In sum, both majority and minority electrons are scattered equally. When the F layers, however, are aligned parallel, e.g. by applying an external magnetic field, the conduction (and thus the resistance) changes as minority electrons are less scattered than majority electrons. The electron scattering for these two cases is illustrated in Fig. 2.1b. For most materials and devices, in the parallel (p) state a low resistance, and in the antiparallel (ap) state a high resistance is found, as indicated in the figure. Due to this difference in the spin-dependent conductance such devices are called spin valves. A minimal spin valve consists of a trilayer F / NM / F (as shown in Fig. 2.1b). As the GMR yields a much larger resistance change than the AMR (in the original work, changes of 80% for Fe / Cr multilayers have been found [29, 30], hence the name "giant"), GMR spin valves replaced the AMR read heads in hard disc drives in 1997 [3]. The signal amplitudes in these commercial spin valve trilayers are around 5-20%.

Tunneling Magnetoresistance

The currently most popular MR is the TMR effect due to its huge effect sizes. In *magnetic tunneling junctions* (MTJs) - spin valves based on the TMR effect - two F are separated by a thin insulating, non-magnetic barrier. Here, usually one F layer is pinned to an AF by exchange bias. With a certain probability, conduction electrons can cross the junction by tunneling, where the tunneling current is driven by a small bias voltage across the junction. This current crucially depends on the relative state of the two ferromagnetic layers F1 and F2. For the two different states the corresponding resistances are labeled R_p and R_ap. We define the TMR ratio as

$$\mathrm{TMR} = \frac{R_\mathrm{ap} - R_\mathrm{p}}{R_\mathrm{p}} \,. \tag{2.2}$$

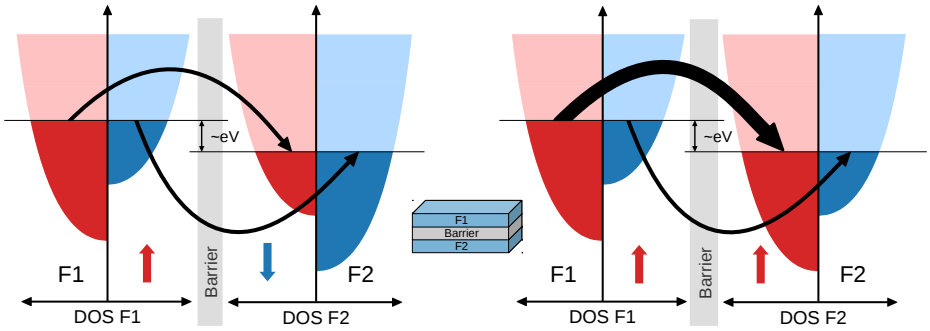

Figure 2.2. | Tunneling magnetoresistance. The DOS for the ferromagnets F1 and F2 on both sides of the barrier is plotted. Depending on the number of initial and final states the tunneling rates differ, indicated by the arrow thickness. For ap alignment the tunneling current is low (left hand side), for p alignment it is high (right hand side).

The effect was first reported by Jullière in 1975 within a Fe / Ge-O / Co multilayer showing a TMR of 14% [48]. However, it did not attract much attention. Unlike other MR effects like the GMR, which also work in current-in-plane geometry, TMR spin valves require a current-perpendicular-to-plane geometry. This, in turn, requires a complex lithographic preparation. In the early 2000's, theoretical investigations on Fe / MgO / Fe multilayers predicted TMR values exceeding 1 000% [49, 50]. Shortly after, Bowen *et al.* experimentally reported on significant TMR values of around 60% in this system [51]. The maximum TMR values found by experimentalists rapidly increased in the following years, reaching up to 600% at room temperature [52] and 2 000% at low temperatures [53].

The reason for these large effect sizes can be understood in a simple two-current model. Here, the conduction channels for majority and minority charge carriers are considered separately and a mixing is excluded. The tunneling currents depend on the density of states (DOS) of the two F. Depending on the magnetic state, more states around the Fermi level are found either in the majority or in the minority channel. In the ap state, the DOS in F1 and F2 differ for both spin species. This results in a reduced tunneling probability, as either few initial or final states are found at the Fermi level. This is sketched on the left hand side of Fig. 2.2, where the black arrows indicate the tunneling probability through the barrier. On the other hand, in the p state shown on the right hand side, for

the majority charge carriers both in F1 and F2 many states at the Fermi level are found. This results in a drastically increased tunneling current of these electrons. Obviously, the TMR effect size crucially depends on the *spin polarization*

$$P = \frac{\mathcal{D}_\uparrow(E_\mathrm{F}) - \mathcal{D}_\downarrow(E_\mathrm{F})}{\mathcal{D}_\uparrow(E_\mathrm{F}) + \mathcal{D}_\downarrow(E_\mathrm{F})} \tag{2.3}$$

of the two F layers, where $\mathcal{D}_\uparrow(E)$ is the density of states for majority or minority electrons indicated by the index and E_F is the Fermi energy. As already outlined by Jullière [48], the TMR ratio can be expressed in terms of the spin polarizations P_1, P_2 in the MTJ electrode materials by

$$\mathrm{TMR} = \frac{2P_1P_2}{1 - P_1P_2}\,. \tag{2.4}$$

Evidently, the TMR becomes infinite if both spin polarizations are 100%. In this case, the MTJ can be switched between an insulating state (infinite resistance) and conducting state (low resistance). Therefore, F materials exhibiting a high spin polarization are of increased interest for the fabrication of MTJ with large effect sizes.

Spintronics

One of the ultimate goals is a fast, non-volatile magnetic memory with low power consumption replacing current technology such as flash memory. Therefore, an electrical switching of such MR elements is required. Instead of using external magnetic fields it is possible to switch the unpinned F layer using a spin polarized current. These currents produce a *spin-transfer torque* (STT) in the unpinned layer by momentum transfer changing the magnetic orientation [54, 55]. The critical current density required to switch an unpinned layer is of the order of $10^6 - 10^8\,\mathrm{A/cm^2}$ [56]. Such densities can easily destroy the tunneling barriers, hence a wide-ranging mass production is still lacking. Nevertheless, this has been brought to a commercial level by Everspin [57]. They are already selling small STT-MRAM modules exceeding standard flash memory capabilities by far.

In the field of spintronics, many different approaches optimizing data storage in magnetic devices can be found. The spin caloritronics [58] utilize thermal gradients for heat assisted switching. Spin-valve like devices with only one

ferromagnetic electrode have been demonstrated using the *tunneling anisotropic magnetoresistance* (TAMR) [59, 60]. This is preferable, as stray fields are reduced, which supports further miniaturization. One step further leads to the data storage in AF materials itself, which produce no stray field at all. This is a remarkable step already indicated by Louis Néel. He was awarded with the Nobel prize in 1970 for his fundamental investigations of antiferromagnetism and stated in his prize lecture: "They [antiferromagnets] are extremely interesting from the theoretical viewpoint, but do not seem to have any applications" [61]. This corresponds to the staggered magnetization in the AF making a switching of the magnetization, either by external fields or electrical currents, difficult. Different approaches were able to switch the magnetization, however, only in one direction. In the recently emerging field of *antiferromagnetic spintronics* [62], Wadley *et al.* demonstrated a completely electrical switching between two magnetic states in the AF CuMnAs [63]. They exploited the inverse spin galvanic effect [64], which arises due to the lacking inversion symmetry of CuMnAs. Using this effect, it is possible to apply a staggered torque on the magnetic moments of the AF using an electric current which allows to switch the magnetization between different directions. Wadley and his coworkers prepared a star-shaped microstructure with read- and write-lanes for two magnetic states, and showed a reliable switching and AMR like readout of the AF state.

All in all, due to the supply risk for Iridium - which is part of the most commonly used AF - research towards novel AF materials is of increasing importance. Especially for the currently rising field of antiferromagnetic spintronics novel materials exhibiting interesting properties are fundamental. The search for these is an appealing task this work is dealing with.

2.3. Heusler Compounds

Heusler compounds are a family of ternary intermetallic compounds firstly presented as the prototype Cu_2MnAl by Friedrich Heusler in 1903 [65]. Their composition is X_2YZ; a sketch of a cubic unit cell is shown in Fig. 2.3. Interestingly, the investigated prototype Cu_2MnAl is ferromagnetic, even though none of its constituents are. This already gives a hint towards the diverse character of the Heusler family. Today, countless Heusler compounds are known [66]

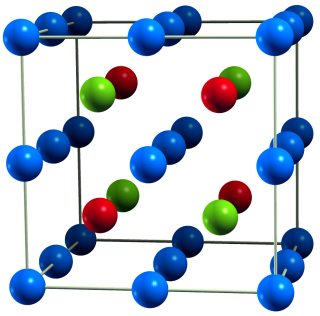

Figure 2.3. | A 16-atom cubic unit cell of the $L2_1$ Heusler structure. Blue positions are occupied by X=●, red positions by Y=● and green positions by Z=●

exhibiting a huge variety of properties. Besides the ferromagnetic Cu_2MnAl, Heusler compounds showing all kinds of magnetism (half-metallic ferromagnetism in Co_2MnSi [67], ferrimagnetism in Mn_2VAl [68], antiferromagnetism in Ru_2MnGe [20]), as well as many different other interesting properties have been found (semiconductivity in Fe_2TiSi [69], superconductivity in Ni_2ZrGa [70], heavy fermion systems like Cu_2CeIn [71], shape memory effects in Ni_2MnGa [72]). Even topological insulators recently have been predicted (V_2YBi [73]).

The Heusler compounds have attracted considerable attention due to this variety of properties [66]. In the field of spintronics the Co-based half metallic ferromagnetic Heusler compounds have been studied extensively [74]. Their high spin polarization resulted in giant effect sizes in magnetoresistive devices [53] as outlined in the previous section. A variation of their composition allows the magnetic properties to be tuned to tailor ideal materials [75]. Recently, even a non-vanishing TMR effect for a fully compensated ferrimagnet has been reported by Borisov *et al.* [76]. It seems more than feasible to investigate the Heusler family for novel AF materials useful for spintronic applications.

The Heusler crystal structure is $L2_1$ (spacegroup $Fm\bar{3}m$), an fcc-lattice with a four-atom basis. The atomic positions are $(0,0,0)$, $(\frac{1}{4},\frac{1}{4},\frac{1}{4})$, $(\frac{1}{2},\frac{1}{2},\frac{1}{2})$ and $(\frac{3}{4},\frac{3}{4},\frac{3}{4})$. The first and third one are occupied by the same atom X. Due to inversion symmetry, the other two positions are equivalent and therefore occupied by either Y or Z. The corresponding Wyckoff positions are $8c$ for the X atoms and $4a$ and $4b$ for Y and Z.

3 Theoretical Methods

Investigating ground state properties of quantum mechanical systems is a challenging task. Where the hydrogen atom as a two-body problem can be solved analytically, this is already impossible for helium. Numerically, small quantum systems can be solved, e.g., via matrix diagonalization. However, as the dimension of the underlying parameter space scales exponentially with the system size, computational limits are reached very quickly. Walter Kohn, one of the founders of the density functional theory (DFT), estimated in his Nobel prize lecture: The parameter space required for a system of 100 interacting particles would already severely exceed the number of baryons in the universe. He called this fact the "exponential wall" [77].

Therefore, complex many-body systems like solids and molecules require different approaches to be evaluated. In the case of solids, one of the most common techniques used is DFT. An introduction to this method is given in Sec. 3.1 followed by a brief overview of the two implementations used in this work in Sec. 3.2. In the last part of this chapter a pathway to calculate transition temperatures of magnetic materials based on the results obtained by DFT is discussed in Sec. 3.3. Unless otherwise stated, the formulation in the following chapter is done using atomic units ($\hbar = m_e = e^2 = 1$).

3.1. Density Functional Theory (DFT)

The general purpose of DFT is to determine the quantum mechanical ground state of a many-body system as a functional of the name-giving electron density without the challenging necessity of solving the full many-body Schrödinger equation. The following introduction will mainly follow the textbook of Koch and Holthausen [78], as well as a review article by Capelle [79]. Modern DFT in the form used in this work aroused in the 1960's, founded by Pierre Hohenberg and Walter Kohn [80]. They investigated an inhomogeneous electron gas in an arbitrary system of several atoms. The corresponding many-body Hamiltonian[1] $\widehat{\mathcal{H}}$ in general therefore consists of contributions from the nuclei (n), the electrons (e) and the interaction between them:

$$\widehat{\mathcal{H}} = \widehat{T}_\mathrm{e} + \widehat{T}_\mathrm{n} + \widehat{V}_\mathrm{ee} + \widehat{V}_\mathrm{nn} + \widehat{V}_\mathrm{en} + \widehat{V} \; . \tag{3.1}$$

Due to their large masses the nuclei move much slower than the electrons. We therefore use the Born-Oppenheimer approximation, where the nuclei are assumed to be fixed, so their kinetic energy $\widehat{T}_\mathrm{n}$ is zero. Furthermore, their potential energy due to Coulomb repulsion is merely a constant contribution in energy $\widehat{V}_\mathrm{nn} = E_\mathrm{nn}$. The remaining terms in the Hamiltonian are the kinetic energies of the electrons

$$\widehat{T}_\mathrm{e} = -\frac{1}{2}\sum_{j=1}^{N} \nabla_j^2 \; , \tag{3.2}$$

the repulsive Coulomb interaction between the electrons

$$\widehat{V}_\mathrm{ee} = \frac{1}{2}\sum_{i\neq j} \frac{1}{|\mathbf{r}_i - \mathbf{r}_j|} \; , \tag{3.3}$$

and the external potential

$$\widehat{V} = \sum_{j=1}^{N} v(\mathbf{r}_j) \; . \tag{3.4}$$

N is the number of electrons and $\mathbf{r}_i$ are their position vectors in all cases. Within the Born-Oppenheimer approximation the electrons are considered to move in

[1] Operators are denoted with a circumflex

the Coulomb potential of the fixed nuclei ($\widehat{V}_{\mathrm{en}}$). Thus, it is usually considered as part of the external potential, so the resulting electron Hamiltonian takes the form $\widehat{\mathcal{H}} = \widehat{T}_{\mathrm{e}} + \widehat{V}_{\mathrm{ee}} + \widehat{V}$. The total energy E is obtained as the expectation value of the Hamiltonian:

$$E = \left\langle \widehat{\mathcal{H}} \right\rangle = \left\langle \Psi | \widehat{\mathcal{H}} | \Psi \right\rangle \ , \tag{3.5}$$

where $\Psi = \Psi(\mathbf{r}_1, \mathbf{r}_2, \ldots, \mathbf{r}_N)$ is a solution of the N-electron Schrödinger equation. The Rayleigh-Ritz variational principle now states that for any probe Ψ' the resulting E is an upper bound for the true ground state energy E_0. Minimization of E with respect to Ψ' gives the true ground state energy

$$E_0 = \min_{\Psi'} \left\langle \Psi' | \widehat{\mathcal{H}} | \Psi' \right\rangle \ . \tag{3.6}$$

Although working in theory, this method is not feasible in practice, as obtaining the full many-body wave function Ψ requires solving the Schrödinger equation, facing the exponential wall mentioned above.

3.1.1. Hohenberg-Kohn Theorems

Using the probability interpretation of the quantum mechanical wave function Ψ, we can derive the electron density

$$n(\mathbf{r}) = N \int \mathrm{d}\mathbf{r}_2 \int \mathrm{d}\mathbf{r}_3 \ldots \int \mathrm{d}\mathbf{r}_N \left| \Psi(\mathbf{r}, \mathbf{r}_2, \ldots, \mathbf{r}_N) \right|^2 \ . \tag{3.7}$$

By integration over the whole space the total number of electrons is obtained by

$$\int n(\mathbf{r}) \mathrm{d}\mathbf{r} = N \ . \tag{3.8}$$

The electron density is the central quantity of DFT, for which Hohenberg and Kohn have proven two fundamental theorems in their original work. The first theorem proposes a unique correspondence between the external potential and the ground state electron density $n_0(\mathbf{r})$ (cited from Ref. [80]):

> *The external potential $v(\mathbf{r})$ is (to within a constant) a unique functional of $n_0(\mathbf{r})$, since, in turn, $v(\mathbf{r})$ fixes $\widehat{\mathcal{H}}$ we see that the full many particle ground state is a unique functional of $n_0(\mathbf{r})$.*

The message of this theorem ultimately leads to the finding that the Hamiltonian of a system is uniquely defined by the ground state electron density, and therefore all properties and observables. The proof is a straight forward consideration based on reductio ad absurdum, which can be found in any common DFT literature. As a consequence, we can write the ground state wave function, and in general every observable, as a functional of the electron density, e.g. $\Psi = \Psi[n_0]$. We write the total energy as

$$E[n] = T[n] + U[n] + V[n] + E_{\mathrm{nn}} = F_{\mathrm{HK}}[n] + \int n(\mathbf{r})v(\mathbf{r})\mathrm{d}\mathbf{r} + E_{\mathrm{nn}} \ , \qquad (3.9)$$

where the interaction between the electrons is given by $U[n]$. A *universal functional* $F_{\mathrm{HK}}[n] := T[n] + U[n]$ can be defined, which is valid for any number of particles and any external potential. The second Hohenberg-Kohn theorem applies the variational principle stating (adopted from Ref. [78]):

> *The functional that gives the ground state energy of the system attains its minimum if and only if the input density is the true ground state density.*

In other words, a minimization of the total energy functional $E[n]$ with respect to $n(\mathbf{r})$ leads to the true ground state density $n_0(\mathbf{r})$ and therefore all properties of the system. A proof is simply achieved by making use of the variational principle established for wave functions. To summarize, the ground state energy (and any other property of the system) can be expressed as a functional of the electron density $n(\mathbf{r})$, and the density which minimizes this functional is the true ground state density $n_0(\mathbf{r})$.

3.1.2. Kohn-Sham Ansatz

The density functional theory as formulated by Hohenberg and Kohn lacks two central points: First, the explicit form of the Hohenberg-Kohn functional $F_{\mathrm{HK}}[n]$ is unknown. Therefore, a simple variational approach to find the ground state density is not possible. Secondly, although there is a unique correspondence between the ground state density and properties of the system, in practice we do not know how to deduce or calculate these from the density. To face this major challenge in DFT, Kohn and Sham developed an approximative theory in

1965 reintroducing wave functions in the form of single-particle orbitals [81]. This theory results in an auxiliary, non-interacting system reproducing the same electron density as the interacting system.

As a first step, the kinetic energy is decomposed into two parts $T[n] = T_\mathrm{s}[n] + T_\mathrm{c}[n]$, where the first part is the known single particle kinetic energy, and the second part consists of contributions due to interaction and correlation, which are unknown in general. Additionally, the classical Coulomb self-interaction of the electron density $U_\mathrm{H}[n]$ can be separated from $U[n]$. The term

$$U_\mathrm{H}[n] = \frac{1}{2}\int \frac{n(\mathbf{r})n(\mathbf{r}')}{|\mathbf{r}-\mathbf{r}'|}\mathrm{d}\mathbf{r}\,\mathrm{d}\mathbf{r}' \tag{3.10}$$

is called the *Hartree energy*. In accordance to Eq. (3.9) the *Kohn-Sham total energy* can therefore be written as

$$E_\mathrm{KS}[n] = T_\mathrm{s}[n] + U_\mathrm{H}[n] + \int n(\mathbf{r})v(\mathbf{r})\mathrm{d}\mathbf{r} + E_\mathrm{nn} + E_\mathrm{xc}[n]\ , \tag{3.11}$$

where all unknown contributions due to interaction and correlation are merged in the so called *exchange-correlation functional*

$$E_\mathrm{xc}[n] = (T[n] - T_\mathrm{s}[n]) + (U[n] - U_\mathrm{H}[n])\ . \tag{3.12}$$

Simply spoken, $E_\mathrm{xc}[n]$ contains all errors introduced by the reduction to a non-interacting system except the classical Coulomb interaction between the electrons. The single-particle Schrödinger-like *Kohn-Sham equation* for the system is now

$$\left[-\frac{1}{2}\nabla^2 + V_\mathrm{KS}(\mathbf{r})\right]\phi_j(\mathbf{r}) = \epsilon_j\phi_j(\mathbf{r})\ , \tag{3.13}$$

where ϕ_j are one-electron functions (called *Kohn-Sham orbitals*) of a fictitious non-interacting system. ϵ_j are the corresponding Kohn-Sham eigenvalues. The electrons move in the effective *Kohn-Sham potential*

$$V_\mathrm{KS}(\mathbf{r}) = v(\mathbf{r}) + V_\mathrm{H}(\mathbf{r}) + V_\mathrm{xc}(\mathbf{r})\ , \tag{3.14}$$

which contains the contributions of the external potential $v(\mathbf{r})$, the Hartree potential

$$V_\mathrm{H}(\mathbf{r}) = \frac{\delta U[n]}{\delta n(\mathbf{r})} = \int \frac{n(\mathbf{r}')}{|\mathbf{r}-\mathbf{r}'|}\mathrm{d}\mathbf{r}'\ , \tag{3.15}$$

and the exchange-correlation contribution

$$V_{\mathrm{xc}}(\mathbf{r}) = \frac{\delta E_{\mathrm{xc}}[n]}{\delta n(\mathbf{r})} \ . \tag{3.16}$$

For the correct choice of $V_{\mathrm{xc}}(\mathbf{r})$ the auxiliary system will reproduce the correct ground state electron density of our original system, which is known exactly as

$$n(\mathbf{r}) = \sum_{j=1}^{N} |\phi_j(\mathbf{r})|^2 \ . \tag{3.17}$$

The Kohn-Sham potential Eq. (3.14) explicitly depends on the electron density obtained from a solution of Eq. (3.13), thus, an iterative solution of Eq. (3.13), Eq. (3.14) and Eq. (3.17) is required. The usual way is to prepare an initial, guessed starting electron density, then iteratively solve the equations to self-consistency. This scheme is shown in Fig. 3.1. It is noteworthy that the Kohn-Sham orbitals and the energy eigenvalues do not have a strict physical meaning. They are a mathematical construct used to obtain the ground state electron density of the original many-body system.

3.1.3. Approximations

Up to this point, the theory to obtain the ground state density is exact. In other words, the Kohn-Sham scheme yields the exact ground state density. But by applying it in practice, we have to face obstacles which cannot be avoided. Hence, it is necessary to introduce approximations. The first one is conceptual: As we simply are not able to calculate the real many-body wave function, we have to deal with the Kohn-Sham orbitals, which are the best approximation we could get so far. The second approximation is of numerical nature. In a calculation, the Kohn-Sham wave functions have to be translated on an explicit representation using a certain basis. An exact solution is then only obtained using a complete basis set. As the analytical form is unknown, this usually requires an infinite expansion of the wave functions to obtain exact results. As this is not possible, an appropriate choice of the basis and a suitable expansion cutoff is mandatory. Last but not least, the collective contributions from exchange and correlation merged into V_{xc} ($E_{\mathrm{xc}}[n]$ respectively) are still unknown.

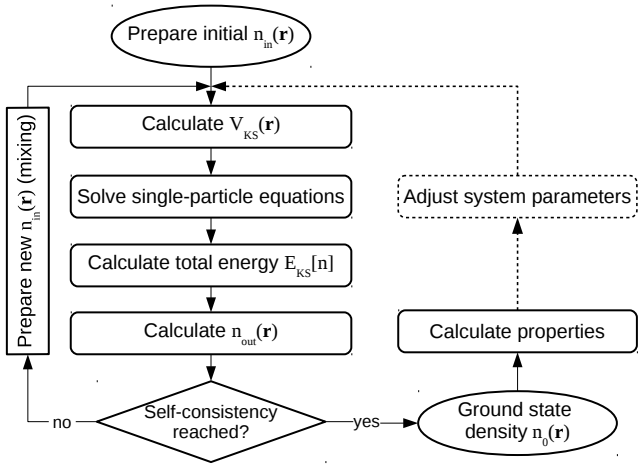

Figure 3.1. | Schematic showing the iterative steps of solving the Kohn-Sham equations in a self-consistency cycle used in a DFT calculation. Ground state system parameters, such as a lattice constant, can be found by repeating cycles for slight adjustments (optional dashed part).

Local density approximation

The major remaining task is to find a suitable approximation for the exchange-correlation (xc) functional $E_{\mathrm{xc}}[n]$. Historically, the most important approximation is based on the homogeneous electron gas (HEG), where electrons are considered to move on a positive background charge distribution created by the nuclei. The xc functional can now be written in the simple form

$$E_{\mathrm{xc}}^{\mathrm{LDA}}[n] = \int n(\mathbf{r}) e_{\mathrm{xc}}^{\mathrm{HEG}}(n(\mathbf{r}))\mathrm{d}\mathbf{r} \; . \tag{3.18}$$

Here, $e_{\mathrm{xc}}^{\mathrm{HEG}}$ is the energy density of the HEG. In this case E_{xc} only depends on the local value of the density, so the approximation is called *local density approximation* (LDA). As the exchange contribution is known analytically, the energy density can be split into exchange and correlation parts:

$$e_{\mathrm{xc}}^{\mathrm{HEG}}(n(\mathbf{r})) = e_{\mathrm{x}}^{\mathrm{HEG}}(n(\mathbf{r})) + e_{\mathrm{c}}^{\mathrm{HEG}}(n(\mathbf{r})) \; . \tag{3.19}$$

The explicit expression for the correlation part is unknown, hence its determination remains subject to an approximation. First, approximations based on perturbation theory have been developed [82, 83]. Modern expressions are parameterized using data of quantum Monte Carlo simulations of the HEG [84]. As the HEG resembles a perfect metal, the LDA is well suited, e.g., for metallic solids. Moreover, it also works surprisingly well for other systems like molecules, as it incorporates a systematic error cancellation [79]. Nevertheless, LDA tends to overestimate binding energies resulting in too short bond lengths. Examples for LDA xc functionals are implementations of Vosko, Wilk, and Nusair (VWN) [85] or Perdew and Wang (PW) [86].

Generalized gradient approximation

In real systems the electron density is in general inhomogeneous, so non-vanishing density gradients occur. The LDA can be considered as a zeroth-order approximation of a general expansion in terms of the density and its derivatives. Hence, an extension to LDA are functionals which not only depend on the local value, but also on density gradients. So called *gradient expansion approximations* tried to include higher-order corrections in terms of $|\nabla n(\mathbf{r})|$, $|\nabla^2 n(\mathbf{r})|$ etc., but almost always failed to improve the results. A breakthrough was made by introducing a more general functional of $n(\mathbf{r})$ and $\nabla n(\mathbf{r})$, the *generalized gradient approximation* (GGA), instead of a power series like expansion. Such a GGA functional takes the form

$$E_{\mathrm{xc}}^{\mathrm{GGA}}[n] = \int f(n(\mathbf{r}), \nabla n(\mathbf{r}))\mathrm{d}\mathbf{r} \,, \tag{3.20}$$

where there are generally no restrictions for the functional f. The GGA functionals are especially useful for systems with a significant inhomogeneous electron density. Regarding applicability, they can behave quite differently due to their choice of f. One of the most used GGA functionals in solid state physics is the implementation of Perdew, Burke and Ernzerhof (PBE) [87]. The PBE functional corrects the overestimation of binding energies in the LDA, but systematically overestimates the bond lengths slightly.

Many functionals such as the PBE functional are non-empirical, i.e., not based on any experimentally measured values. This is the essence of *ab initio* calculations, as they are only based on fundamental physics without the use of any

empirical values. However, empirical functionals supported by experimental data also exist, which aim to reproduce this data well.

3.1.4. Magnetism in DFT

Up to now the formulation of DFT is charge-only, i.e., the spin of the electrons is neglected. Hence, in order to deal with magnetic, i.e. spin-polarized systems, an extension to a more general theory (spin DFT) is required. This is achieved by introducing additional densities besides the charge density $n(\mathbf{r})$. In the simplest case of collinear magnetism, where the electron spin has only one degree of freedom along a certain direction, a single additional density is required. There are several possible choices of the fundamental density, however, all leading to an equivalent formulation. A common way is dealing with a charge density for each spin orientation, up ($n^{\uparrow}(\mathbf{r})$) and down ($n^{\downarrow}(\mathbf{r})$). The total charge density $n(\mathbf{r})$ and the spin density $s(\mathbf{r})$ then are

$$n(\mathbf{r}) := n^{\uparrow}(\mathbf{r}) + n^{\downarrow}(\mathbf{r}) \tag{3.21}$$

$$s(\mathbf{r}) := n^{\uparrow}(\mathbf{r}) - n^{\downarrow}(\mathbf{r}) \ . \tag{3.22}$$

This separation is possible due to the non-relativistic formulation neglecting spin-orbit-coupling effects. Thus, spin and spatial degrees of freedom decouple and the resulting wave functions can be separated into a tuple for spin-up and spin-down. The Kohn-Sham equations then apply separately for both spin-up and -down with a spin dependent Kohn-Sham potential V_{KS}^{σ}, indexed by σ:

$$\left[-\frac{1}{2}\nabla^2 + V_{\mathrm{KS}}^{\sigma}(\mathbf{r})\right]\phi_j^{\sigma}(\mathbf{r}) = \epsilon_j^{\sigma}\phi_j^{\sigma}(\mathbf{r}) \tag{3.23}$$

$$V_{\mathrm{KS}}^{\sigma}(\mathbf{r}) = v^{\sigma}(\mathbf{r}) + \frac{\delta U[n^{\uparrow}, n^{\downarrow}]}{\delta n^{\sigma}} + \frac{\delta E_{\mathrm{xc}}[n^{\uparrow}, n^{\downarrow}]}{\delta n^{\sigma}} \tag{3.24}$$

$$n(\mathbf{r}) = \sum_{\sigma}\sum_{j=1}^{N_{\sigma}} \left|\phi_j^{\sigma}(\mathbf{r})\right|^2 \ . \tag{3.25}$$

Here, N_{σ} is the number of spin-up or -down electrons and $N = N_{\uparrow} + N_{\downarrow}$. Especially, $v^{\sigma}(\mathbf{r}) = v(\mathbf{r}) - \sigma\mu_0 B(\mathbf{r})$ (where $\sigma = \pm 1$) contains the additional Zeeman term. The xc functionals change accordingly, where the LDA used in spin DFT is

called local spin density approximation (LSDA). LSDA and GGA functionals then take the form

$$E_{\mathrm{xc}}^{\mathrm{LSDA}}[n^{\uparrow}, n^{\downarrow}] = \int n(\mathbf{r}) e_{\mathrm{xc}}^{\mathrm{HEG}}(n^{\uparrow}(\mathbf{r}), n^{\downarrow}(\mathbf{r}))\mathrm{d}\mathbf{r} \tag{3.26}$$

$$E_{\mathrm{xc}}^{\mathrm{GGA}}[n^{\uparrow}, n^{\downarrow}] = \int f(n^{\uparrow}(\mathbf{r}), n^{\downarrow}(\mathbf{r}), \nabla n^{\uparrow}(\mathbf{r}), \nabla n^{\downarrow}(\mathbf{r}))\mathrm{d}\mathbf{r} \ . \tag{3.27}$$

A further extension to non-collinear magnetism is possible by introducing a full three dimensional spin density $\mathbf{s}(\mathbf{r})$ instead of a scalar one. Therefore, one has to deal with four sets of functions. As this is computationally demanding, usually collinear spin DFT is used.

3.1.5. DFT of Solids: Periodic Boundary Conditions

In solid state physics we deal with crystals, i.e. ideal - at least in theory - periodic systems. Here, the nuclei are perfectly ordered on a periodic lattice, thus the potential the electrons are moving in is periodic as well. Consequently, the whole problem becomes periodic and allows us to apply periodic boundary conditions. Hence, we are able to deduce bulk properties from a primitive unit cell of the crystal containing only a few atoms. For a periodic potential $V(\mathbf{r}) = V(\mathbf{r} + \mathbf{R})$, where $\mathbf{R} = n_1\mathbf{a}_1 + n_2\mathbf{a}_2 + n_3\mathbf{a}_3$ ($n_j = 0, 1, 2, \ldots$) is an arbitrary translation along the lattice vectors $\mathbf{a}_j$, the *Bloch theorem* states that solutions of the Schrödinger equation take the general form

$$\psi_{\mathbf{k}}(\mathbf{r}) = \mathrm{e}^{i\mathbf{k}\cdot\mathbf{r}} u_{\mathbf{k}}(\mathbf{r}) \ , \tag{3.28}$$

where $u_{\mathbf{k}}(\mathbf{r}+\mathbf{R}) = u_{\mathbf{k}}(\mathbf{r})$ has the same periodicity as the crystal lattice (and thus $V(\mathbf{r})$). Therefore, except for a phase factor, the wave functions are periodic as well:

$$\psi_{\mathbf{k}}(\mathbf{r} + \mathbf{R}) = \mathrm{e}^{i\mathbf{k}\cdot\mathbf{R}} \psi_{\mathbf{k}}(\mathbf{r}) \ . \tag{3.29}$$

From this it follows that the probability distribution and thus the electron density is also periodic. The Kohn-Sham equations can be separately solved for each $\mathbf{k}$ of the first Brillouin zone in the reciprocal space, leading to a band structure of energy eigenvalues. In principle we would need to integrate over the whole Brillouin zone. However, in practice, this integration can be approximated by a

weighted summation, as the wave functions vary slowly with $\mathbf{k}$. The electron density is therefore calculated by

$$n(\mathbf{r}) = \frac{1}{N_k} \sum_{\mathbf{k}} n_{\mathbf{k}}(\mathbf{r}) \ , \tag{3.30}$$

where $n_{\mathbf{k}}(\mathbf{r})$ is the electron density for a given $\mathbf{k}$ and N_k the number of $\mathbf{k}$-points. The numerical results crucially depend on an adequate choice of N_k. Fortunately, it is possible to exploit symmetries of the crystal lattice. The summation over the Brillouin zone can be reduced to an irreducible wedge, and the result extended to the whole Brillouin zone via symmetry operations. Nevertheless, convergence regarding the chosen $\mathbf{k}$-point mesh has to be ensured for each system separately to obtain consistent results.

3.2. DFT Implementations

In the following sections we will briefly discuss the DFT implementations and codes used in this work. Fundamental investigations are done using the *Vienna Ab Initio Simulation Package* (VASP) [88–90]. In order to determine transition temperatures for magnetic materials exchange parameters are calculated using the *Munich spin-polarized relativistic Korringa-Kohn-Rostoker* (SPR-KKR) package [91, 92].

A very convenient choice to write down the periodic part of the wave function is an expansion in terms of plane waves, where the expansion is cut off at a certain wave vector[2]. Plane waves are solutions of the free electron Schrödinger equation, so this is a reasonable choice while dealing with metal-type materials, where the free electron assumption approximately applies. Furthermore, the implementation of the Hamiltonian as well as the calculation of energies is trivial. However, due to the deep Coulomb potential in close vicinity to the nuclei, the orthogonal wave functions are rapidly varying. An adequate expansion would require an enormous set of plane waves.

There are different approaches facing this problem. The *augmented plane waves* (APW) method divides the space into nuclei centered non-overlapping aug-

[2] In practice, often a cutoff *energy* $E_{\max}$ is given, related to the cutoff vector $\mathbf{G}_{\max}$ by $E_{\max} = |\mathbf{G}_{\max}|^2 \hbar^2 / 2m_e$.

mentation spheres and an interstitial region. Within the augmentation spheres, the wave functions are augmented by various approaches such as atomic orbitals. For this method, a matching of the APWs with the plane wave expansion in the interstitial region at the sphere boundary is necessary.

Another approach uses *pseudopotentials*. Electrons are usually divided into core and valence electrons. The first ones are localized close to the nucleus, e.g. $1s$, $2s$, $2p$ states and so on, and their states are assumed not to change in different environments. Further away from the nuclei only the valence electron states are non-zero resulting in much smoother wave functions. Pseudopotentials for isolated atoms then are created by pre-calculating an effective potential of the nuclei in conjunction with the core electrons. The resulting potential leads to smoother wave functions significantly reducing the necessary size of the plane wave basis set. The Kohn-Sham equations are then only solved for the valence electrons. An all-electron wave function is lost, and corresponding information about core-related quantities, e.g., hyperfine fields, cannot be obtained.

3.2.1. Vienna Ab Initio Simulation Package (VASP)

Besides the pseudopotential method, VASP supports the *projector augmented wave* (PAW) method invented by Peter Blöchl in 1994 [93]. It provides special advantages compared to APW or pseudopotential methods, hence it is used for most of the calculation presented in this work. A brief introduction to the method follows based on two introductory papers by Blöchl [94] and Rostgaard [95].

In principle, the PAW method is a merging of the ideas behind APW and pseudopotentials. In fact, APW methods can be obtained as a special case and the pseudopotential method by a well-defined approximation of the PAW method [93]. The idea is to define a transformation $\widehat{\mathcal{T}}$ by

$$|\Psi\rangle = \widehat{\mathcal{T}}\,|\widetilde{\Psi}\rangle \ , \tag{3.31}$$

which transforms an auxiliary smooth wave function $|\widetilde{\Psi}\rangle$ back to the all-electron wave function $|\Psi\rangle$, solution of the single-particle Kohn-Sham equation Eq. (3.13). In the following, original, untransformed functions are referred to as all-electron (AE) functions, whereas transformed functions, marked with a tilde, are referred to as pseudo (PS) functions. For the sake of clarity, we drop any index and deal

with a single wave function only. As the wave functions are naturally smooth in the valence region, a transformation is only required within a certain distance to the nucleus. A radius r_c^a defines an *augmentation region* Ω_a, similar to APW methods, around the atom a at position $\mathbf{R}^a$, where $|\mathbf{r} - \mathbf{R}^a| \leq r_c^a$. Requiring $\widehat{\mathcal{T}}$ to affect the wave function only within these non-overlapping augmentation regions, we can write it in a site-wise form

$$\widehat{\mathcal{T}} = 1 + \sum_a \widehat{\mathcal{T}}_a \ . \tag{3.32}$$

The sum runs over all atoms a with the atom-centered transformations $\widehat{\mathcal{T}}_a$. Within the Ω_a regions we expand the PS wave function $|\widetilde{\Psi}\rangle$ into partial waves $|\widetilde{\Phi}_j^a\rangle$

$$|\widetilde{\Psi}\rangle = \sum_j |\widetilde{\Phi}_j^a\rangle \, c_j^a \quad \text{within } \Omega_a \ , \tag{3.33}$$

where c_j^a are the expansion coefficients for atom a and the index j refers to quantum numbers of the partial waves. Each of the PS partial waves corresponds an AE partial wave $|\Phi_j^a\rangle$, which is the result of the transformation:

$$|\Phi_j^a\rangle = \widehat{\mathcal{T}} \, |\widetilde{\Phi}_j^a\rangle = \left(1 + \widehat{\mathcal{T}}_a\right) |\widetilde{\Phi}_j^a\rangle \quad \text{within } \Omega_a \ . \tag{3.34}$$

Therefore, as in the region Ω_a only $\widehat{\mathcal{T}}_a$ has an effect, this defines the atom-centered transformations $\widehat{\mathcal{T}}_a$ by

$$\widehat{\mathcal{T}}_a \, |\widetilde{\Phi}_j^a\rangle = |\Phi_j^a\rangle - |\widetilde{\Phi}_j^a\rangle \ , \tag{3.35}$$

so the transformation adds the difference between the PS partial waves and the AE partial waves. As by definition the transformation $\widehat{\mathcal{T}}_a$ has no effect outside the augmentation region, the PS and AE partial waves are equal beyond the distance r_c^a to the nucleus:

$$|\Phi_j^a\rangle = |\widetilde{\Phi}_j^a\rangle \quad \text{for } |\mathbf{r} - \mathbf{R}^a| > r_c^a \ . \tag{3.36}$$

We write the AE wave function by applying the transformation

$$|\Psi\rangle = \widehat{\mathcal{T}} \, |\widetilde{\Psi}\rangle = \sum_j |\Phi_j^a\rangle \, c_j^a \quad \text{within } \Omega_a \tag{3.37}$$

and see that the expansion has the same expansion coefficients as the PS wave function. As the transformation $\widehat{\mathcal{T}}$ is linear, the coefficients must be linear functionals of the PS wave function $|\widetilde{\Psi}\rangle$. Therefore, the coefficients are obtained by a scalar product

$$c_j^a = \langle \widetilde{p}_j^a | \widetilde{\Psi} \rangle \tag{3.38}$$

with the name-giving smooth *projector functions* $|\widetilde{p}_j^a\rangle$. Without overlap of the augmentation regions, by inserting Eq. (3.38) into Eq. (3.33), we can deduce the completeness relation

$$\sum_j |\widetilde{\Phi}_j^a\rangle \langle \widetilde{p}_j^a| = 1 \,. \tag{3.39}$$

This also implies the orthogonality $\langle \widetilde{p}_i^a | \widetilde{\Phi}_j^a \rangle = \delta_{ij}$, where δ_{ij} is the Kronecker-Delta[3]. Multiplying the atom-centered transformation $\widehat{\mathcal{T}}_a$ with the identity Eq. (3.39) and inserting the result of Eq. (3.35) we obtain the representation

$$\widehat{\mathcal{T}}_a = \sum_j \widehat{\mathcal{T}}_a |\widetilde{\Phi}_j^a\rangle \langle \widetilde{p}_j^a| = \sum_j \left(|\Phi_j^a\rangle - |\widetilde{\Phi}_j^a\rangle \right) \langle \widetilde{p}_j^a| \,. \tag{3.40}$$

Using this, the full transformation takes the form

$$\widehat{\mathcal{T}} = 1 + \sum_a \sum_j \left(|\Phi_j^a\rangle - |\widetilde{\Phi}_j^a\rangle \right) \langle \widetilde{p}_j^a| \,. \tag{3.41}$$

Furthermore, with knowledge of the AE and PS partial waves, and the projector functions, we are able to obtain the exact AE wave function from the PS wave function by

$$|\Psi\rangle = |\widetilde{\Psi}\rangle - \sum_a \underbrace{\sum_j |\widetilde{\Phi}_j^a\rangle \langle \widetilde{p}_j^a | \widetilde{\Psi}\rangle}_{|\widetilde{\Psi}^a\rangle} + \sum_a \underbrace{\sum_j |\Phi_j^a\rangle \langle \widetilde{p}_j^a | \widetilde{\Psi}\rangle}_{|\Psi^a\rangle} \,. \tag{3.42}$$

This equation shows the nature of the transformation: In the first term, the smooth, pseudo part in the augmentation region is removed, and in the second term replaced by the all-electron part. An example is visualized in Fig. 3.2. By construction $|\widetilde{\Psi}\rangle$ is smooth everywhere, hence much more easy to handle numer-

[3] $\delta_{ij} = 1$ if $i = j$, $\delta_{ij} = 0$ if $i \neq j$

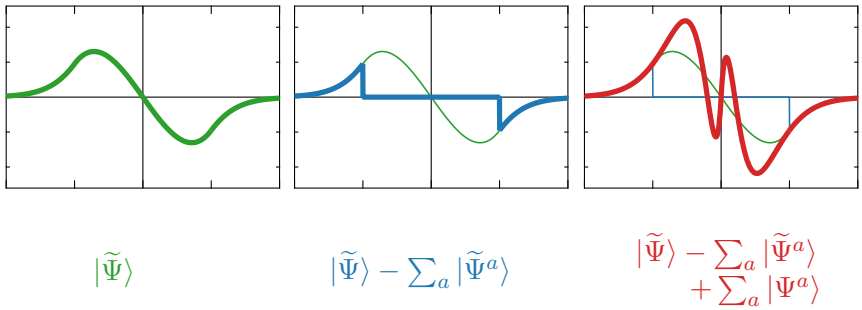

Figure 3.2. | Example of a PAW transformation (Eq. (3.42)) for the radial part of a hydrogen wave function. The green pseudo wave function is smooth even in the core region. For the blue function the smooth pseudo partial wave expansion in the central augmentation region has been removed. In red, the all-electron wave function is shown.

ically than the original Kohn-Sham AE wave function. Inserting the transformation into the Kohn-Sham equation we get the transformed Kohn-Sham equation

$$\widehat{\widetilde{\mathcal{H}}}\,|\widetilde{\Psi}_n\rangle = \epsilon_n \widehat{\widetilde{S}}\,|\widetilde{\Psi}_n\rangle \tag{3.43}$$

with the transformed Hamiltonian $\widehat{\widetilde{\mathcal{H}}} = \widehat{\mathcal{T}}^\dagger \widehat{\mathcal{H}} \widehat{\mathcal{T}}$ and the so called overlap operator $\widehat{\widetilde{S}} = \widehat{\mathcal{T}}^\dagger \widehat{\mathcal{T}}$. The variational quantity for this equation is now the smooth pseudo wave function $|\widetilde{\Psi}_n\rangle$. Finding the self-consistent solution for this transformed problem is much more feasible. No information is lost as the complete all-electron wave function of the original Kohn-Sham problem can be reconstructed. However, PAW data sets (partial wave expansions, projector functions, etc.) for each element need to be constructed in advance. This is done by highly accurate atomic DFT calculations on isolated atoms. Details about a reasonable choice for partial wave functions as well as construction of the projector functions can be found in Ref.s [94, 95]. The VASP code provides PAW data sets for all elements, which are ready to use; their construction is not part of this work.

The electronic structure of the isolated atoms is often used as a starting configuration in PAW calculations. Usually the frozen-core approximation is used, where the core states are considered well localized within the augmentation regions, and are not affected by changes of the atomic environment. In the DFT

calculation, only the valence electrons will be calculated. This is equivalent to the pseudopotential approach, however, due to the PAW transformation all core-related information can be restored.

3.2.2. Munich SPR-KKR Package

A different approach to find the electronic ground state is proposed by Korringa [96], Kohn and Rostoker [97] (KKR) by means of *multiple scattering theory* (MST). The problem is formulated as electrons scattered by the nuclear potential. The total potential is separated into scattering centers located at each nuclei. First, the scattering properties of these centers are calculated individually. Second, the solution of the Schrödinger equation is determined by the requirement that an incident wave at one center is the sum of the outgoing waves from all other centers. Due to the formulation in multiple scattering the KKR method is not restricted to periodic systems like solids, and can be easily applied to finite systems like molecules.

In this section the fundamental considerations implemented in the Munich SPR-KKR package [92] as of the publication by Ebert *et al.* [91], the authors of the code, are outlined. A very detailed introduction as well as explicit forms of quantities and functions dealt with can be found in this reference as well as in the one by Mavropoulos and Papanikolaou [98]. The KKR theory is an approach of determining the electronic structure equivalent to the usual DFT way. Instead of using the electron density, the *Green's function* $G(\mathbf{r}, \mathbf{r}', E)$ is introduced, which is defined by

$$\left(E - \widehat{\mathcal{H}}\right) G(\mathbf{r}, \mathbf{r}', E) = \delta(\mathbf{r} - \mathbf{r}') \; . \tag{3.44}$$

The Hamilton operator $\widehat{\mathcal{H}} = \widehat{\mathcal{H}}^0 + \widehat{V}$ is decomposed into a "free" part $\widehat{\mathcal{H}}^0$, for which solutions $\Psi^0(\mathbf{r}, E)$ are known, and a perturbation part $\widehat{V}$. This allows us to write the Schrödinger equation in an integral form, the *Lippmann-Schwinger equation*

$$\Psi(\mathbf{r}, E) = \Psi^0(\mathbf{r}, E) + \int G^0(\mathbf{r}, \mathbf{r}', E) V(\mathbf{r}) \Psi(\mathbf{r}, E) \mathrm{d}\mathbf{r}' \; , \tag{3.45}$$

where $G^0(\mathbf{r}, \mathbf{r}', E)$ is the Green's function of the unperturbed system. The Green's function in its spectral representation is

$$G^+(\mathbf{r}, \mathbf{r}', E) = \lim_{\varepsilon \to +0} \sum_j \frac{\psi_j(\mathbf{r}) \psi_j^*(\mathbf{r}')}{E - E_j + \mathrm{i}\varepsilon} \; , \tag{3.46}$$

with the eigenfunctions $\psi_j(\mathbf{r})$ and the eigenvalues E_j. Poles of the Green's function indicate the eigenvalues, so the limit avoids divergencies. Using the Dirac identity $\lim_{\varepsilon\to 0} \Im\,(x+\mathrm{i}\varepsilon)^{-1} = -\pi\delta(x)$ we can relate the Green's function to the density of states $\rho(E)$, the charge density $n(\mathbf{r})$ and the expectation value of an operator $\widehat{\mathcal{A}}$ by:

$$\rho(E) = -\frac{1}{\pi}\Im \int G^+(\mathbf{r},\mathbf{r}',E)\mathrm{d}\mathbf{r} \tag{3.47}$$

$$n(\mathbf{r}) = -\frac{1}{\pi}\Im \int^{E_\mathrm{F}} G^+(\mathbf{r},\mathbf{r}',E)\mathrm{d}E \tag{3.48}$$

$$\left\langle \widehat{\mathcal{A}} \right\rangle = -\frac{1}{\pi}\Im \int\int^{E_\mathrm{F}} \widehat{\mathcal{A}} G^+(\mathbf{r},\mathbf{r}',E)\mathrm{d}E\mathrm{d}\mathbf{r}\,, \tag{3.49}$$

where E_F is the Fermi energy. With the expressions above we are able to calculate all ground state properties of the system without the explicit use of the eigenfunctions. Thus, the Green's function contains all information about the system just as the ground state electron density.

The calculation of the Green's function as follows is split into a (single-site) potential and a geometrical part. For this purpose, in the full potential mode the system is split into Wigner-Seitz polyhedra centered at each nucleus, and the potential is split accordingly into non-overlapping single-site parts $V = \sum_n V^n$ within these polyhedra. The full potential in the polyhedra is expressed in an angular momentum expansion using spherical harmonics.

Now the solutions of the single-site problems are calculated, where the scattering solutions $\psi^n(\mathbf{r},E)$ could be obtained from the Lippmann-Schwinger equation Eq. (3.45). However, a major, appealing benefit of the Green's function formalism is the use of the *Dyson equation*, which provides an alternative approach. It allows us to write the Green's function G for a system $\widehat{\mathcal{H}} = \widehat{\mathcal{H}}^\mathrm{ref} + \widehat{\mathcal{H}}^\mathrm{pert}$ in terms of a Green's function G^ref for a simpler reference system $\widehat{\mathcal{H}}^\mathrm{ref}$ with a perturbation $\widehat{\mathcal{H}}^\mathrm{pert}$. The Dyson equation here in operator form is

$$\widehat{G} = \widehat{G}^\mathrm{ref} + \widehat{G}^\mathrm{ref}\widehat{H}^\mathrm{pert}\widehat{G}\,. \tag{3.50}$$

Interpreting the single-site problem as a free electron scattered at the potential V^n, we can write the Dyson equation for the single-site scattering problem as

$$\widehat{G}^n(E) = \widehat{G}^0(E) + \widehat{G}^0(E)\widehat{V}^n(E)\widehat{G}^n(E) \tag{3.51}$$

with the perturbation V^n, where n is the site index. The free electron Green's function of the reference system corresponding to $\widehat{G}^0(E)$ is

$$G^0(\mathbf{r}, \mathbf{r}', E) = -\frac{\mathrm{e}^{-\mathrm{i}\sqrt{E}|\mathbf{r}-\mathbf{r}'|}}{4\pi\,|\mathbf{r}-\mathbf{r}'|}\ . \tag{3.52}$$

We remember the Lippmann-Schwinger equation in order to solve the Dyson equation (3.45). In Dirac notation, it reads $|\Psi\rangle = |\Psi^0\rangle + \widehat{G}^0\widehat{V}\,|\Psi\rangle$. We define a *transition matrix* $\widehat{T}$ by

$$\widehat{V}\,|\Psi\rangle = \widehat{T}\,|\Psi^0\rangle\ . \tag{3.53}$$

This transition matrix relates the eigenfunctions of the perturbed Hamiltonian to the eigenfunctions of the unperturbed system. It has the general form

$$\widehat{T} = \widehat{V} + \widehat{V}\widehat{G}^0\widehat{T} \tag{3.54}$$

$$= \widehat{V}(1 - \widehat{G}^0\widehat{V})^{-1} \tag{3.55}$$

and can be expanded into a Born series by iterative insertion. The Dyson equation using a single-site *t-matrix* $\hat{t}^n$, which transforms the incoming wave of an electron into a scattered wave, is

$$\widehat{G} = \widehat{G}^0(E) + \widehat{G}^0(E)\hat{t}^n(E)\widehat{G}^0(E)\ . \tag{3.56}$$

When dealing with multiple scatterers we find an analogous equation for the complete problem:

$$\widehat{G}(E) = \widehat{G}^0(E) + \widehat{G}^0(E)\widehat{V}(E)\widehat{G}(E) \tag{3.57}$$

$$= \widehat{G}^0(E) + \widehat{G}^0(E)\widehat{T}(E)\widehat{G}^0(E)\ . \tag{3.58}$$

All scattering processes can be decomposed into a series of single-site scattering events characterized by $\hat{t}^n$ and free propagation in between. Hence, the multiple *scattering $\widehat{T}$-matrix operator* is

$$\widehat{T}(E) = \sum_{nn'} \widehat{\tau}^{nn'}(E) \tag{3.59}$$

using the *scattering path operator* $\widehat{\tau}^{nn'}(E)$, which translates a wave incoming at site n' to an outgoing wave at site n. The operator takes all possible scattering

events in between into consideration. The equation of motion for this operator in an angular momentum basis is

$$\underline{\tau}^{nn'}(E) = \underline{t}^{n}(E)\delta_{nn'} + \underline{t}^{n}(E)\sum_{m\neq n} G^{0nm}(E)\underline{\tau}^{mn'}(E)\ , \tag{3.60}$$

where we note the adoption in an angular momentum basis by the underlines. Solving this problem for a finite system is done via matrix inversion by

$$\underline{\underline{\tau}}(E) = \left[\underline{t}(E)^{-1} - \underline{\underline{G}}^{0}(E)\right]^{-1}\ , \tag{3.61}$$

where double underlines include site and angular momentum indices, so in this case $[\underline{\tau}]_{nn'} = \underline{\tau}^{nn'}$, $[\underline{\underline{G}}^{0}]_{nn'} = \underline{G}^{0nn'}$ and $[\underline{t}]_{nn'} = \underline{t}^{n}\delta_{nn'}$. Commonly, the matrix $\left[\underline{t}^{-1} - \underline{\underline{G}}^{0}\right] = \underline{\underline{M}}$ is called *real-space KKR matrix*. The dimension of these matrices is determined by the number of scatterers N and the angular momentum expansion, which is usually cut off at a certain maximum $l_{\max}$. The resulting dimension is $D = N(l_{\max}+1)^2$. Hence, $l_{\max}$ crucially affects the numerical effort. Usually, a value of $l_{\max} = 3$ or 4 is sufficient. This finite cutoff introduces systematic errors in the charge density resulting in a miscalculation of the Fermi energy. Lloyd proposed an analytical expression (Lloyd's formula) [99] to solve this problem by an accurate charge density normalization.

For a periodic system like solids, the solution is found by a Fourier transformation of Eq. (3.60) into

$$\underline{\tau}^{nn'}(E) = \frac{1}{\Omega_{\mathrm{BZ}}}\int_{\Omega_{\mathrm{BZ}}} \left[\underline{t}(E)^{-1} - \underline{G}^{0}(\mathbf{k},E)\right]^{-1} \mathrm{e}^{\mathrm{i}\mathbf{k}\cdot(\mathbf{R}_n - \mathbf{R}_{n'})}\mathrm{d}\mathbf{k}\ , \tag{3.62}$$

where Ω_{BZ} is the Brillouin zone volume, $\mathbf{R}_n$ the positions of the nuclei and $\underline{G}^{0}(\mathbf{k},E)$ the so-called reciprocal space structure constant matrix.

Similar to other DFT codes, the core electrons, which are well localized within the constructed Wigner-Seitz polyhedra, are not considered within the multiple scattering calculation. They are treated separately in a relativistic way by the Dirac equation. The problem then is solved only for the valence electrons, where the SPR-KKR package supports either a scalar-relativistic way neglecting spin-orbit coupling or a full relativistic calculation.

3.3. Calculation of Transition Temperatures

One of the most important properties of magnetic materials is their transition temperature, above which no spontaneous ordering is found anymore. For ferromagnets, this temperature is the *Curie temperature* T_C, whereas for antiferromagnets it is the *Néel temperature* T_N. As these kinds of magnetism are of collective origin, a straight forward calculation from a primitive unit cell is not directly possible. Total energy differences between F and AF configurations can provide information of the interaction strength, but the estimation is typically not very accurate. The SPR-KKR package ships with an implementation of the theory by Liechtenstein *et al.* [100] to directly calculate the interaction between spins, the exchange coupling parameters. As this is the origin of collective magnetic ordering, we can deduce transition temperatures from the exchange parameters.

3.3.1. Exchange Coupling Parameters

The interaction between spins (or the corresponding magnetic moments, respectively) is described by an exchange integral [101]

$$J = \int \psi_a^*(\mathbf{r}_1)\psi_b^*(\mathbf{r}_2)\widehat{\mathcal{H}}\psi_a(\mathbf{r}_2)\psi_b(\mathbf{r}_1)\mathrm{d}\mathbf{r}_1\mathrm{d}\mathbf{r}_2 \ , \tag{3.63}$$

which can be derived from quantum mechanical indistinguishability of two particles a and b, leading back to the Pauli principle. An effective Hamiltonian describing the exchange interaction is the *Heisenberg Hamiltonian*

$$\widehat{\mathcal{H}}_\mathrm{Heis} = -\sum_{i,j} \widehat{\mathbf{S}}_i \, \mathbf{J} \, \widehat{\mathbf{S}}_j \ , \tag{3.64}$$

where $\widehat{\mathbf{S}}_i$ is the spin operator for site i. $\mathbf{J}$ contains the interaction and can be in general a complex matrix. In a first order approximation, the spins i and j interact directly only via a single exchange coupling parameter J_{ij}. In a classical Heisenberg model [102], which has proven to work well [103], the spins are able to orient arbitrarily in space. The Hamiltonian consists of the unit vectors $\mathbf{e}_i$ pointing in the direction of the magnetic moment at site i:

$$\widehat{\mathcal{H}} = -\sum_{i,j} J_{ij}\mathbf{e}_i \cdot \mathbf{e}_j \ . \tag{3.65}$$

To calculate these exchange parameters from an ab-initio calculation, the energy difference δE induced by a small deviation from the magnetic configuration in the ground state is calculated. This is done by rotating a pair of spins i and j by an angle $\pm\theta/2$ in real space. This requires localized magnetic moments which do not change in magnitude dependent on the spin configuration. The resulting energy difference is $\delta E_{ij} = J_{ij}(1 - \cos\theta)$. Using the local force theorem of Andersen [104] this energy difference can be expressed as

$$\delta E = \int^{E_\mathrm{F}} E\delta\rho(E)\mathrm{d}E = -\int^{E_\mathrm{F}} \delta N(E)\mathrm{d}E \,, \tag{3.66}$$

where $\rho(E) = \mathrm{d}N/\mathrm{d}E$ is the density of states. In this way, the energy difference can be calculated in the KKR Green's function formalism. Mapped to the classical Heisenberg Hamiltonian we find in terms of the scattering operators

$$J_{ij} = \frac{1}{4\pi}\int^{E_\mathrm{F}} \mathrm{d}E\, \Im\,\mathrm{Tr}\left(\hat{t}_{i\uparrow}^{-1} - \hat{t}_{i\downarrow}^{-1}\right)\hat{\tau}_{\uparrow}^{ij}\left(\hat{t}_{j\uparrow}^{-1} - \hat{t}_{j\downarrow}^{-1}\right)\hat{\tau}_{\downarrow}^{ji} \,. \tag{3.67}$$

The arrows denote the spin-up and spin-down operators. This is known as the *Liechtenstein formula*, proposed by Liechtenstein *et al.* in 1987 [100]. The exchange parameters J_{ij} are only calculated up to a certain cluster radius r, where sites i and j are separated by less than r.

3.3.2. Mean Field Approximation

The transition temperature can be derived in a simple *mean-field approximation* (MFA) [105] using the calculated exchange parameters J_{ij}. Usually, a compound consists of several sublattices which we label by μ and ν. To determine the transition temperature, we have to solve the coupled equations [106]

$$\frac{3}{2}k_\mathrm{B}T_\mathrm{N}^\mathrm{MF}\left\langle\mathbf{e}_\mu\right\rangle = \sum_\nu J_{\mu\nu}^0\left\langle\mathbf{e}_\nu\right\rangle \tag{3.68}$$

$$\text{with}\quad J_{\mu\nu}^0 = \sum_{\mathbf{r}\neq 0} J_{\mu\nu}^{\mathbf{r}} \,, \tag{3.69}$$

where T_N^MF is the estimated Néel temperature (in the case of antiferromagnets), k_B is the Boltzmann constant, $\langle\mathbf{e}_\mu\rangle$ is the average z component of the unit vector

$\mathbf{e}_\mu$ in the sublattice μ and $J^{\mathbf{r}}_{\mu\nu}$ represents the interaction between sites in sublattices μ and ν separated by $\mathbf{r}$. The problem can be represented in matrix form:

$$\left(\mathbf{\Theta} - T_{\mathrm{N}}^{\mathrm{MF}}\mathbb{1}\right)\mathbf{E} = 0 \tag{3.70}$$

$$\text{with} \quad \frac{3}{2}k_{\mathrm{B}}\Theta_{\mu\nu} = J^0_{\mu\nu}\ . \tag{3.71}$$

$\mathbb{1}$ is a unity matrix and $\mathbf{E}$ is the vector of $\mathbf{e}_\mu$. $T_{\mathrm{N}}^{\mathrm{MF}}$ is then obtained by solving the eigenvalue problem. The largest eigenvalue of $\mathbf{\Theta}$ corresponds to the transition temperature [105, 106].

3.3.3. Monte Carlo Simulations

Ferromagnetism and antiferromagnetism are collective phenomena, so many characteristic properties of such systems are determined by the interaction between a large number of individual atoms. The transition temperature belongs to this group of properties. An estimation in the MFA as outlined above is a rather rough approximation. A better approach would consider a significant number of atoms or unit cells in order to reduce effects according to the finite size of the system. Numerically, an exact treatment for such large systems is hard if not impossible.

A more feasible way goes back to an idea first published in 1949 by Metropolis and Ulam [107]. Their *Monte Carlo*[4] (MC) method is a stochastical way of solving problems approximately. A prominent example is numerical integration. The space defined by the integration range and the function to be integrated is sampled by N randomly chosen points. The value of the integral is then approximated by the number of points which hit the space below the function. Thus, the quality of the result can be easily improved by increasing the sampling. Of course, this method is applicable to integrals of any dimension. Typically, the error δ in MC methods scales with the inverse square root of the number of trial steps $\delta \propto 1/\sqrt{N}$ [109]. Furthermore, the numerical effort scales linearly with the problem size, a significant advantage for the large problems we are dealing with. The given introduction follows in large parts the article by Walter and Berkama [110]. More details can be found in the textbook of Landau and Binder [109].

[4] The name is "not unrelated to the fact" that an uncle of Ulam borrowed money from relatives to visit a casino in Monte Carlo [108]

Monte Carlo simulation of physical systems

A physical application of a MC method would sample our system's parameter space searching for the state of lowest energy, i.e., the ground state. We note certain states of a system simply as A and B. During the sampling we create a chain of system states, where the state after n steps is X_n. We write the probability of going from state A to state B as a conditional probability

$$W(A \to B) = P(X_n = B | X_{n-1} = A) \; . \tag{3.72}$$

Such a sequence of states is a special case of the so called *Markov chain*. In the more general case, the probability of finding the system in state B at step n can depend on all $n-1$ previous steps. The probability $W(A \to B)$ must fulfill the conditions

$$W(A \to B) \geq 0 \quad , \qquad \sum_B W(A \to B) = 1 \; . \tag{3.73}$$

The first one is natural for a probability and the second one ensures that the system will be in any state after a transition. The MC process applied for physical systems consists of two steps: First, a new state B is proposed based on the current state A of the system (see Eq. (3.72)). Each possible state B is proposed with a certain trial probability $T(A \to B)$. Second, the proposed state B is put into trial and only accepted with a certain, well-defined probability $A(A \to B)$. We therefore decompose the transition probability into

$$W(A \to B) = T(A \to B) \cdot A(A \to B) \; . \tag{3.74}$$

To obtain physically correct results, the Markov chain must meet some basic requirements constraining the probabilities introduced above. First of all, a possibility to reach every system state must be ensured. Otherwise, the MC process would be unable to sample a certain part of the parameter space. Not every state necessarily must be reachable from every other state. This constraint is called *ergodicity*. It corresponds to the Boltzmann distribution of statistical physics, where every state A is found with the probability $P_A = \exp(-E_A/k_B T)/Z > 0$, with the Boltzmann constant k_B, the energy E_A of state A, the temperature T and the partition function Z.

Proposition and acceptance probabilities have to be well chosen so the Boltzmann distribution is resembled by the MC process, which seems difficult at first sight, as we do not know Z in general. We make use of the so-called *master equation*, which describes the evolution of probabilities in a MC process:

$$\frac{dP_A}{dt} = \sum_B \left[W(B \to A)P_B - W(A \to B)P_A\right] \ . \tag{3.75}$$

Here, the "time" t has not to be taken literally in a physical manner but in terms of the MC sampling process. In equilibrium, the derivative vanishes, i.e., $dP_A/dt = 0$. This condition is achieved if the sums are equal, or, in a stronger but not strictly necessary condition, if the summands are pairwise equal:

$$P_A \cdot W(A \to B) = P_B \cdot W(B \to A) \ . \tag{3.76}$$

This condition is called *detailed balance*. By inserting the Boltzmann probabilities it relates the transition probabilities to a term only dependent on the energy difference $E_A - E_B$. Fortunately, the partition function Z drops out:

$$\frac{P_A}{P_B} = \frac{W(B \to A)}{W(A \to B)} = \frac{T(B \to A) \cdot A(B \to A)}{T(A \to B) \cdot A(A \to B)} = \mathrm{e}^{-\frac{E_A - E_B}{k_B T}} \ . \tag{3.77}$$

If we ensure that $T(A \to B) = T(B \to A)$ in our sampling process, we get a prescription for the acceptance probabilities by

$$\frac{W(B \to A)}{W(A \to B)} = \frac{A(B \to A)}{A(A \to B)} = \mathrm{e}^{-\frac{E_A - E_B}{k_B T}} \ . \tag{3.78}$$

The choice of $A(A \to B)$ is free and a key subject of the used algorithm as long as Eq. (3.78) is fulfilled. Thus, the combination of ergodicity and detailed balance ensures that the sampling process resembles the Boltzmann distribution.

Metropolis Algorithm

In this work the *Metropolis algorithm*, developed and published in 1953 by Metropolis *et al.* [111], is used. Originally, they used this technique to solve multidimensional integrals for the evaluation of partition functions. The first approach is to uniformly sample the phase space of a system just by generating

arbitrary configurations and weighting them with their Boltzmann probability $\exp(-E/k_BT)$. However, this method turns out to be inefficient, as the whole phase space is sampled uniformly. This uniform sampling is generally referred to as simple sampling. Physically, in equilibrium only a narrow part in the phase space contributes significantly to measured observables. Thus, many of the configurations in Metropolis' original sampling process only contribute negligibly to the final result.

To overcome this problem, the phase space is sampled according to the Boltzmann probability and the contributions are weighted evenly. This weighted sampling is referred to as importance sampling, as the relevant (important) region of the phase space significantly contributing to the calculation's result is sampled preferably. This is achieved by defining the acceptance probabilities as

$$A(A \to B) := \min\left[1, \exp\left(-\Delta E/k_BT\right)\right] \tag{3.79}$$

with $\Delta E = E_B - E_A$. In other words, a trial state lowering the energy ($\Delta E \leq 0$) is immediately accepted, whereas an increase in energy ($\Delta E > 0$) is only accepted according to the Boltzmann distribution. If the generation of new states fulfills $T(A \to B) = T(B \to A)$, then the conditions of ergodicity and detailed balance are fulfilled by this choice of $A(A \to B)$. The general scheme of the Metropolis algorithm is as follows:

(1) Create a (random) initial state

(2) Change the state of the system randomly

(3) Calculate the energy difference ΔE caused by the change

(4) Generate a random number ζ with $0 \leq \zeta \leq 1$

(5) If $\zeta < A(A \to B)$, apply the change, otherwise discard it

(6) Iterate (2) to (5)

One iteration of points (2) to (5) is called a *Monte Carlo step*. The system will systematically strive to reach a state of lowest energy. However, the algorithm does not ensure to reach a global minimum after a finite amount of steps, therefore a reasonable choice of the initial state is of increased importance. As this initial guess is generally not the ground state, usually a defined amount of MC steps is

performed as a relaxation prior to calculating observables. Observables are then calculated by integrating over several MC steps by

$$\langle Q \rangle = \frac{1}{N} \sum_{i=1}^{N} Q_i \ , \tag{3.80}$$

where $\langle Q \rangle$ is the integrated mean value, Q_i the value for state i and N the number of MC steps.

Implementation for a Classical Heisenberg Model

In Sec. 3.3.1 we showed how to calculate the exchange parameters J_{ij} between atoms i and j for a classical Heisenberg model. The simulation box for the MC process is created by building a large supercell from the unit cell of the J_{ij} calculation. This box usually contains several thousand atoms. Each set of equivalent atoms within is referred to as a sublattice. We then apply the Metropolis algorithm to this system. The energy differences are calculated from the Hamiltonian Eq. (3.65) only containing the orientation of the magnetic moments. As the size of the magnetic moments for the corresponding atoms is included in the exchange parameters J_{ij}, we only deal with unit vectors here. As an initial guess a perfectly ordered collinear configuration is usually chosen. For each MC step, the magnetic moment of a randomly chosen atom is put into trial by rotating it arbitrarily in space. The new state created this way is accepted according to Eq. (3.79). This approach changes only one magnetic moment per MC step but does not violate the ergodicity condition, as every collective change of several moments can be achieved by a consecutive change of single moments. As a side note, besides this simple approach more complex ones to improve the efficiency of the algorithm exist as well [112].

Quantities of interest, such as the magnetization, are calculated according to Eq. (3.80). As the MC process primarily deals with unit vectors $\mathbf{e}_j$, the normalized sublattice magnetization m_i can be easily obtained by

$$m_i = \frac{1}{N_i} \left| \sum_{j=0}^{N_i} \mathbf{e}_j \right| \ , \tag{3.81}$$

where N_i is the number of atoms in sublattice i. The heat capacity c and the normalized sublattice susceptibility χ_i can be derived from fluctuations of the total energy and the magnetization by

$$c = \frac{1}{k_\mathrm{B} T^2} \left(\left\langle E^2 \right\rangle - \left\langle E \right\rangle^2 \right) \tag{3.82}$$

$$\chi_i = \frac{1}{k_\mathrm{B} T} \left(\left\langle m_i^2 \right\rangle - \left\langle m_i \right\rangle^2 \right) \ . \tag{3.83}$$

By repeating a MC simulation for a set of different temperatures usually starting at $T \sim 0$ and increasing, a temperature dependence of, e.g., the magnetization can be studied. This allows us to deduce the transition temperature from ferro- or antiferromagnetism to paramagnetism.

4 Sample Preparation and Analysis

Within this work thin film samples for spintronic applications are investigated. The experimental methods used for their fabrication, analysis, and characterization are introduced in the following sections. The deposition of thin films from an atomic monolayer to several hundred nanometers by *magnetron co-sputtering* and *electron beam evaporation* is discussed in Sec. 4.1. It is crucial that the composition of the sample, e.g. X_2YZ in the case of Heusler compounds, is met precisely in the experiment to avoid the nucleation of different, unwanted compounds. The corresponding composition analysis methods are explained in Sec. 4.2. An introduction to crystal structure analysis methods e.g. using X-rays is given in Sec. 4.3. Analysis methods of intrinsic magnetic and electrical properties are discussed in Sec. 4.4 and Sec. 4.5. Finally, to prepare spintronic devices the samples are patterned by UV lithography. The process is outlined in Sec. 4.6.

4.1. Thin Film Deposition

The thin film samples characterized in this work are mainly prepared by magnetron co-sputtering [113] from elemental targets. These targets, mounted on

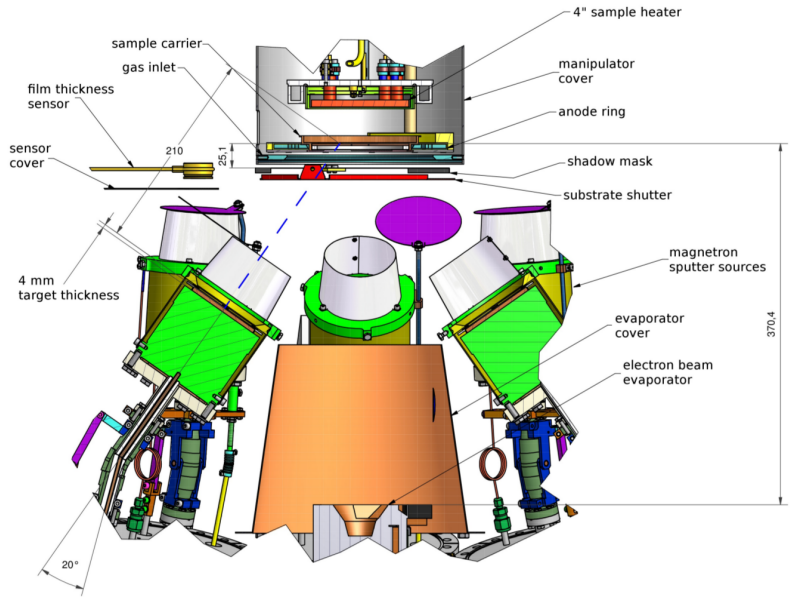

Figure 4.1. | Schematic of the BESTEC magnetron sputter deposition system [114].

the magnetron sources, are bombarded by an argon plasma in vacuum with a typical processing pressure of $2 \cdot 10^{-3}$ mbar. The plasma is ignited by applying a voltage of up to 800V to the target material. The momentum of the electrons in the plasma is transferred to the target material removing single atoms. These are, in turn, deposited on a substrate positioned above the source (sputtering). Creating a suitable magnetic field at the target material forces the electrons to follow helical paths significantly enhancing the deposition yield (magnetron sputtering). A suitable base vacuum is required to reduce contaminations from residual gas in the chamber as much as possible.

Two custom built systems manufactured by BESTEC [114] are used within this work. Both use a confocal geometry of the magnetron sources with the sample carrier in the focus, one equipped with eight 3", one with four 2" magnetron sources. They allow co-deposition from up to four sources at the same time. The sources can be operated with a DC or RF (13.56 MHz) voltage, allowing co-sputtering of both metals and insulators. The magnetrons are operated in

constant-power mode. Deposition rates are controlled by the applied power, so full control of the composition is possible. High purity (6N) Ar gas is used for the sputtering process. To keep the deposition homogeneous across the whole sample, the carrier can be rotated during the process. Furthermore, the carrier is equipped with a radiative heater allowing deposition at substrate temperatures of over 900°C. A cross section of the eight-source apparatus is shown in Fig. 4.1. This apparatus is also equipped with an electron beam evaporator, which is primarily used to deposit MgO tunneling barriers. For this purpose, the evaporator is operated at 6 kV and a current of about 10 mA. Deposition rates can be monitored using a quartz crystal microbalance. Both systems have a base pressure of better than 10^{-8} mbar.

4.2. Composition Analysis

When depositing thin films, accurate control of the composition is crucial. This is necessary to obtain a certain crystal structure and prevent the formation of unwanted, secondary phases. The technique of co-sputtering provides the required tools for adjustments. Analyzing the resulting composition of a sample is discussed in the following sections.

4.2.1. X-ray Fluorescence Spectroscopy

A fast and reliable method of composition analysis is *X-ray fluorescence spectroscopy* (XRF). The material of interest is irradiated with hard X-ray radiation, especially continuous bremsstrahlung, with energy higher than the binding energy of core level electrons in the material's K and L shells. The electrons are excited to continuum and the vacancies eventually filled by electrons of higher levels. The transition into the K or L shell is responsible for either creation of an Auger electron, or emission of a photon (X-ray fluorescence), which has a transition - and therefore element - specific energy. The experimental setup as well as the process is sketched in Fig. 4.2. The most important transitions are K_α, K_β and L_α, L_β (cf. Fig. 4.2c) as the corresponding transitions can be easily excited for most elements. Here, K or L denotes the final shell of the transition and α or β the origin. Due to the reduced absorption cross section for light elements (up to $Z \sim 12$), a reasonable application is limited to the heavier elements.

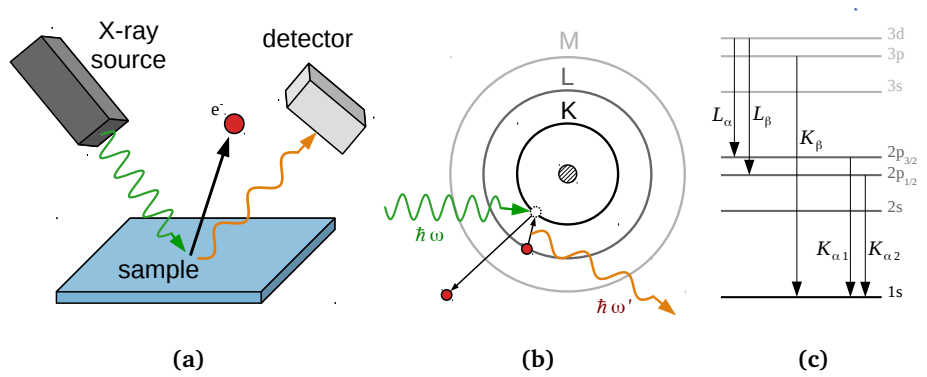

Figure 4.2. | Principle of X-ray fluorescence spectroscopy. **(a)** Experimental setup with X-ray tube and detector. **(b)** Electrons of higher levels fill the vacancies of core levels emitting a photon of material specific wavelength. **(c)** Term diagram of the most relevant transitions. Splitting of $3p$ and $3d$ states is omitted for the sake of legibility.

The resulting emission spectrum is detected by a multi-channel detector. The characteristic peaks are evaluated after removing the background, escape and sum peaks, and smoothing the spectrum. The adjusted spectrum is then evaluated by a fundamental parameter analysis [115] fitting the spectrum without the need of standards. The physical environment of the experimental setup, such as sample and setup geometry, filters, atmosphere, detector, and the X-ray source, is taken into account. X-ray absorption, emission, and secondary absorption and emission are modeled based on tabulated atomic parameters. Evaluation of element specific peaks allows the underlying composition of the irradiated material to be determined.

The thin film samples are usually analyzed in a He atmosphere, as otherwise the characteristic emission of light elements would be absorbed by air distorting the results. The sample is irradiated by an Ag anode X-ray tube, generating X-rays with a typical maximum energy of 40 keV. The spectrum is recorded by an AMPTEK XR-100CR Si-PIN detector. Typically, integrating for one to two hours gives accuracies $\lesssim 1\%$ atomic content. To reduce unwanted peaks due to diffraction on crystalline substrates, samples analyzed with XRF are usually deposited on amorphous glass substrates.

4.2.2. Energy Dispersive X-ray Spectroscopy

The shortcomings of the XRF method can be overcome using the *energy dispersive X-ray spectroscopy* (EDX). The underlying analysis in this method is equal to XRF, however, the excitation of core electrons is done by an electron beam in an electron microscope. The cross section for this excitation does not scale linearly with the atomic number Z, so lighter elements can be considered in this method as well. Furthermore, unwanted diffraction peaks do not occur using this method, so samples deposited on crystalline substrates can be measured with ease. Due to the highly focusable electron beam, a spatial composition analysis is possible by rastering the sample, recording a spectrum at each spatial point.

4.2.3. Rutherford Backscattering and ICP-OES

For calibration and comparison, the composition for some samples in this work was also determined externally by other methods. The first one is the *inductively coupled plasma optical emission spectrometry* (ICP-OES), where the sample is dissolved in an acidic solution. This solution then is sputtered into an inductively coupled plasma. The atoms are excited by the plasma emitting element specific radiation. This spectrum is analyzed similar to the XRF and EDX method.

Additionally, *Rutherford backscattering spectrometry* (RBS) was used. Here, high energy ($\sim$ MeV) ions of hydrogen or helium are shot onto the sample. The energy of the backscattered ions is measured and evaluated in a model of elastic, hard-sphere scattering. The scattering intensity depends on the scattering element, so an analysis of the backscattered spectrum provides information about the composition.

4.3. Structural Analysis

The analysis of structural properties is of major importance for material synthesis. It gives fundamental information about the crystal structure and properties of the material, such as lattice parameters, layer thickness, and roughness. In the following sections the techniques used to characterize the samples in this work are outlined.

4.3.1. X-ray Diffraction

X-ray diffraction is the standard method [116] to examine crystalline materials. The sample is irradiated with X-rays, which are diffracted by the crystal lattice. Diffraction on different layers causes a path difference, so depending on the incident angle of the radiation, constructive interference occurs. The condition for this is given by *Bragg's law*

$$n\lambda = 2d\sin\theta\ , \qquad n = 1, 2, 3, \ldots \tag{4.1}$$

with the wavelength of the incident radiation λ, the crystal lattice spacing d and the diffraction angle θ. This is shown in Fig. 4.3a. The lattice spacing between certain crystal layers in a cubic crystal system (e.g. the Heusler structure) can be expressed by the corresponding Miller indices [hkl] by

$$d = d_{hkl} = \frac{a}{\sqrt{h^2 + k^2 + l^2}}\ , \tag{4.2}$$

where a is the lattice parameter. Irradiating the sample under different angles θ and recording the diffracted pattern gives information about the crystal lattice. All X-ray structure analysis measurements in this work are done in a PHILIPS X'Pert Pro MPD diffractometer, which is equipped with a Bragg-Brentano geometry depicted in Fig. 4.3b. Here, the sample is fixed in the center of a circle on which the X-ray source and the detector are moved against each other. The X-ray tube generates Cu K_α radiation of $\lambda = 1.54187\,\text{Å}$. The detector side is equipped with a graphite monochromator. Scanning the sample by varying ω while 2θ (see Fig. 4.3b for explanation of the angles) is fixed to a position of a Bragg reflection provides information about the relative orientation of crystallites in the sample. These measurements - called *rocking curves* - can indicate the quality of the sample growth. A perfect crystal would yield a very sharp peak at $\omega = \theta$. Real samples, however, consist of many crystallites, which may be slightly tilted relative to each other. This results in small deviations from the ideal Bragg condition Eq. (4.1) for the peak positions. The orientation distribution of the crystallites is found then as a broadening of the rocking curve. Hence, narrow rocking curves are indicative of good and homogeneous crystal growth.

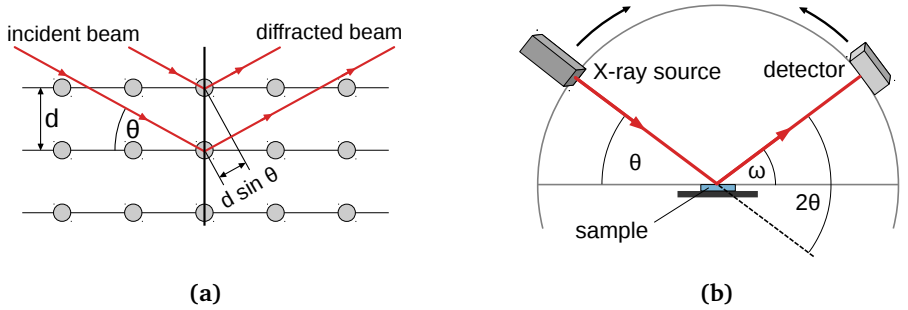

(a) **(b)**

Figure 4.3. | X-ray diffraction in Bragg-Brentano geometry. **(a)** Path difference $d \sin\theta$ of two incident rays diffracted by a crystal lattice leading to Bragg's law. **(b)** Bragg-Brentano geometry used for structural sample analysis. The sample is fixed; X-ray tube and detector are both moved by θ against each other.

4.3.2. X-ray Reflectivity

In a flat angle regime the X-ray beam is reflected on the sample surface depending on the optical properties of the material. This analysis is called *X-ray reflectivity* (XRR) and typically goes to $2\theta < 5°$. Here, below a critical angle θ_c, total reflection occurs. This angle is proportional to the square root of the material's density $\theta_c \propto \sqrt{\rho}$ [116] allowing the determination of ρ. Beyond the critical angle, the reflected intensity drops as the beam enters the material. Furthermore, in the case of multiple layers, the beam is reflected at each interface. The partial beams interfere similar to a Fabry-Pérot interferometer. The resulting intensity oscillates with 2θ and so called Kiessig fringes are observed. The layer thickness can be derived by [116]

$$d = \frac{\lambda}{2} \frac{m - n}{\sin\theta_m - \sin\theta_n} \tag{4.3}$$

for oscillation maxima of order m and n and the corresponding angular positions. If the interfaces deviate from perfect flat surfaces, diffuse scattering of the X-ray beam leads to a decrease in intensity. Thus, information about the interface roughness can be deduced from the oscillation amplitudes.

An XRR analysis consists of measuring the pattern and fitting it numerically using the Parratt formalism [117]. Here, the reflection is simulated by modeling the optical properties of the material. Therefore, information about the material's

composition is required. Layer thickness, roughness and mass density are fit parameters. Thus, especially accurate sputter deposition rates can be obtained from XRR measurements.

4.3.3. Atomic Force Microscopy

Atomic force microscopy (AFM) is used to accurately scan the surface of a sample. Here, a very sharp needle (cantilever) is brought into close proximity of the sample. Between the cantilever and the sample's surface a force occurs affecting the cantilever. There are different approaches to measure this. So called contact-mode methods directly measure the displacement of the cantilever either using a laser or a piezo element. In the tapping mode, the cantilever is given an externally driven oscillation. The oscillation is affected by the forces from the interface and the electric feedback signal gives information about the scanning height.

With this technique, a detailed image of the sample's surface can be obtained, where atomic resolution is possible in modern microscopes. Within this work, mainly the roughness of the surface is investigated using AFM. The corresponding images are recorded in the tapping mode, if not otherwise stated. Information about the surface roughness is obtained by calculating RMS roughness of a scanned sample region by

$$R_{\mathrm{RMS}} = \sqrt{\frac{1}{N}\sum_{i=1}^{N}\left(z_{\mathrm{i}} - \overline{z}\right)^2}\,, \tag{4.4}$$

where z_i is the height at each data point, N the number of data points and $\overline{z}$ the mean height of the N data points.

4.4. Magnetic Analysis

For the magnetic characterization, which is the major aspect of sample characterization, several different methods are used including direct measurement of the magnetization and measuring indirect effects mediated by the sample's magnetism. In the following sections, we discuss these techniques in the form used in this work.

4.4.1. Vibrating Sample Magnetometer

The *vibrating sample magnetometer* (VSM) provides direct access to the magnetic moment of the sample under consideration. The measured signal is an induction voltage in a coil induced by a vibrating magnetic dipole. The setup is rather simple; historically the original VSM was operated with a loudspeaker [118]. The sample is mounted on a carrier which is moved sinusoidally, centered in between a pair of pick-up coils. The number of pick-up coils and their geometry can be modified and extended to match the requirements of the experiment [119]. Due to the vibrating magnetic dipole the magnetic flux through the pick-up coils changes in time resulting in a periodic induction voltage, which is proportional to the amplitude a and frequency ω of the oscillation $U_{\mathrm{VSM}} \propto a \cdot \omega$. Measuring the signal using lock-in amplifiers provides a high sensitivity down to about $1\,\mu$emu. The VSM was not available during parts of this work, therefore other methods providing equivalent information are used as well.

4.4.2. Magnetoresistance

Magnetoresistance covers a wide range of different effects which exhibit a change of resistance dependent on the applied magnetic field in common. Generally, the MR ratio - similar to the TMR ratio in Eq. (2.2) - is defined as

$$\mathrm{MR}(H) = \frac{R(H) - R_0}{R_0} \,. \tag{4.5}$$

The external magnetic field is H and R_0 a defined reference resistance, e.g. $R_0 = R(0)$ for zero field. The resistance $R(H)$ is measured while the magnetic field is swept. In spintronic applications, where the MR value itself is often of primary interest, MR effects can also be utilized to extract quantities of interest such as the switching fields of a sample.

The AMR, already discussed in Sec. 2.2, depends on the relative orientation between the current $\mathbf{I}$ and the magnetization $\mathbf{M}$. An angular dependency of $R(\theta) = R_\perp + \Delta R \cos^2\theta$ is found where θ is the angle between $\mathbf{I}$ and $\mathbf{M}$. $\Delta R = R_\parallel - R_\perp$ is the difference in resistance between $\mathbf{M} \parallel \mathbf{I}$ and $\mathbf{M} \perp \mathbf{I}$. The net magnetization of a material is zero at the switching fields. The resulting resistance at these fields is independent of the field orientation. Therefore, AMR measurements are

normalized to $R_0 = R(M = 0) = R(H_c)$ with the coercivity H_c. As the AMR only depends on θ, for $H = H_c$ a minimum (maximum) in $R(H)$ is found for $\theta = 0°$ ($\theta = 90°$). As shown by Leighton *et al.* in Ref. [120], this effect can be used to measure the coercivity and thus the exchange bias in thin films.

4.5. X-ray Absorption Techniques

The *X-ray absorption spectroscopy* (XAS) is a powerful method to investigate the behavior of single elements in a compound, as the related transitions are element specific. The samples are irradiated with soft X-rays (energy 100 eV - 2 000 eV), which excite core level electrons. The absorption can be quantified in different ways. Auger electrons created by the core holes eventually induce a cascade of secondary electrons, where close-to-surface electrons may leave the sample. The measured drain current when grounding the sample is proportional to the absorbed intensity. This is referred to as the *total electron yield* (TEY). As the mean free path for electrons in the samples is limited to a few nanometers [121], this technique is especially sensitive to the sample volume near the surface. Another option is measuring fluorescence photons of the substrate created by X-rays penetrating the sample. This can be done by placing a photo diode behind the sample and measuring the resulting current. This measurement is called *luminescence yield* (LM). The MgO type substrate has fluorescence lines in a suitable range for detection, whereas this method does not work for $SrTiO_3$ or Si substrates. Both types of measurements are shown in Fig. 4.4a.

For $3d$ transition metal elements the absorption lines under investigation are transitions from the $2p$ into unoccupied $3d$ and $4s$ levels. The absorption, however, is dominated by the transition into the d states by a factor of 20 [122]. For the spin-orbit split $2p$ states transitions originating from the $2p_{1/2}$ states are denoted as L_2, whereas transitions originating from the $2p_{3/2}$ states as L_3. The X-ray absorption XA(E), where E is the photon energy, can give information about the element specific environment. For example, oxidation affects the electronic structure of the atoms, resulting in a shift of the transition lines easily detectable in the absorption spectrum. The absorption spectra of materials, however, can be dichroic. This is utilized to probe the sample's element specific magnetism.

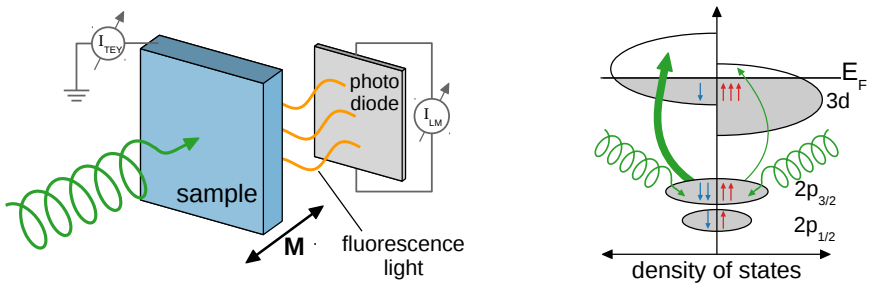

Figure 4.4. | X-ray magnetic circular dichroism. **(a)** Setup measuring the total electron yield I_{TEY} of secondary electrons and the luminescence yield I_{LM} of fluorescence photons. **(a)** Term diagram of the $2p \rightarrow 3d$ transitions. Different helicities of the x-rays result in different transition rates.

4.5.1. X-ray Magnetic Circular Dichroism

By using circular polarized X-rays it is possible to investigate the spin polarization, i.e., ferromagnetism of the sample material. Light of different helicity is absorbed by the sample, which is magnetized parallel or antiparallel to the incident beam direction. Due to the density of states imbalance in the two spin channels of the partially filled $3d$ band, the transition rates from $2p$ states for both helicities differ, resulting in different absorption spectra. These are denoted by $\mu^+(E)$ and $\mu^-(E)$ for the two helicities, where E is the photon energy. This X-ray magnetic circular dichroism (XMCD) [122, 123] is sketched in a simple picture in Fig. 4.4b: The transition rate into the minority spin final states is larger, as there are more unoccupied, final states. The average XA as well as the XMCD signal is obtained by the combination of the two absorption spectra as

$$\mathrm{XA}(E) = \frac{1}{2}\left(\mu^+(E) + \mu^-(E)\right) \tag{4.6}$$

$$\mathrm{XMCD}(E) = \mu^+(E) - \mu^-(E)\ . \tag{4.7}$$

4.6. Lithography

Samples are patterned into nano pillars using standard UV lithography. The raw sample is coated by photoresist (positive resist ALLRESIST AR-P 5350). A ho-

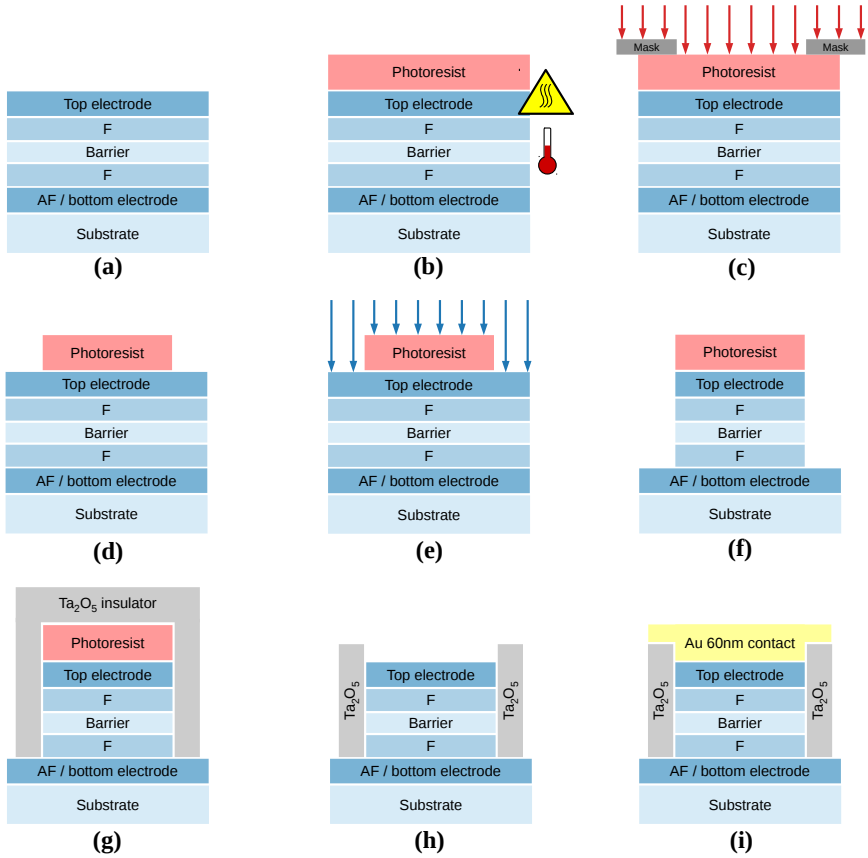

Figure 4.5. | UV-Lithography process. **(a)** Raw sample **(b)** Bake out of the photoresist applied on the sample **(c)** UV exposure with attached mask **(d)** Developed photoresist **(e)** Etching **(f)** Etched sample **(g)** Insulator sputtering **(h)** Liftoff **(i)** Contact pad sputtering

mogeneous coating is achieved by spin-coating the sample for 60 s at 4 000 rpm. The photoresist is baked out at 100°C for 4 min. Next, an optical mask is put onto the sample which is then exposed to a UV light dose of 55 mJ/cm^2. Afterwards, the unexposed portion of the photoresist is removed treating the sample for 60 s with a developer (ALLRESIST AR 300-35). In the next step the sample is etched using Ar^+ ion beam etching under an angle of 35° while rotating the

sample. A quadrupole secondary ion mass spectrometer allows precise control of the etching process. The sample is then covered by an insulating Ta_2O_5 layer approximately 100 nm thick using reactive Ta sputter deposition in an oxygen atmosphere. The remaining photoresist is removed (liftoff) using acetone in an ultrasonic bath. Gold contact pads are added in a second lithography step using sputter deposition. The whole process is sketched exemplarily for a TMR nano pillar in Fig. 4.5.

5

Screening for Novel Antiferromagnetic Heusler Compounds

It is well known that density functional theory has a huge potential in the field of computational material design. Many reports on material search, prediction and optimization can be found in the literature [124–126]. Due to increasing availability of sufficient amounts of computational power, more and more high-throughput frameworks aiming at large-scale material discoveries emerged in the last two decades [127–133]. Today, there are several publically available computational material databases, such as the Materials Project [134, 135], providing detailed calculations of a large number of material properties. These databases differ in their focus, for example in investigated material classes and included elements. One of these databases is the AFLOWLib of which data our investigation is based on.

5.1. AFLOWLib

The AFLOW project [136, 137] investigates binary and especially ternary compounds in a high-throughput framework. They utilize the VASP DFT code, which we already introduced in Sec. 3.2.1, to material ground state properties such as lattice parameters, formation enthalpies, magnetic configurations and band structures. These results are helpful for experimentalists in the search for novel materials exhibiting specific properties. Energetic considerations may indicate if a certain compound is expected to be stable.

The calculations are done combinatorically regarding the included elements, so an unbiased database of material properties for a large variety of element combinations is obtained. Currently, depending on the compound class (elemental, binary, ternary), some elements are not yet included in the calculations. These are elements which are usually hard to handle by DFT calculations (strongly correlated systems) or technologically less relevant (e.g. man-made, radioactive elements). At the time of writing, generally not included are actinides. For the binary compounds, noble gases and most other elements found in the gas phase at ambient conditions are not included. Furthermore, only a few lanthanides are included. In the ternary family, all lanthanides except La are omitted. For the gas-type elements only noble gases are excluded.

For the limited number of binary combinations many different crystal structures are considered in calculations for each combination. In contrast, for ternary compounds the number of possible combinations is already very large. In favor of more combinations the calculations are restricted to a few crystal structures including the Heusler structure. By the time of writing, the AFLOWLib includes calculated properties for more than 330 000 binary and 1.2 million ternary compounds [137]. The binary part of the database builds an important basis of the AFLOWLib, where an intensive investigation of binary phase diagrams has been done. The results are remarkable: The ground state prediction for binary crystal structures is accurate with a 96.7% probability [136]. Hence, an investigation of the Heusler family based on the data available in the AFLOWLib is feasible.

Within a high-throughput approach, several requirements for the investigated materials need to be set up in advance in order to avoid unnecessary computational time. As we are aiming to find new materials for future use in spintronic

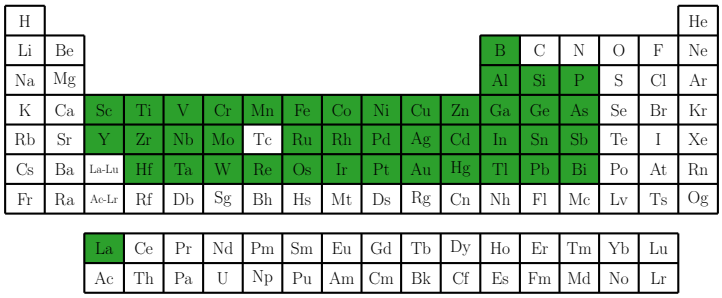

Figure 5.1. | Elements included in the screening process are shown in green.

thin film applications we define three basic criteria for the database search within the AFLOWLib:

1. **Suitable elements** - exclude elements which are not suitable for thin film deposition and processing
2. **Magnetism** - at least one atom needs to have a non-vanishing magnetic moment
3. **Stability** - the material needs to be stable against decomposition into other phases

Besides radioactive elements, we excluded elements not suitable for thin film preparation (alkaline metals, noble gases) or that impose significant constraints on the type of deposition technology (halogens, chalcogens). The full list of included elements is visualized in a periodic table of the elements in Fig. 5.1.

To exclude nonmagnetic materials we restricted our search to compounds, where the sum of the absolute magnetic moments of the constituents is at least $1\mu_{\mathrm{B}}$. To further restrain our search to thermodynamically stable compounds, we considered the formation enthalpy. This is the amount of energy released when forming a compound from the elemental constituents. In the limit $T \to 0$ present in DFT calculations, entropic contributions vanish and the formation enthalpy is equal to the formation energy. For Heusler compounds X_2YZ the formation energy ΔE is

$$\Delta E(X_2YZ) = E(X_2YZ) - 2E(X) - E(Y) - E(Z)\,, \tag{5.1}$$

where $E(X)$ is the total energy of the ground state structure of element X. The formation energy, as well as the magnetic moment is calculated for every compound in the AFLOWLib and available in the online library, which includes a search engine with corresponding filters [137].

5.2. Phase Stability

The formation energy contains information about the possible decomposition into the elemental constituents of a compound. However, a decomposition into other compounds or a mixture of phases can also be energetically favorable. This is not considered in the formation energy alone. In order to ensure stability against phase separation into competing binary and ternary phases, we investigate the so called zero temperature phase diagrams. Here, the formation energies obtained from the DFT calculations are plotted against the atomic composition. The corresponding formation energy values can be obtained through the AFLOWLib API [138], so automatic processing and evaluation is easily possible. For binary systems X-Y this yields a simple two dimensional graph containing a data point for all elemental phases of X and Y and their binary combinations. Elementary phases are included by their total energy with an offset, so the phase of lowest energy has $E = 0$. This is exemplarily shown for the Ge-Mn system in Fig. 5.2a. Especially interesting is the $\Delta E < 0$ part of the graph containing the phases which are stable against elemental decomposition. However, for certain phases other decompositions into further binary phases are possible. To investigate the possibility of decomposition into other phases, the *convex hull* (CH) for the point set with $\Delta E \leq 0$ is calculated. The CH of a point set is the smallest convex subset containing the whole original point set. In Fig. 5.2a, this is marked by the blue line. We calculate the CH using the QHULL tool [139]. As we only consider $\Delta E \leq 0$, the CH always contains the trivial part $E = 0$. As this is of no experimental relevance, we will neglect this part of the CH in the following only discussing the negative part.

The grade of stability can now be evaluated in terms of the CH. Each phase, which is not part of the CH, can separate into two or more phases which *are* part of the CH. The energy gain by this decomposition is characterized by the vertical distance to the CH. We calculate this distance, in the following denoted

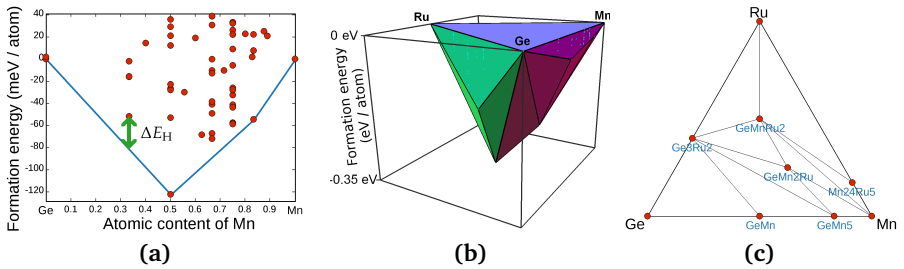

Figure 5.2. | Zero temperature phase diagrams. **(a)** Two-dimensional phase diagram for the Ge-Mn system. The green arrow (↕) indicates the distance to the convex hull ΔE_H. **(b)** Three-dimensional convex hull for the Ge-Mn-Ru system. **(c)** Phase diagram showing the convex hull projection to the xy-plane for the Ge-Mn-Ru system.

by ΔE_H, geometrically. The higher ΔE_H is for a certain phase, the less stable the compound is. Exemplarily, ΔE_H is sketched in for one phase in Fig. 5.2a. Phases, which are part of the CH have no possible decomposition channels into other phases lowering their total energy. Thus, these phases are expected to be stable in the experiment. Of course, a complete phase diagram including every possible phase is required to produce a definite prediction. For ternary compounds this is currently not possible, but nevertheless, as already shown for binary compounds by the AFLOW consortium, this method works remarkably well.

In order to investigate the Heusler family we need to evaluate the full three dimensional, zero temperature phase diagrams for all candidates already fulfilling criteria 1 and 2 defined in Sec. 5.1. The composition for a system X-Y-Z is encoded into an equilateral triangle, where the corners represent the elemental X, Y, or Z phases. The sides of the triangle represent binary compounds, i.e., the binary phase diagrams. Ternary phases containing all three elements are found in the area of the triangle. The formation energies are now plotted on the z-axis resulting in a three dimensional exemplarily CH shown in Fig. 5.2b, where a phase is found at every vertex. Due to this, usually a projection to the xy-plane is printed. For the Ge-Mn-Ru system this is shown in Fig. 5.2c. Here, only phases which are part of the CH, as well as the projected facets of the CH are shown in the diagram. The CH as well as the distance ΔE_H are calculated the same way as for binary compounds. With this information, the three basic criteria from Sec. 5.1 are fulfilled.

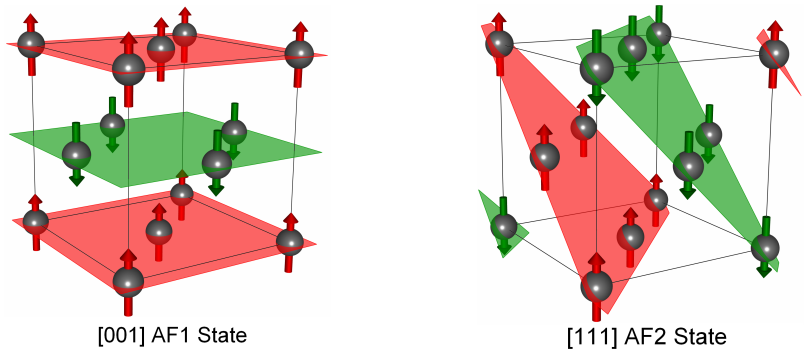

Figure 5.3. | AF configurations in an fcc lattice. Shaded planes indicate parallel aligned magnetic moments (arrows). **(a)** AF1 state with staggered magnetization in [001] direction. **(b)** AF2 state with staggered magnetization in [111] direction. Sketches are created with VESTA [140].

5.3. Magnetic Ground State

Up to now, our screening task has only used data already available in the AFLOWLib. This yields a set of Heusler compounds only containing the elements we chose to include, containing at least one magnetic constituent and being stable against elemental, binary and ternary phase decomposition. The calculations included in the AFLOWLib only consider structural unit cells. However for AFs, the magnetic unit cell can be larger than the structural one. For example, this is the case for an AF Heusler compound, where Y atoms are coupled antiferromagnetically in neighboring structural, four atom unit cells. As this is not yet covered by the AFLOW framework, we need to put further effort into determining the magnetic ground state.

To check for antiferromagnetism in the candidate materials filtered from the AFLOWLib as described in the previous section, we investigate the two AF configurations AF1 and AF2. These are sketched in Fig. 5.3. The grey spheres represent atoms in an fcc lattice. Their arrows show the orientation of their magnetic moments. The shaded areas indicate the corresponding alternating planes of parallel magnetic moments. In the AF1 state (Fig. 5.3a), the magnetic moment orienta-

tion is staggered in the (001) planes; in the AF2 state (Fig. 5.3b) the magnetic moment orientation is staggered in the (111) planes. Due to the inversion symmetry, all $\{001\}$ or $\{111\}$ arrangements are equivalent. For our investigations we use eight-atom unit cells maximizing the symmetries for the corresponding configurations. Detailed information about the used geometry and unit cells are given in the appendices, see Chapter A.

Our investigations are done using the VASP DFT code (cf. Sec. 3.2.1) just as used in the AFLOWLib. We use the generalized gradient approximation with the Perdew-Burke-Ernzerhof (PBE) [87] exchange-correlation functional. This functional is widely used in solid-state physics and known for its good performance in reproducing formation energies and structures for solids [141–143]. To keep calculations as consistent as possible, for all investigated compounds the same PAW potentials as used in the calculations found in the AFLOWLib are used.

We investigate the energy differences of AF configurations to the structural unit cell by setting up three distinct calculations for every candidate material. In the following, we will refer to the state found in the structural unit cell simply as the FM state[1]. In addition to this, we calculate the AF1 and AF2 states using supercells. Initially, we set the magnetic moments of all atoms to a high-spin configuration according to Hund's rules. For the AF configurations magnetic moments are aligned parallel within a structural unit cell and antiparallel to neighboring unit cells. All calculations are done assuming collinear magnetism neglecting spin-orbit coupling, thus, the orientation of the magnetic moments with respect to the lattice plays no role. In order to predict AF ground states we calculate the total energy differences to the FM state by

$$\Delta E_{\mathrm{AF1}} = E_{\mathrm{AF1}} - E_{\mathrm{FM}}\,, \tag{5.2}$$

$$\Delta E_{\mathrm{AF2}} = E_{\mathrm{AF2}} - E_{\mathrm{FM}}\,, \tag{5.3}$$

where E_{FM}, E_{AF1}, and E_{AF2} are the total energies per four-atom formula unit (f.u.) obtained from the calculation of the respective states.

The calculations on all three states are done for all candidate materials. They include an ionic quasi-Newton relaxation [144] by calculating forces and the

[1] The magnetic state found in this calculation is not ad-hoc clear and usually requires further investigation, as due to periodic boundary conditions and $T \to 0$ the "true" magnetic coupling cannot be directly accessed.

stress tensor relaxing all internal degrees of freedom and the lattice parameters. This is a necessary step as the Coulomb repulsion for differently aligned magnetic moments can lead to lattice distortions. We performed extensive convergence tests on crucial numerical parameters. These are set to achieve a total energy convergence down to 1 meV. The convergence checks are discussed in the appendices, see Chapter B.

In addition to this, to cover shortcomings in the convergence tests and to cope with the large variety of candidate materials, a fourth calculation in the AF1 configuration using fewer $\mathbf{k}$-points is added. As a simple, automatic convergence test, the total energy convergence between the AF1 and reduced $\mathbf{k}$-point AF1 calculation is evaluated and, if necessary, calculations are repeated using more $\mathbf{k}$-points automatically until the desired convergence is achieved. Furthermore, substantial changes in the lattice parameters and/or magnetic moments are detected automatically and reviewed manually. Finally, the magnetic ground state is determined by the total energy: If one of the energy differences ΔE_{AF1} and ΔE_{AF2} is negative, the ground state is AF, at least within our framework.

5.4. Néel Temperature Estimation

To estimate Néel temperatures for materials we predict to be AF we use the Munich SPR-KKR package (cf. Sec. 3.2.2). As outlined in Sec. 3.3.1, it provides tools to calculate the Heisenberg exchange parameters. In order to do so, the ground state calculation for the corresponding AF configuration needs to be repeated in the SPR-KKR code. We use the fully relaxed and converged results from the calculations done with VASP as a starting configuration for the SPR-KKR code. The size and orientation of magnetic moments used in the calculation are obtained from previous results.

We use the full-potential mode to accurately reproduce the previous results. The angular momentum cutoff[2] is set to $l_{\max} = 3$. The Brillouin zone integration is done on 1 000 $\mathbf{k}$-points, which corresponds to a dense $20 \times 20 \times 20$ mesh. The integration of the Green's function is done on an arc with 60 energy points in the complex plane. These tight numerical parameters ensure convergence for all

[2] In the current version of the code used in this work, this is the maximum value supported by the code.

investigated materials. In a second step, we calculate the Heisenberg exchange parameters on a cluster with a radius of $r = 4.5a$ in real-space.

A first estimation of the Néel temperature is obtained in the mean field approximation (cf. Sec. 3.3.2). As the value $T_{\mathrm{N}}^{\mathrm{MF}}$ obtained from Eq. (3.69) typically overestimates the Néel temperature [145], we performed atomistic spin dynamic simulations using Monte Carlo (MC) methods for all candidate materials with a predicted AF ground state. This is a viable method to obtain excellent results [146]. We use a custom implementation of the Metropolis algorithm as explained in Sec. 3.3.3.

MC simulations are done on a temperature range up to $T^{\max} = 1.25 \cdot T_{\mathrm{N}}^{\mathrm{MF}}$ for a simulation box of 8 000 unit cells with periodic boundary conditions. In the case of two magnetic atoms in the unit cell, within the interaction radius of $r = 4.5a$ about 1 600 interactions/atom are included. For four atoms, the number increases to about 3 000 and for six atoms to about 5 000 interactions/atom. Each system is initially relaxed at $T = 0.05 \cdot T^{\max}$. The temperature step size is set to approximately $T^{\max}/100$. For each temperature step 2 000 MC steps per atom are performed as a relaxation, using the previous configuration as a starting configuration for the new temperature. The relaxation is followed by an integration over 20 000 MC steps per atom. All relevant parameters are carefully checked (see appendix Chapter B) and summarized in Tab. 5.1. At each temperature we calculate the normalized sublattice magnetizations m_i (see Eq. (3.81)), the heat capacity from fluctuations c_F (see Eq. (3.82)) and the magnetic sublattice susceptibilities χ_i (see Eq. (3.83)). Furthermore, we derive the heat capacity c_{S} as the numerical derivative of the total energy. All of these are shown for the

Table 5.1. | MC parameters as used in the screening process

Parameter	Value
Simulation Box	$20 \times 20 \times 20$ (8 000 unit cells)
Interaction radius	$4.5a$
Initial relaxation steps	20 000 / atom
Relaxation steps	2 000 / atom
MC steps	20 000 / atom

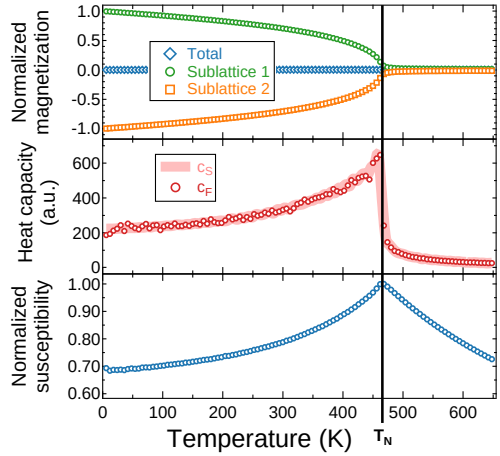

Figure 5.4 | Determination of the Néel temperature. Normalized magnetization (top), heat capacity (middle) and normalized susceptibility (bottom) for Mn_2PtAu in the AF1 state are shown. The solid vertical line indicates the Néel temperature.

Mn_2PtAu system in the AF1 state in Fig. 5.4. Both c_F and c_S match precisely. The susceptibility decreases to 2/3 of its maximum for $T \to 0$ as expected for antiferromagnets. The heat capacity shows a divergence at the phase transition. Fitting a cubic spline to the total energy and determining the steepest decay using the second derivative yields the transition temperature most reliably, thus all Néel temperatures T_N^MC are determined this way.

5.5. Prediction of Antiferromagnetic Heusler Compounds

We started our screening process with more than 80 000 Heusler compounds present in the AFLOWLib. By database filtering using the criteria defined in Sec. 5.1 we find $\approx$ 30 000 Heusler compounds with $\Delta E < 0$. After discarding compounds with a magnetic moment of less than $1\mu_\mathrm{B}$/f.u., the number reduces to $\approx$ 5 000. At this point, our own computational work starts by calculation of the CHs for all of these ternary systems. We end up with a number of 74 Heusler compounds which are part of the respective CH. Now we introduce a meta stability cutoff of $\Delta E_\mathrm{H} < 80\,\mathrm{meV/atom}$ accounting for numerical inaccuracies. For the well-known stable Heusler prototype Cu_2MnAl we find $\Delta E = 64\,\mathrm{meV/atom}$ consistent with other computational material databases such as the Materials Project,

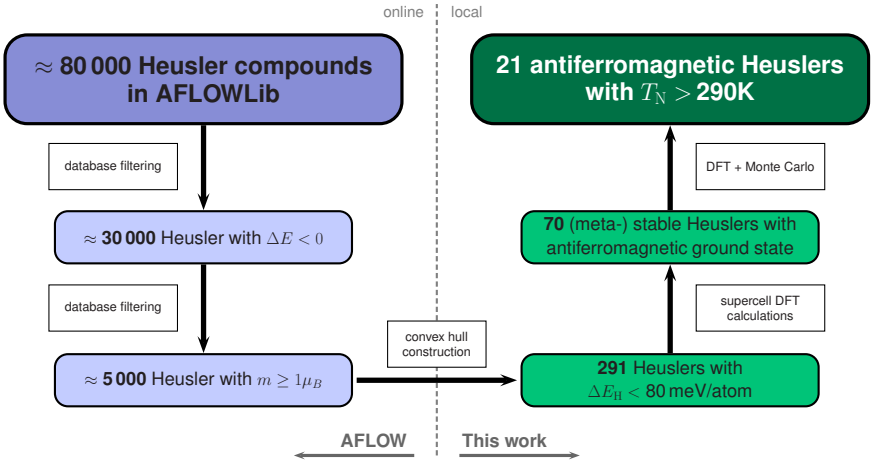

Figure 5.5. | The screening workflow. The left part (purple) shows data already present in the AFLOWLib. The right part (green) reflects the extended calculations done in this work.

justifying this cutoff. Furthermore, because AF configurations of compounds are not included in this consideration, a compound above the CH can become part of it in the AF state due to the energy gain. Our results support this assumption. Taking into account this cutoff, we find a sizable number of 291 magnetic Heusler compounds we expected to be stable in the experiment.

For these 291 compounds we performed magnetic ground state investigations as described in Sec. 5.3. We obtain a negative ΔE_{AF1} or ΔE_{AF2} in 70 cases, which we refer to in the following as "stable". A stable AF1 state is found in 37 cases and a stable AF2 state in 48 cases. 17 compounds are found to be stable in both AF configurations. We performed an estimation of the Néel temperature following the method described in Sec. 5.4 for each stable AF compound separately. The results are wide spread, however, we identify 21 AF Heusler compounds with Néel temperatures above room temperature $T_{\mathrm{N}}^{\mathrm{MC}} > 290\,\mathrm{K}$. Our complete workflow as well as the corresponding numbers are summarized in Fig. 5.5. Due to the huge amount of data, only partial aspects are discussed. A whole set of obtained energetic, structural and magnetic data for each of the 70 investigated Heusler compounds can be found in the appendix Chapter C.

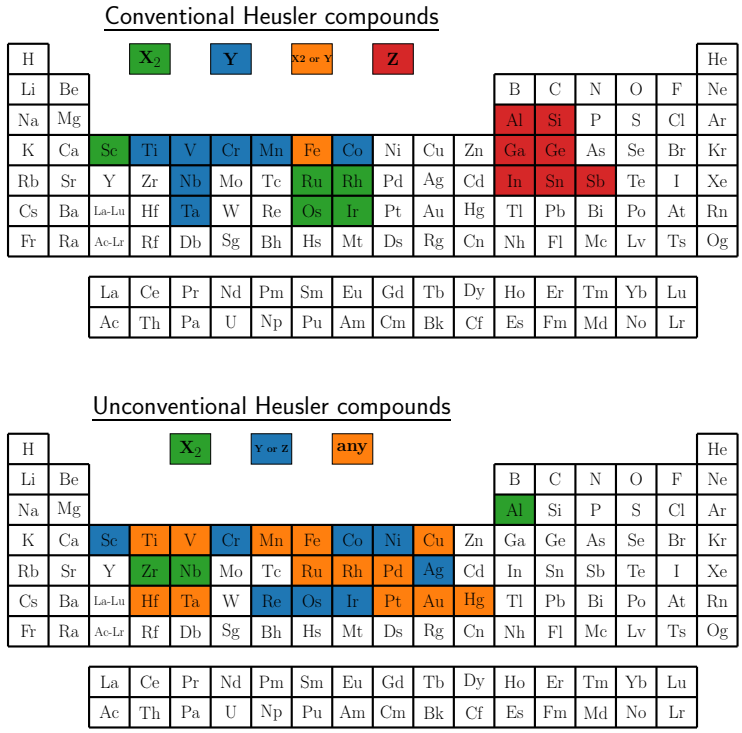

Figure 5.6. | Distribution of elements on the different atomic positions in AF Heusler compounds for conventional ones (top) and unconventional ones (bottom).

5.5.1. Structure and Composition

The AF compounds are divided into two groups, the conventional Heusler compounds, where the Z position is occupied by a main group element, and unconventional Heusler compounds, which are mainly pure intermetallic compounds. Calculations on unconventional Heusler compounds were mainly carried out by Kevin Diekmann within a Master's thesis [147]. We find an interesting elemental distribution among the conventional Heusler compounds: Here, the X position is occupied by platinum group metals (Ru, Rh, Os), Ir, and Sc only. The Y position is taken by $3d$ transition metals Ti, V, Cr, Mn, Fe, Co, Nb, and Ta. This distribution is visualized in Fig. 5.6. In the upper part, the distribution among conventional

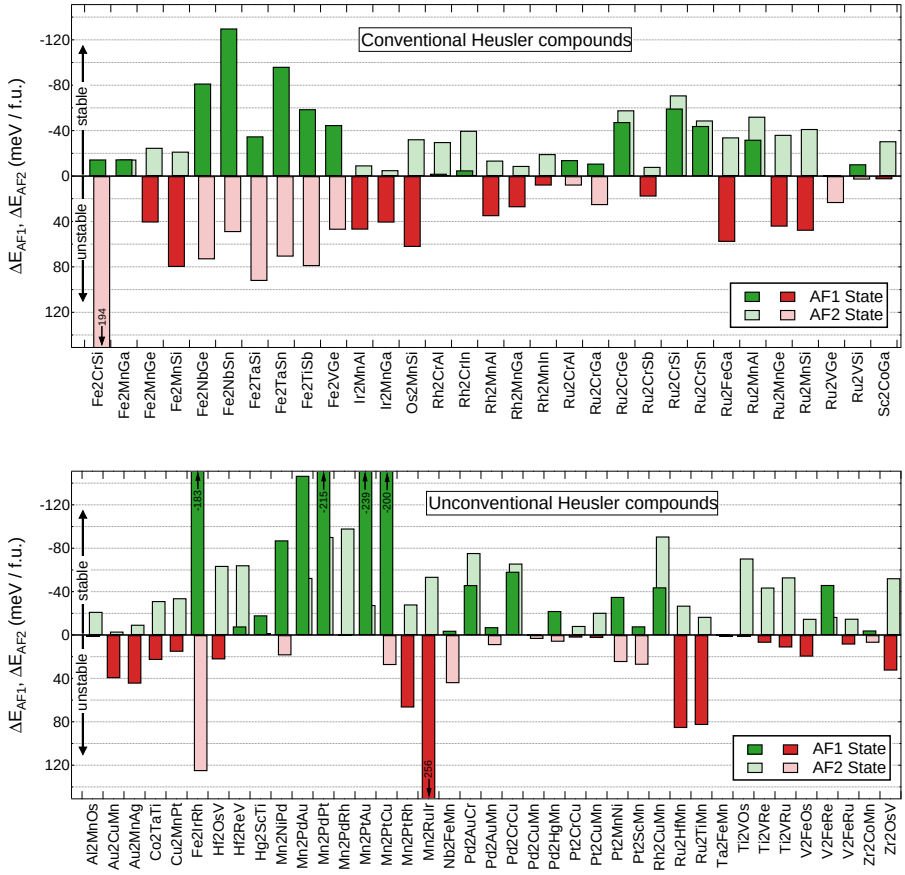

Figure 5.7. | Energy differences ΔE_{AF1} (solid bars) and ΔE_{AF2} (light bars) for AF Heusler compounds. Green bars indicate stable, red bars unstable AF states. The top graph shows conventional and the bottom graph unconventional Heusler compounds.

Heusler compounds is shown. In the lower part, the same is sketched for unconventional ones. In this case, there is no clear tendency; many different combinations without a preference can be found. As a side remark, with one exception (Co_2TaTi), no compound from the well-known family of ferromagnetic Co-based compounds is found to be AF in the screening. In Fig. 5.7 we compare the en-

ergy differences ΔE_{AF1} (solid bars) and ΔE_{AF2} (light bars) for all 70 AF Heusler compounds. Negative energies (stable) are shown in green, positive ones (unstable) in red. Again, conventional Heusler compounds are plotted in the upper part and unconventional ones in the lower. The first result is that no correlation between the two AF configurations is found: One stable AF configuration does not imply the other to be stable as well. Besides Fe- and Mn- based compounds (Fe_2YZ, Mn_2YZ) there is no clear tendency found between included elements and the resulting energy differences. The largest (negative) energy difference is $\Delta E_{\mathrm{AF1}} = -239\,\mathrm{meV/f.u.}$ for Mn_2PtAu in the AF1 state. For Fe- and Mn- based compounds the largest energy differences are found. This is most likely due to the fact that the Fe and Mn atoms, naturally carrying a large magnetic moment, occupying the X position. In an AF configuration this leads to a distortion in the crystal lattice which is indeed found in the calculations for these compounds. Due to symmetry, this distortion is only found in the AF1 state. Here, we find a contraction in [001] direction of typically 3-5% for the Fe- and Mn-based compounds. The unit cell volume remains approximately the same in these cases. For all other compounds, such distortions are negligible. Generally, the equilibrium lattice constants typically differ from the FM state in a sub-permille range.

5.5.2. Magnetism

The magnetic moment for the investigated compounds is almost exclusively localized on the Y atom. Another exception are the Fe- and Mn- based compounds, where a significant moment is found on the X atom. For the absolute magnetic moment $m_{\mathrm{abs}} = \sum_i |m_i|$ per atom we find a Slater-Pauling like behavior, as can be seen by plotting m_{abs} as a function of the number of valence electrons n_{val} per atom in Fig. 5.8a. All three configurations FM (green), AF1 (blue), and AF2 (orange) are shown. Additionally, data for binary compounds (adopted from Ref. [148]) is included in the graph as black dots. Here we find many compounds that approximately follow the well-known Slater-Pauling rule (light blue lines) $m = n_{\mathrm{val}} - 24$ in units of μ_{B} for Heusler compounds. Furthermore, some of the compounds seem to follow the $m = n_{\mathrm{val}} - 18$ rule for the half Heusler structure [148].

The calculated Néel temperatures cover a wide range from nearly 0 K to 956 K. Corresponding values for all investigated AF Heusler compounds can be found in

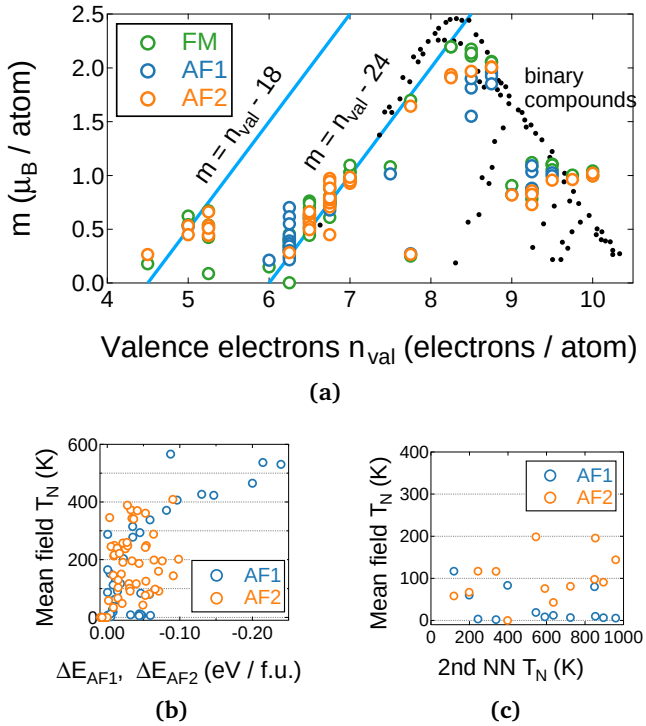

Figure 5.8. | Correlations between several values. **(a)** Magnetic moments m of the investigated Heusler compounds plotted against the number of valence electrons n_{val}. A Slater-Pauling like behavior (light blue lines) is found. The black dots are data for binary phases adopted from Ref. [148]. **(b)** Mean field Néel temperature $T_{\mathrm{N}}^{\mathrm{MF}}$ plotted against the energy differences ΔE_{AF1} and ΔE_{AF2}. **(c)** Mean field Néel temperature $T_{\mathrm{N}}^{\mathrm{MF}}$ plotted against the second nearest-neighbor model Néel temperature $T_{\mathrm{N}}^{\mathrm{2nn}}$ where applicable.

the appendix Chapter C. The highest temperature for the AF1 state is obtained for Fe_2IrRh at 956 K and in the AF2 state it is 520 K for Mn_2PdAu. Slightly higher Néel temperatures are found for compounds with larger magnetic moments. Beside that, no further notable correlations between energy differences, magnetic moments and calculated transition temperatures are found.

The comparison between $T_{\mathrm{N}}^{\mathrm{MF}}$ and $T_{\mathrm{N}}^{\mathrm{MC}}$ obtained in the mean field approximation and by MC reveals the usual trend of $T_{\mathrm{N}}^{\mathrm{MF}} > T_{\mathrm{N}}^{\mathrm{MC}}$. In Fig. 5.8b we compare the resulting $T_{\mathrm{N}}^{\mathrm{MF}}$ with the energy gain in the AF configurations ΔE_{AF1}

and ΔE_{AF2}. A weak correlation between the energy gain and the Néel temperature is evident, although there are many examples that have small energy gain but still large Néel temperature.

Now we investigate the transition temperatures in a second nearest-neighbor model. For compounds of the X_2YZ, type where only Y has a magnetic moment, the first and second neighbor exchange interactions J_1 and J_2 can be written as

$$\begin{aligned} \Delta E_{\mathrm{AF1}} &= 8J_1, \\ \Delta E_{\mathrm{AF2}} &= 6J_1 + 6J_2. \end{aligned} \tag{5.4}$$

In the mean-field approximation one can now write the Néel temperature as $\frac{3}{2}k_{\mathrm{B}}T_{\mathrm{N}}^{2\mathrm{nn}} = |12J_1 + 6J_2| = |\frac{3}{4}\Delta E_{\mathrm{AF1}} + \Delta E_{\mathrm{AF2}}|$. Where applicable (stable in both AF configurations, magnetic moment only on Y atom), we compare $T_{\mathrm{N}}^{\mathrm{MF}}$ with the values of T_{N}^{2nn}. This is the case for 13 compounds and plotted in Fig. 5.8c. It turns out that the second-nearest neighbor model greatly overestimates the Néel temperature in most cases and no clear correlation between the two Néel temperature estimations is observed. These results indicate that interactions at much longer range play a significant role in determining the transition temperature. Thus, especially the second nearest-neighbor approach is insufficient here; a detailed evaluation taking long range interactions into account is mandatory.

Finally, we note an interesting observation during the MC calculations. In many cases, the sublattice magnetizations of the AF1 or AF2 planes were found to vanish for all temperatures, although the total energy, the heat capacity and the susceptibility showed a phase transition at nonzero temperature. This phenomenon occurs when the real magnetic ground state created by the MC simulation differs from the ground state that was expected (AF1 or AF2). The ground state does not consist of the expected alternating planes, which results in an incorrect calculation of the sublattice magnetization. In order to quantify this phenomenon we calculated the quasi spin-spin correlation function

$$\zeta = \frac{1}{N^2} \sum_{i=1}^{N} \sum_{j=1}^{N} |\mathbf{S}_i \cdot \mathbf{S}_j| \ . \tag{5.5}$$

Due to the antiparallel orientation of spins in an AF, many values connected to the alignment of spins are naturally not distinguishable from a paramagnetic phase.

This is not the case for the absolute value of the scalar product, as it neglects the difference between parallel and antiparallel orientations. Therefore, ζ can take values in the interval [0.5, 1], where $\zeta = 1$ corresponds to perfect collinearity between all spins and $\zeta = 0.5$ to a highly non-collinear state. Accordingly, $\zeta = 0.5$ is found for the paramagnetic phase. We evaluated ζ at $T \to 0$ for all AF Heusler compounds to get an impression how well the MC simulation reproduces the expected ground state.

We find that for 16 out of 37 compounds in the AF1 state the MC simulation reproduces the ground state as expected. For a further four compounds, we find a collinear ground state, however, different from the expected AF1 configuration. In the case of the AF2 state, we find twelve out of 48 compounds having a ground state as expected. A further seven compounds have a collinear ground state. No clear scheme can be found in cases where both AF states are energetically lower than the FM state. Neither one of the states is preferably reproduced in the MC simulation, nor a collinear or non-collinear state. This investigation shows that the real AF ground state for many compounds is more complex than a pure antiparallel alignment. We explain this behavior by the fact that the ground state determination using DFT is done using collinear calculations. The true ground state might show a more complex arrangement of the moments, e.g., a frustrated state, a spiral state or a Kagome lattice. It is remarkable that although an AF1 or AF2 ground state is enforced in the DFT calculation, the resulting Heisenberg exchange parameters create a different ground state in the MC simulation.

5.5.3. Selected Compounds and Literature

On the following pages, two tables summarizing the most relevant data are given. At first, in Tab. 5.2, the 21 Heusler compounds we predict a Néel temperature $T_{\mathrm{N}}^{\mathrm{MC}}$ above room temperature for are listed. As a measure for stability in the experiment, the energy difference to the CH ΔE_{H} is given. The Néel temperature for the most stable AF configuration is given. In cases where $T_{\mathrm{N}}^{\mathrm{MC}}$ is higher for the other configuration, the corresponding value is given in brackets. Notably, the AF2 state is found more often than the AF1 state. Unfortunately, it turns out that the majority of the Heusler compounds with high Néel temperature have a fairly large distance from the CH. It has to be left to experiment to assess the stability of these phases in both bulk as well as thin film forms. To the best of our

Table 5.2. | Heusler compounds with a predicted Néel temperature $T_{\mathrm{N}}^{\mathrm{MC}}$ above room temperature. The energy difference to the CH ΔE_{H} and the AF configuration of lowest energy is shown. If the Néel temperature is higher for other AF configuration, it is given in brackets. Experimental Néel temperatures are given where available.

Compound	$\mathrm{T_N^{MC}}$ (K)	ΔE_{H} (meV/atom)	State	$\mathrm{T_N^{exp}}$ (K)
Al_2MnOs	308	72	AF2	—
Au_2CuMn	316	31	AF2	—
Fe_2IrRh	956	54	AF1	—
Fe_2NbGe	310	16	AF1	—
Fe_2NbSn	355	44	AF1	—
Fe_2TaSn	338	68	AF1	—
Hf_2ReV	177 (369)	72	AF2	—
Mn_2NiPd	819	71	AF1	—
Mn_2PdAu	385 (520)	40	AF1	—
Mn_2PdPt	442	0	AF1	—
Mn_2PdRh	192 (873)	6	AF2	—
Mn_2PtAu	462 (495)	35	AF2	—
Mn_2PtCu	373	53	AF2	—
Os_2MnSi	396	18	AF2	—
Pd_2AuCr	225 (747)	65	AF2	—
Pd_2CrCu	166 (408)	61	AF2	—
Ru_2FeGa	308	2	AF2	(*) [149]
Ru_2HfMn	409	77	AF2	—
Ru_2MnGe	307	0	AF2	353 [20]
Ru_2MnSi	365	0	AF2	313 [22]
Ru_2TiMn	348	51	AF2	—

(*) Antiferromagnetism predicted

Table 5.3. | Most stable AF Heusler compounds ($\Delta E_{\mathrm{H}} = 0$). The corresponding Néel temperatures are given for the AF configuration of lowest energy. If the Néel temperature is higher for the other AF configuration, it is given in brackets. Experimental Néel temperatures are given where available. Compounds synthesized in experiments, but not yet investigated magnetically, are marked with *stable*.

Compound	T_N^{MC} (K)	State	T_N^{exp} (K)
Fe_2VGe	252	AF1	—
Ir_2MnAl	192	AF2	500 [150]
Ir_2MnGa	190	AF2	65 [151]
Mn_2PdPt	442	AF1	—
Mn_2PtRh	189	AF2	—
Pd_2AuMn	177	AF1	—
Pd_2CuMn	244	AF1	—
Rh_2MnGa	163	AF2	stable [152]
Rh_2MnIn	103	AF2	stable [152]
Ru_2CrAl	83	AF1	—
Ru_2CrGa	98	AF1	—
Ru_2CrGe	37	AF2	13 (AF2) [153]
Ru_2CrSi	41	AF2	14 [154]
Ru_2MnAl	37 (50)	AF2	stable [155]
Ru_2MnGe	307	AF2	353 [20]
Ru_2MnSi	365	AF2	313 [22]
Ru_2VGe	75	AF1	paramagnetic [156]
Ru_2VSi	69	AF1	stable [155]

knowledge, most of these compounds are not yet investigated experimentally. For only three of them, Ru_2FeGa, Ru_2MnGe, and Ru_2MnSi, published data can be found in the literature. For Ru_2FeGa, antiferromagnetism has been predicted. Experimentally determined Néel temperatures for the other two are within a 20% error margin of our investigations.

In contrast to this, in Tab. 5.3 we summarize the most stable AF Heusler compounds with $\Delta E_{\mathrm{H}} = 0$. The corresponding Néel temperatures of the most stable configurations are given as well. Similarly, the value for the other configuration is given in brackets if higher. Only three compounds, Mn_2PdPt, Ru_2MnGe, and Ru_2MnSi are predicted to have Néel temperatures above room temperature. Ru-based compounds make up half of the compounds that are stable according to our analysis. Here, experimental data is available for most of the compounds. These experiments confirm our predictions. The experimental Néel temperatures resemble the predicted ones well, except for the Ir-based compounds. Differences between the predicted temperatures and the experimentally determined ones may be attributed to the fact that the true AF ground state may differ from AF1 or AF2, as already stressed in the previous section.

Additional information for all 70 investigated AF Heusler compounds can be found in the appendices (see Chapter C). Generally, our predictions of the magnetic ground states are confirmed by experiments: For ten of the compounds, AF phases were experimentally confirmed in agreement with the predictions; neutron diffraction analyses of Ru_2CrGe [153] and Ru_2MnGe [21] identified an AF2 state in agreement with our prediction. Five additional compounds we predict to be AF already have been investigated experimentally and found to be stable, however, no magnetic measurements have been published yet. Additionally, Ru_2FeGa, was already predicted to exist in an AF state [149], but has not been experimentally confirmed.

There are four compounds that require additional discussion: Experimentally, Fe_2CrSi and Fe_2TiSb are found to be unstable [157, 158], Ru_2CrSn shows a spin glass behavior [153], and Ru_2VGe is found to be paramagnetic [156]. For Fe-Ti-Sb, a disordered, more stable phase ($Fe_{1.5}TiSb$ [158]) not included in the AFLOWLib exists. For Fe_2CrSi the distance to the convex hull $\Delta E_{\mathrm{H}} = 76.1\,\mathrm{meV/atom}$ is quite high (but still within our tolerance), which means it is very likely that this compound is unstable in the experiment. For Ru_2VGe we have to consider that our calculations (as well as the AFLOWLib calculations)

are based on the Perdew-Burke-Ernzerhof generalized gradient approximation, which systematically overestimates the lattice constants of most solids [141] due to too strong exchange energy. For compounds on the verge between ferro- and paramagnetism, the enlarged lattice constant and enhanced exchange interaction may give rise to a nonzero ordering temperature contrary to the experiment. As we consider only two highly symmetric AF states, we are not able to correctly identify more complex states such as spin spirals or glassy states.

5.6. Limitations and Extensions

Despite the fact that our systematic approach shows excellent selectivity, it is limited by several aspects. Besides the main limitation due to available computational power, the accuracy of the convex hull calculations strongly depends on the number of phases used in the calculation. There may exist more binary and especially ternary phases not considered in the calculations, rendering a compound stable which actually is not. Furthermore, to allow for some tolerance in the convex hull calculation to include phases that are known to be stable by experiment, we introduced a cutoff for the distance to the CH, ΔE_{H}. Compounds with $\Delta E_{\mathrm{H}} < 80\,\mathrm{meV/atom}$ are considered potentially stable, although they might not be, as in the case for Fe_2CrSi. Also, atomic disorder was neglected. Atoms in the Heusler structure may mix, e.g., between Y and Z sites, leading to a reduction in order, which can seriously affect the magnetic properties. For example, the B2 ordered compound Ni_2MnAl is AF, although the $L2_1$ ordered phase is F [159]. The Néel temperature can also be affected by the degree of order in the compound [160]. Within our calculations we only included two collinear AF states, AF1 and AF2. However, there is in principle an infinite number of possible AF arrangements. More complex ground states including non-collinear spin spiral or frustrated states are yet to be investigated. Our investigation of spin-spin correlations underlines this. This task may be subject to a hybrid DFT + MC method, where the magnetic ground state obtained from the MC simulation is fed back into a DFT calculation in a self-consistent way. However, despite these possible shortcomings, we claim to have identified essentially all possible, fully ordered AF Heusler compounds with either AF1 or AF2 ground state, that are suitable for applications in spintronic devices. Within a review of the literature, we have

Table 5.4. | Heusler compounds with magnetic moments on X atoms investigated for the AF3 type antiferromagnetism. The table shows the energy difference to the ferromagnetic state ΔE_{AF3}, the calculated Néel temperature $\mathrm{T_N^{MC}}$ and the c/a lattice parameter ratio.

Compound	ΔE_{AF3} (meV/atom)	$\mathrm{T_N^{MC}}$ (K)	c/a
Co_2TaTi	-16	— (*)	1.00
Mn_2NiPd	-571	1 253	1.37
Mn_2PdPt	-535	1 122	1.36
Mn_2PdRh	-57	510	1.00
Mn_2PtAu	59	—	1.00
Mn_2PtRh	29	—	1.00
Mn_2RuIr	-32	265	1.01

(*) Unable to reproduce ground state with SPR-KKR

found only one additional AF Heusler compound not identified by our screening: Fe_2VSi. This is due to the fact that it has a very low magnetic moment of 0.74 μ_{B}/f.u. [161], which is excluded in one of our first steps.

The framework we established can be easily extended to either related crystal structures such as the inverse Heusler (prototype Hg_2CuTi) or half Heusler (prototype MgAgAs) structure, or completely different ones. The AFLOWLib is steadily growing including additional structures, on which screening can continue. Furthermore, our method can be extended to additional AF configurations. Exemplarily, we investigated the AF3 state for some of the already investigated compounds. Here, the alternating planes are perpendicular to the [011] direction. This state is equivalent to the AF1 state by symmetry if only the Y or Z atom carries a magnetic moment. For the relevant compounds, where the MC ground state did not match our expectations, we investigated this configuration. The list of corresponding compounds can be found in Tab. 5.4. This includes mainly the Mn-based compounds. The table shows the energy difference $\Delta E_{\mathrm{AF3}} = E_{\mathrm{AF3}} - E_{\mathrm{FM}}$ and the calculated Néel temperature $\mathrm{T_N^{MC}}$, as well as the c/a ratio, where c is the lattice parameter in [001] direction. For Co_2TaTi, we were unable to reproduce the correct ground state in the SPR-KKR code. A large energy gain is found for Mn_2NiPd and Mn_2PdPt, which is attributed to the lattice

Table 5.5. | Comprehensive list of newly predicted AF Heusler compounds. Those found stable in experiments, but not investigated magnetically, are marked with an *.

Al_2MnOs	Mn_2NiPd	Pd_2HgMn	Ru_2HfMn
Au_2MnAg	Mn_2PdAu	Pt_2CrCu	Ru_2MnAl*
Co_2TaTi	Mn_2PdPt	Pt_2CuMn	Ru_2TiMn
Cu_2MnPt	Mn_2PdRh	Pt_2MnNi	Ru_2VSi*
Fe_2IrRh	Mn_2PtAu	Pt_2ScMn	Sc_2CoGa
Fe_2MnGe*	Mn_2PtCu	Rh_2CrAl	Ta_2FeMn
Fe_2NbGe	Mn_2PtRh	Rh_2CrIn	Ti_2VOs
Fe_2NbSn	Mn_2RuIr	Rh_2CuMn	Ti_2VRe
Fe_2TaSi	Nb_2FeMn	Rh_2MnGa*	Ti_2VRu
Fe_2TaSn	Os_2MnSi	Rh_2MnIn*	V_2FeOs
Fe_2VGe	Pd_2AuCr	Ru_2CrAl	V_2FeRe
Hf_2OsV	Pd_2AuMn	Ru_2CrGa	V_2FeRu
Hf_2ReV	Pd_2CrCu	Ru_2CrSb	Zr_2CoMn
Hg_2ScTi	Pd_2CuMn	Ru_2FeGa	Zr_2OsV

deformation found in the c/a ratio. This deformation may be indicative for shape memory behavior. The resulting Néel temperatures exceed 1 000 K. Also, only for these two compounds we find the expected ground state in the MC simulation. This investigation demonstrates that determining the correct AF ground state is a complex task and a future investigation of the AF3 state (and even further AF states) for all candidate materials is reasonable.

In conclusion we identified 70 antiferromagnetic Heusler compounds, out of the initial 80 000 ones in the AFLOWLib, which are expected to be stable or metastable in experiments. Comparison with available experimental data shows that our high-throughput approach has excellent selectivity. We identify 21 compounds to have a Néel temperature above room temperature, making them candidates for spintronic applications. A list of all compounds we predict as novel AF Heusler compounds, for which no magnetic or even no published data at all is found, is given in Tab. 5.5.

6

Antiferromagnetic Heusler Compound Ru_2MnGe

The Heusler compound Ru_2MnGe (RMG) is an AF material, predicted by our screening, which has been investigated both theoretically and experimentally. A theoretical investigation similar to our screening method was already done by Ishida *et al.* in 1995 [19] and yielded the same results. A detailed magnetic investigation in the bulk material using neutron diffraction was first reported by Gotoh *et al.* in the same year [21]. They found the predicted AF2 state as well as a Néel temperature of $T_\mathrm{N} = 295\,\mathrm{K}$.

About ten years later, the first experimental investigations on RMG thin films started. The results obtained by Kanomata *et al.* in 2006 confirmed the antiferromagnetism [22]. Extrapolating from the paramagnetic regime they reported a Néel temperature of $T_\mathrm{N} = 316\,\mathrm{K}$. A metal-insulator-metal transition was reported by doping the compound with Ti [162]. Ferromagnetism appeared when doping with V, although the two end compositions Ru_2MnGe and Ru_2VGe are AF [156]. In 2013, Ishida *et al.* investigated the exchange bias in nominal Fe_2CrSi / RMG bilayers [20, 163]. The Néel temperature determined by temperature dependent resistance measurements is $T_\mathrm{N} = 353\,\mathrm{K}$ for samples deposited on MgO substrates and $T_\mathrm{N} = 304\,\mathrm{K}$ on $MgAl_2O_4$ [163]. They prepared the samples by magnetron sputtering from stoichiometric targets and found a maximum exchange bias of

about 5 mT at liquid nitrogen temperature (77 K). Furthermore, they investigated the thickness dependence of the AF RMG and observed a critical thickness of about 8 nm, below which no exchange bias was found [20].

The RMG compound is a promising candidate for exchange bias systems. As previously described, the effect was already reported in RMG / F bilayers, however, only at liquid nitrogen temperatures. Its high Néel temperature above room temperature makes a further investigation interesting. In the following sections we will discuss the temperature dependence of the exchange bias as well as the integration of RMG in spintronic devices.

6.1. Preparation

We prepared RMG thin films using magnetron co-sputtering from elemental targets (cf. Sec. 4.1). These films were prepared in the 8×3" source apparatus. To obtain epitaxial growth we deposited RMG on a heated MgO (001) substrate. With a lattice parameter of $a_{\mathrm{MgO}} = 4.21\,\text{Å}$, the mismatch to the bulk lattice parameter of RMG $a_{\mathrm{RMG}} = 5.985\,\text{Å}$ [21] is about 0.5% considering the epitaxial relation RMG [100] ∥ MgO [110] ($a_{\mathrm{MgO}} \cdot \sqrt{2} = 5.957\,\text{Å}$).

The composition of the samples was determined and adjusted in advance using X-ray fluorescence (cf. 4.2.1). These results are typically accurate within 1% atomic content. We checked the epitaxial growth of RMG on heated MgO substrates for different substrate temperatures T_{S}. During the deposition, we used an Ar pressure of $2.3 \cdot 10^{-3}$ mbar. After the deposition the samples were cooled down to ambient temperature, then a protective capping layer to prevent oxidation was added. For these samples, this is a 2 nm MgO layer deposited by electron-beam evaporation at a rate of approximately $0.1\,\text{Å/s}$. Deposition rates for all sputtered layers were obtained using X-ray reflectivity analysis (cf. Sec. 4.3.2) which yields the layer thickness. Combined with the deposition time, the deposition rates were calculated.

In Fig. 6.1 measurements obtained by X-ray diffraction (cf. Sec. 4.3.1) for the three different substrate temperatures $T_{\mathrm{S}} = 300°\text{C}$, 400°C, 500°C are shown. For 300°C, no crystallization is observed. For 400°C and 500°C we observe the expected (002) and (004) peaks of the cubic RMG Heusler structure. Especially, for 500°C both (002) and (004) peaks show pronounced Laue oscillations, which

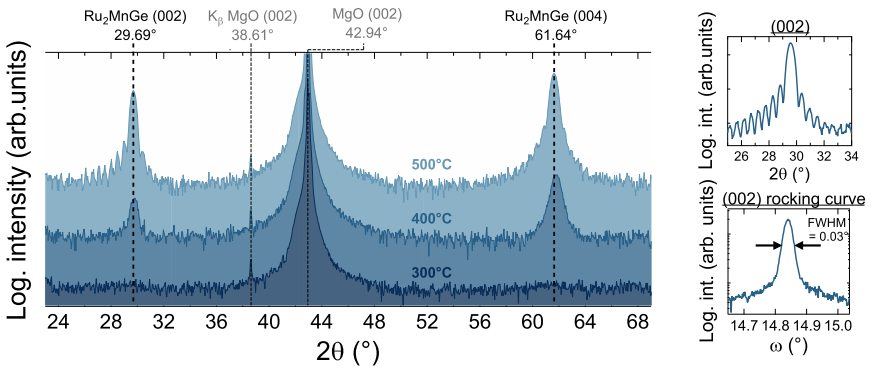

Figure 6.1. | XRD patterns of 20 nm thick RMG layers epitaxially grown at different substrate temperatures (left). The small graphs (right) show high-resolution measurements of the (002) peak and its rocking curve for a 500°C sample.

is indicative of a very homogeneous and coherent crystal growth. This is supported by the narrow rocking curves with full widths at half maximum (FWHM) of less than 0.03°, limited by the divergence of the diffractometer optics. The calculated lattice parameter deduced from the (002) and (004) peak positions is $c_{\mathrm{epit}} = 6.018\,\text{Å}$. It is slightly larger than the bulk value due to the lattice mismatch at the MgO / RMG interface. Due to these high quality results and previous experiments, which indicate Mn evaporation for temperatures above 550°C, we chose 500°C as the final deposition temperature. Further investigated deposition rates for RMG ranging from 1 Å/s to 3 Å/s revealed no changes in crystallographic properties.

The deposition system is further equipped with a *rapid thermal annealing* (RTA) system. This technique allows to rapidly heat a sample's surface with large temperature ramps of several 10 K/s, which may reduce the sample preparation time greatly. Here, the sample is heated by halogen lamps with a maximum power of 1 000 W. The RTA system is equipped in the load lock of the deposition system, so RTA treatment can be done without a vacuum break in the whole fabrication process. We checked the applicability of RTA to the RMG system by depositing RMG on amorphous thermally oxidized silicon substrates at room temperature.

Generally, all samples were treated by RTA before adding additional layers, which is done after the sample was cooled down. However, our first investigation

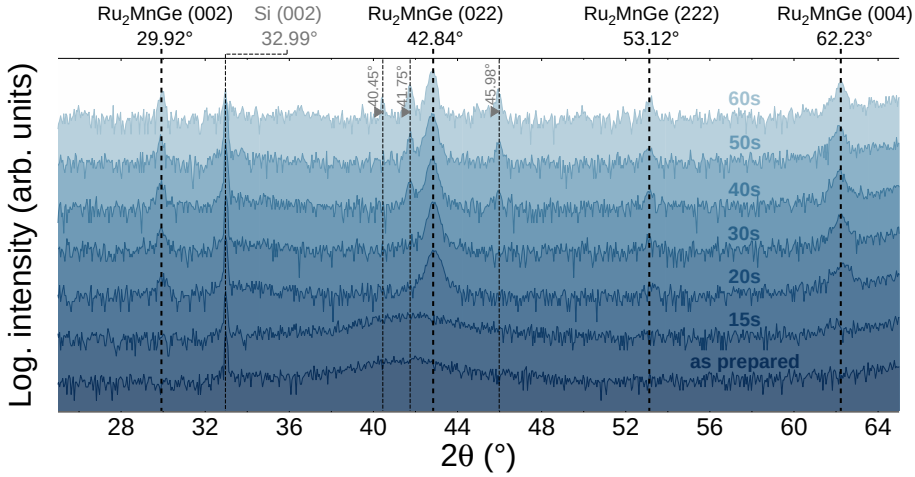

Figure 6.2. | XRD patterns of 20 nm thick polycrystalline RMG layers grown on amorphous Si/SiO_2 substrates treated with 1 000 W RTA for different durations printed in the graph.

is an exception: A 2 nm MgO capping layer deposited using electron-beam evaporation is added and the sample cut into pieces (including a vacuum break) prior to RTA treatment. This allowed the effect of RTA to be investigated by means of XRD, as shown in Fig. 6.2. Here, the patterns for annealing with 1 000 W for different durations are plotted. After 20 s annealing, crystallization can be observed. Here, the sample reaches approximately 400°C. For 30 s ($\sim$ 550 °C) we obtain optimal results, where for 40 s ($\sim$ 650°C) secondary phases crystallize indicated by additional peaks in the XRD pattern. This happens most likely due to the Mn evaporating from the sample. Therefore, further investigated samples are annealed for 30 s in general. We observe the (002), (022), (222) and (004) peaks, which are expected for polycrystalline crystal growth. Rocking curves and peak intensity analysis confirms the polycrystalline nature of the samples. The lattice parameter deduced from XRD peak positions is $a_{\mathrm{poly}} = 5.971\,\text{Å}$, which is in good agreement with the bulk lattice constant. In conclusion, using two different thermal treatments within the deposition process we are able to produce epitaxial as well as polycrystalline RMG thin films.

We investigated both types of samples regarding their magnetic properties. Standard magnetization measurements at room temperature did not show any

ferromagnetic signals. X-ray magnetic circular dichroism (cf. 4.5.1) in total electron yield and luminescence of the substrate[1] showed no ferromagnetic signal for Mn down to 10 K in a field of 0.5 T, thus confirming the zero net magnetization. Hence, the Mn atoms are presumably coupled antiferromagnetically as expected.

6.2. Exchange Bias in Ru_2MnGe / Fe bilayers

To investigate the exchange bias effect in RMG based systems we prepared RMG / Fe bilayers. For both epitaxial and polycrystalline samples we deposited the Fe layer after cooling down the sample, either the heated substrate or from RTA. The samples are capped with a 2 nm MgO layer as before.

We use the AMR (cf. Sec. 2.2) to electrically measure the switching fields of the Fe layer. As outlined in 4.4.2, this is a viable method to investigate exchange bias and coercivity in thin films. We cut the samples into pieces of approximately 2 mm $\times$ 5 mm. The pieces are glued onto a chip carrier and contacted across the long side by conductive silver as sketched in Fig. 6.3a. To ensure reliable results using this contacting method, a contacting via bonding wires and resistance measurements in 4-point geometry was done in comparison. The results indicate no significant increase in signal-to-noise ratio, hence we decided to contact the samples with conductive silver for the sake of reduced preparation effort.

Measurements were done in a closed-cycle He cryostat providing temperatures in the range of 1.7 - 300 K with magnetic fields up to 4 T in one direction and 0.5 T in perpendicular direction. The resistance was measured using a KEITHLEY 2000 multimeter. To verify the measurement of the AMR we measured an MgO / RMG 10 nm / Fe 2 nm / MgO 2 nm sample at 200 K sweeping the magnetic field in the sample plane for both parallel and perpendicular orientation to the current. The resulting $R(H)$ measurements are plotted in Fig. 6.3b. Here, the absolute resistance as well as the magnetoresistance MR (as defined in Eq. (4.5)) are plotted. The MR is normalized to $R_0 = R(M = 0)$, i.e., the resistance at the switching fields. In blue, a field sweep in parallel orientation is plotted, whereas in orange in perpendicular orientation. The curves are perfectly symmetric regarding the resistance changes. The signal matches the expectation for the AMR.

[1] XMCD measurements were performed at beamline 4.0.2 of the Advanced Light Source in Berkeley, CA, U.S.

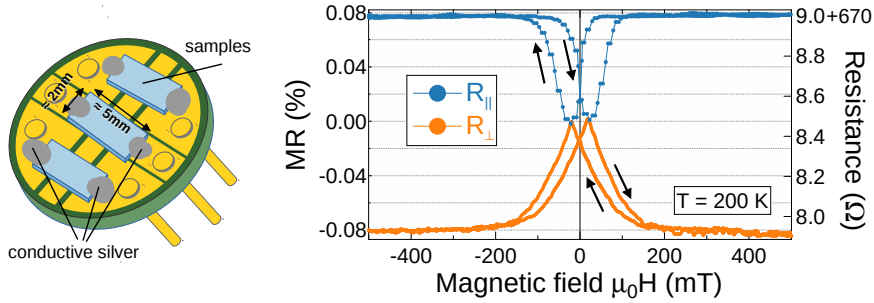

(a) **(b)**

Figure 6.3. | AMR measured in RMG / Fe bilayers. **(a)** Sketch of samples on a chip carrier as used in the experiment. **(b)** AMR of an epitaxial RMG / Fe bilayer measured at 200 K for field sweeps parallel (blue) and perpendicular (orange) to the current. Arrows indicate the sweep direction.

The differences in shape and point density are attributed to the two different superconducting magnets, as the 4 T magnet has a significant lower resolution. The signal amplitude at 200 K is about 0.08% as shown and increases to 0.2% on average at 3 K.

As demonstrated in these measurements we are able to deduce the magnetic switching of the Fe layer from AMR measurements. To exclude possible contributions from the RMG layer we measured the AMR of a single RMG layer without Fe. No measurable AMR signal was found in this case, which is consistent with previous investigations by Mizusaki *et al.* [164]. We obtain the same results for measurements on polycrystalline samples grown on Si / SiO_2 substrates. Therefore, we use the AMR technique in general to investigate the exchange bias in RMG / Fe bilayers.

We measured all samples after FC in a magnetic field of 0.5 T perpendicular to the current direction. If temperature dependent measurements were performed, these were recorded after FC starting at low temperature and increasing. In all cases, the Fe thickness is $t_{\mathrm{Fe}} = 2\,\mathrm{nm}$. In a first experiment we investigated the exchange bias effect size dependence on the RMG thickness t_{RMG}. This was already done by Fukatani *et al.* and revealed a critical thickness of $t_{\mathrm{RMG}} = 8\,\mathrm{nm}$. This result is reproduced by our experiments. In order to achieve the maximum ex-

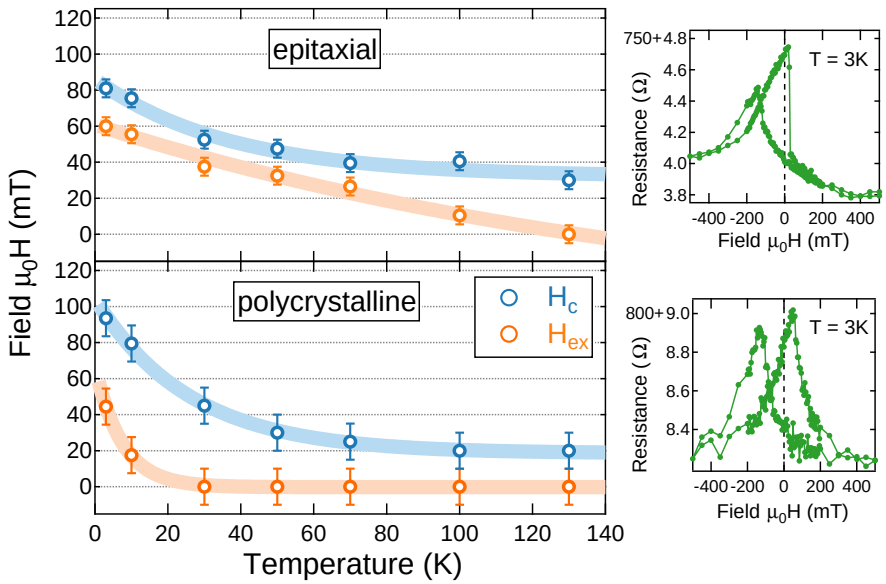

Figure 6.4. | Exchange bias and coercivity in RMG / Fe bilayers. Results obtained from epitaxial (polycrystalline) samples are shown in the top (bottom) part. The left graph shows the temperature dependence of the coercivity H_c (blue) and the exchange bias field H_{ex} (orange). Solid lines are guide to the eye. Error bars for epitaxial samples are smaller due to a sharper switching in the AMR signal, exemplarily shown for both cases in the right graphs.

change bias we prepared samples of $t_{RMG} = 10, 20, 30$ nm. The largest exchange bias was found for $t_{RMG} = 10$ nm. Our measurements for $t_{RMG} = 20, 30$ nm show no further increase in exchange bias, therefore all further investigations are done with $t_{RMG} = 10$ nm. We find a sizable exchange bias of $H_{ex} = 68$ mT for epitaxial films and $H_{ex} = 54$ mT for polycrystalline films[2] after cooling down the samples to 3 K. These values, however, are the initial values obtained in the first field loop. To estimate a training effect, i.e. a decrease of H_c and H_{ex} with the number of field cycles, ten loops were recorded in a row. We observe a small training effect in both sample types. For epitaxial films, the effect is about 12% and for polycrystalline films about 20%. After 3-5 loops, no further significant

[2]This and all further mentioned field values given in mT implicitly include the μ_0 factor.

drop is visible. The temperature dependence of the coercivity and the exchange bias was investigated by heating up the samples to the desired temperature after training. Both H_c (blue) and H_{ex} (orange) are plotted in Fig. 6.4 for the epitaxial and polycrystalline samples as well as an exemplary $R(H)$ measurement for both types in the right graphs plotted in green. The error bars for epitaxial samples are smaller due to a sharper switching in the AMR signal. We find a substantially different temperature dependence of the exchange bias between epitaxial and polycrystalline samples. It decreases linearly for the epitaxial RMG before going down to zero at around 130 K. In case of polycrystalline RMG the exchange bias rapidly decreases with increasing temperature and vanishes at around 30 K. The coercivity decreases in both cases and stabilizes at around 70 K. The maximum values we obtained at a temperature of 3 K are summarized in Tab. 6.1. Here, also the interfacial energies $J = t_{Fe} M_{Fe} H_{ex}$ are given. They are $J = 0.210\,\mathrm{erg/cm^2}$ (epitaxial) and $J = 0.156\,\mathrm{erg/cm^2}$ (polycrystalline), respectively, with the saturation magnetization of iron $M_{Fe} = 1748\,\mathrm{emu/cm^3}$ [165]. These values are of the same order as for common exchange bias systems at room temperature, for example, 0.18 erg/cm^2 for PtMn / CoFe and IrMn / CoFe [13]. The given blocking temperature is an upper limit deduced from our measurements. The different temperature stability is attributed to the different exchange bias mechanism dominating in epitaxial and polycrystalline thin films. Whereas in epitaxial films mainly domain wall pinning in the AF stabilizes the exchange bias, for polycrystalline the granular structure and thermal activation energy of the crystal grains determine the effect size (see Sec. 2.1).

Table 6.1. | Coercivity H_c, exchange bias H_{ex}, interfacial energy J and blocking temperature T_B values for RMG / Fe bilayers measured at 3 K. Given values are measured after training. The initial, maximum values measured prior to training in the first field loop are given in brackets.

Parameter	Epitaxial	Polycrystalline
H_c (mT)	81.0 (93.0)	93.5 (109.0)
H_{ex} (mT)	60.0 (68.0)	44.5 (54.0)
J (erg/cm^2)	0.210 (0.238)	0.156 (0.189)
T_B (K)	130	30

6.3. Improving Effect Size

To improve the effect size and temperature stability we followed two approaches. The *interface dusting* allows us to control the termination of RMG at the interface, which affects the exchange bias effect size. By doping RMG we tried to stabilize the exchange bias by domain wall pinning, as proposed by Nowak *et al.* [44, 45].

6.3.1. Interface Dusting

Due to the complex magnetic AF2 structure within the fcc-Heusler structure and the magnetic moment isolated on the Mn atoms, the interface termination of RMG to Fe plays an important role. The RMG grows in [001] direction, hence a termination with Ru atoms at the RMG / Fe interface is possible, which is not beneficial for the coupling between the magnetic Mn atoms and Fe. In order to control the interface termination of RMG we added a thin intermediate layer of Mn after depositing and cooling down the initial RMG layer. This interface dusting was already investigated by Carpenter *et al.* in polycrystalline IrMn / CoFe bilayers [166]. They found a significant increase of the exchange bias. The temperature stability, however, was not affected. This is not unexpected, as the underlying crystal structure of the AF is hardly affected by the dusting.

We prepared samples with an intermediate layer of 1.0, 1.5 and 2.0 monolayers (MLs) of Mn. The interlayer thickness was estimated using the Mn atom radius and the Mn deposition rate. Polycrystalline RMG samples show a significant increase in exchange bias of up to 40% for 2 ML of Mn as plotted in Fig. 6.5a. For thicker interlayers the effect is expected to reduce again as shown by Carpenter *et al.*, therefore the maximum interlayer thickness investigated in this work is 2 ML. For epitaxial samples we did not find an increase in effect size within the error bars.

To investigate the different observations for polycrystalline and epitaxial samples we performed X-ray absorption[3] studies on selected samples (cf. Sec. 4.5). As shown in Fig. 6.5b, in contrast to the epitaxial films we find multiplet structures (marked by arrows) for polycrystalline films in the XA spectrum, which are indicative of oxidation. The shown spectra were recorded in TEY mode, sensitive

[3] XAS measurements are performed at beamline 4.0.2 of the Advanced Light Source in Berkeley, CA, U.S.

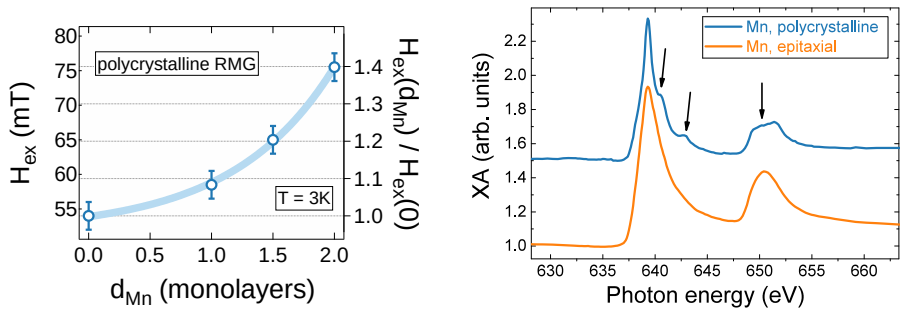

Figure 6.5. | Effect of Mn interface dusting. **(a)** Exchange bias field H_{ex} depending on the Mn interlayer thickness d_{Mn} for polycrystalline RMG / Fe bilayers. The solid line is a guide to the eye. **(b)** Mn XA spectra of the L_2 and L_3 edges for epitaxial (blue) and polycrystalline (orange) RMG / Fe bilayers recorded in TEY mode. The arrows indicate peak shifts most likely due to oxidation, which are not visible in the LM mode.

only to the Mn atoms close to the sample surface. As the multiplet structures are not visible in LM mode, sensitive to the bulk, we conclude an oxidation effect at the RMG / Fe interface. However, a depth analysis using ion etching and Auger electron spectroscopy [167] did not show any significant oxygen concentration at the RMG / Fe interface. The polycrystalline RMG layer was treated by RTA before adding additional layers, so the films were exposed to an increased oxygen concentration, as the pressure rises due to the RTA heating of the chamber. This may have led to an oxygen deposition at the interface. The addition of a few monolayers Mn at the interface possibly compensated the oxygen or may even have formed antiferromagnetic MnO leading to the significant increase of the exchange bias field.

Furthermore, the different crystallization processes may result in different grain sizes and boundaries. The growth process on heated substrates forms very homogeneous crystallites with low angular mismatches at their boundaries. In contrast, the polycrystalline structures form at random orientations supporting large angular mismatches between crystallites. This leads to potentially larger voids in the films allowing oxygen to migrate deeper into the film, which is another explanation for the measured oxidation effects. These facts influence the

thermal stability as well as produce a measurable XA signal, but no general significant oxygen concentration in the films.

6.3.2. Doping

The domain state model proposes to enhance the exchange bias when the AF is diluted leading to domain wall pinning. We investigated this by doping the RMG layer with Ta. Other materials were less favorable due to too large specific deposition rates, increasing the lower doping concentration limit. We prepared RMG / Fe bilayers with low Ta doping concentrations in the RMG of approximately 1%, 2%, and 3% by co-sputtering. Unfortunately, we find no improvement in effect sizes for both epitaxial and polycrystalline samples. Moreover, the exchange bias drops for about 10-20% in both cases when doping with 3% Ta.

This investigation, however, is to be extended. As demonstrated by Fecioru-Morariu *et al.* in an investigation of Cu doped IrMn [168], dilution up to 20% Cu can improve the exchange bias effect. Smaller concentrations also slightly improved the temperature stability. Obstacles like the large specific deposition rates for dopant materials can be overcome, e.g., by using composite targets. Here, the elemental constituents including the dopant are merged in the correct composition into a single sputtering target. The overall composition then can be adjusted by co-sputtering with the elemental targets.

6.4. Integration of Ru_2MnGe into Spintronic Devices

Previous investigations aim to integrate RMG into spintronic devices to use it in applications. Despite the shortcomings regarding temperature stability, we investigate this in the following. Therefore, we prepared TMR multilayers using an MgO tunneling barrier. Before depositing the TMR stack, we left the deposited RMG layer at 500°C for one hour (in-situ post annealing). This further increases the crystalline quality. As previously done, we deposited the TMR stack in the form of F / MgO / F on top of the RMG layer after cooling down the sample. If not otherwise stated, the full multilayer sequence is MgO / RMG 12 / F 2 / MgO 2 / F 2 / Ta 3 / Ru 5. All layer thicknesses are given in nm. The RMG layer thickness is

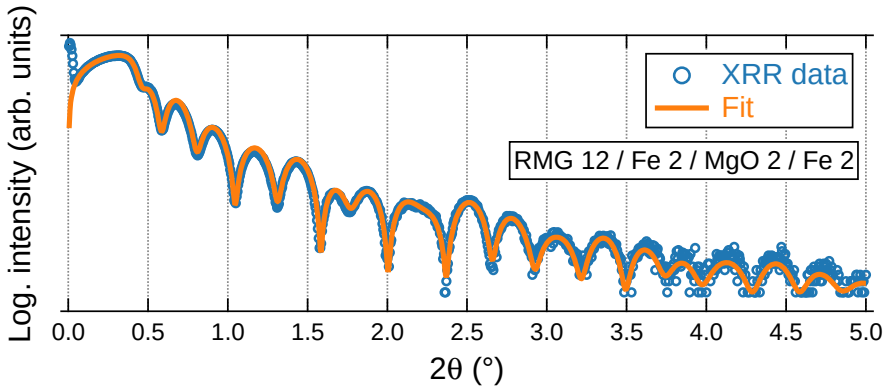

Figure 6.6. | XRR measurement of a TMR stack (thicknesses in nm). Blue dots are measured data points and the solid orange line is a fit.

Table 6.2. | Final XRR fit parameters obtained for a RMG / Fe / MgO / Fe TMR stack. The layer thickness t, the interface roughness R and the density ρ are given.

Layer	t (Å)	R (Å)	ρ (g/cm^3)
Substrate	–	2.36	3.58
RMG	115.1	2.77	10.11
Fe	20.5	3.31	7.67
MgO	24.2	2.27	3.58
Fe	21.6	6.03	7.50

slightly increased to ensure a maximal exchange bias. Within our investigation, we used Fe and $Co_{70}Fe_{30}$ (in the following simply denoted as CoFe) as the F for both electrodes. The MgO barrier was deposited using electron-beam evaporation at a deposition rate of approximately 0.1 Å/s. As an electrical top contact, a Ta / Ru layer is added. The RMG layer is used as an electrical bottom contact in all cases.

In a first investigation we examined the structural properties of a full TMR stack. Previous investigations already demonstrated that the crystal growth of the RMG layer is of high quality. Especially a low roughness is important to

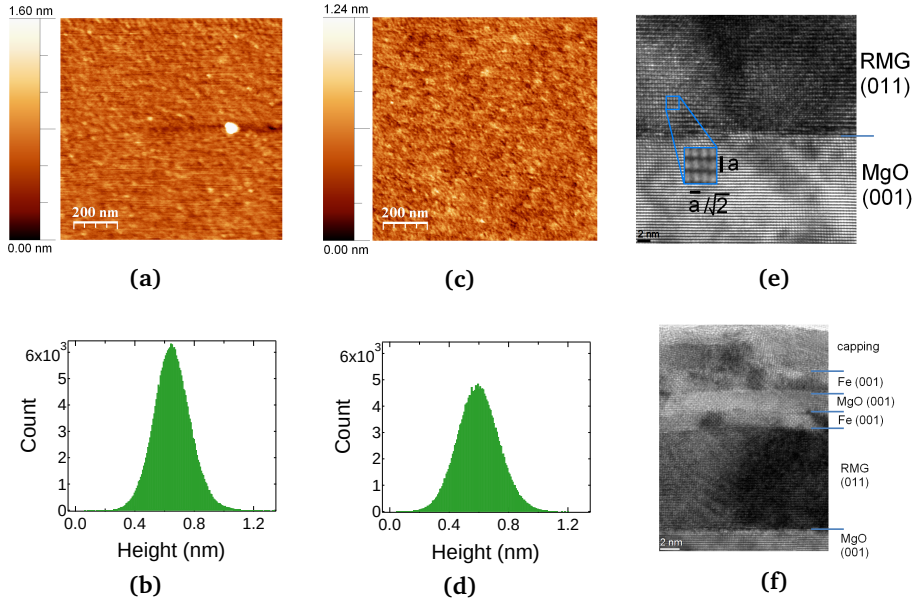

Figure 6.7. | AFM and HR-TEM measurements of TMR tacks. **(a)** and **(b)** AFM image of an Fe-based TMR stack's surface and the corresponding height distribution across the AFM image. **(c)** and **(d)** The same analysis for a CoFe-based TMR stack. **(e)** HR-TEM image of the MgO substrate / RMG interface. **(f)** HR-TEM image of the full TMR stack showing a clean tunneling barrier.

obtain a clean tunneling barrier without pinholes. An XRR measurement of a RMG / Fe / MgO / Fe multilayer is given in Fig. 6.6. The blue dots are measured data points and the orange line is a fit using the Parratt algorithm as discussed in Sec. 4.3.2. The fit matches the measured data precisely, even up to large angles of $2\theta = 5°$. The layer thicknesses t as well as the interface roughness R and the mass density ρ as obtained by the fit are summarized in Tab. 6.2. The results indicate a very low roughness of 2-3 Å for the TMR stack. For the upper Fe layer, a slightly increased thickness and lower density is found, which is attributed to the increased roughness of 6 Å.

In addition to this, we investigated the surface of our TMR stacks using AFM (cf. Sec. 4.3.3). Recorded data is shown in Fig. 6.7. In Fig. 6.7a, the surface of a Fe-based TMR stack is shown, with the corresponding height distribution plotted in Fig. 6.7b. For the CoFe-based one the corresponding data is shown in Fig. 6.7c

and Fig. 6.7d, respectively. Both measurements show a smooth surface without cluster or island nucleation. The white dot in Fig. 6.7a is due to contamination and not attributed to the sample. This is excluded in all deduced values. The low roughness obtained from the XRR measurements is confirmed by these results. We find values of 1.3 Å for the Fe-based stack and 1.4 Å for the CoFe-based one.

In collaboration with the University of York the tunneling barrier was further investigated by high-resolution tunneling electron microscopy (HR-TEM)[4]. Cross section images are shown in Fig. 6.7e and Fig. 6.7f. In the first image the MgO / RMG interface is shown confirming the epitaxial growth. In the RMG layer the ordered Heusler structure is visible by the alternating planes of Ru and Mn-Ge. The magnified region shows the $1 : 1/\sqrt{2}$ relation of the unit cell dimensions as expected for the RMG [110] interface. No defects are observed in the bulk material. The second image shows all layers with an atomically smooth growth throughout the whole TMR stack. The barrier is of good crystallinity without any defects. The visible 11-12 atomic layers of MgO correspond to a barrier thickness of $23.2 - 25.3$ Å ($a_{\mathrm{MgO}} = 4.21$ Å) confirming the results obtained by XRR. The slight increase in roughness at the interface of the top Fe and the capping layer is confirmed as well.

For the final investigation of MTJ devices the samples were patterned in a standard UV lithography process (cf. Sec. 4.6) in combination with secondary ion mass spectroscopy controlled Ar ion beam etching. Square nano pillars of $7.5 \times 7.5\,\mu\mathrm{m}^2$ were prepared. The RMG layer is used as a bottom contact for all MTJ cells as shown in Fig. 6.8a. Here, a patterned MTJ nano pillar is illustrated with Ta 5 nm / Au 60 nm contact pads added in a second lithography step on top. The TMR structure at the bottom contact is negligible as its area of $\mathcal{O}(10\,\mathrm{mm}^2)$ is large compared to the MTJ. Samples are mounted on a chip carrier for electrical measurements and contacted by Au bonding wire using ball and wedge bonding. Measuring the I-V characteristic curve at room temperature reveals a working tunneling barrier. Applying a Brinkman fit [169] to the numerical derivative dI/dV allows determination of the tunneling barrier height φ, asymmetry $\Delta\varphi$ and thickness d. Fig. 6.8b shows the actual measurement (thin, blue line) and the fit (thick, orange line). The effective electron mass m_{eff} is a free parameter in

[4] HR-TEM investigations were done by Teodor Huminiuc, Department of Physics, University of York, York YO10 5DD, England

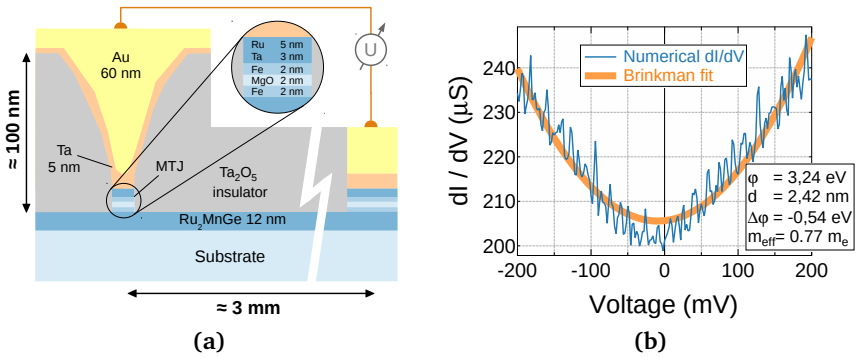

Figure 6.8. | Structured MTJ nano pillar. **(a)** Schematic cross section of an exemplary MTJ nano pillar after lithography. The TMR structure of the bottom contact (right) is negligible due to its large area of $\mathcal{O}(10\,\mathrm{mm}^2)$. **(b)** Numerical derivative of the MTJ's I-V characteristic curve (blue) and a Brinkman fit (orange). Final fit parameters for fixed d are given in the box.

this model. As we know the barrier thickness d exactly from XRR and HR-TEM, we adjust m_{eff} to obtain the correct value for d. The final fit parameters given in Fig. 6.8b are reasonable considering the MgO band gap of 7.8 eV [170].

Further magnetic characterization was done similarly as for the exchange bias investigation. The samples are cooled down in the closed-cycle He cryostat in a magnetic field of 4 T. After cooling down the TMR (see Eq. (2.2)) is measured with a constant applied voltage of $U = 10\,\mathrm{mV}$ across the MTJ and sweeping the magnetic field in the sample plane while recording the resulting tunneling current. The corresponding loops are shown in Fig. 6.9. In Fig. 6.9a the major loop is plotted. A clear asymmetry is found in the loop caused by the exchange bias. The switching fields in the positive field range are equal within the measured resolution, thus, no distinct switching is observed. This measurement demonstrates that we successfully integrated RMG into an MTJ acting as a pinning layer for the lower Fe electrode. To confirm the functionality of the MTJ we recorded a minor loop plotted in Fig. 6.9b. We measure a clean, square switching of the resistance with an amplitude of about 100% TMR. It is noteworthy that these results are obtained from samples *as prepared* without the necessity of further treatment such as post annealing.

However, in typical CMOS fabrication procedures elevated temperatures occur. Therefore, we systematically investigated the TMR amplitude as a function of dif-

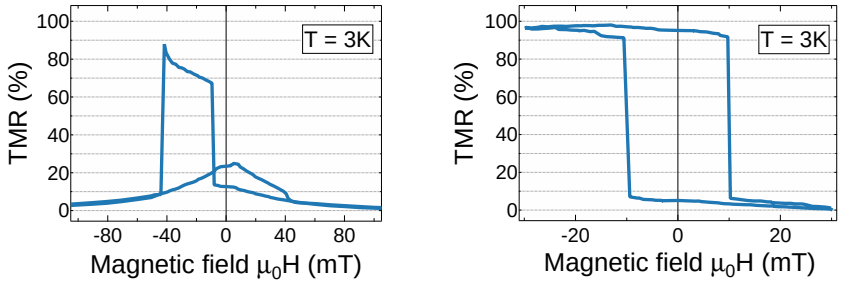

Figure 6.9. | Characterization of a RMG / Fe / MgO / Fe TMR stack. **(a)** Major loop recorded at $T = 3\,\mathrm{K}$ with a bias voltage of $U = 10\,\mathrm{mV}$. The exchange bias causes an asymmetry in the loop. **(c)** Minor loop recorded at the same conditions.

ferent post annealing temperatures. We prepared TMR stacks with an increased layer thickness of 3 nm for the upper, unpinned electrode to induce an intrinsic asymmetry in the switching fields. This allows to measure a comparable TMR value at room temperature. Comparison of low temperature measurements reveal that the TMR amplitude is not affected by this. We annealed equivalent samples prior to lithography for one hour at temperatures ranging from $T_{\mathrm{pa}} = 250°\mathrm{C}$ to 400°C in steps of 50°C, which are typical post-processing temperatures. We measured the TMR in about 20 MTJ cells for each sample. The average values are plotted in blue in Fig. 6.10. The error bars indicate the standard deviations. We find a maximum in the TMR amplitude for $T_{\mathrm{pa}} = 250°\mathrm{C}$, however, in conjunction with a significantly increased scattering indicated by the error bars. For 300°C, the amplitude is comparable to the as-prepared state. For higher annealing temperatures, the TMR amplitude decreases further.

As already indicated in Fig. 6.10 we also exemplarily investigated TMR stacks using CoFe as the electrode material. The resulting TMR amplitudes are shown in orange. The as-prepared sample is comparable to the Fe-based one with a slightly increased scattering. The sample annealed at the optimum temperature $T_{\mathrm{pa}} = 250°\mathrm{C}$, however, shows the least scattering of all samples. The TMR amplitude remains approximately the same.

In a next step, we measured the TMR at low temperatures for samples in the as-prepared state without post annealing as well as annealed samples at the op-

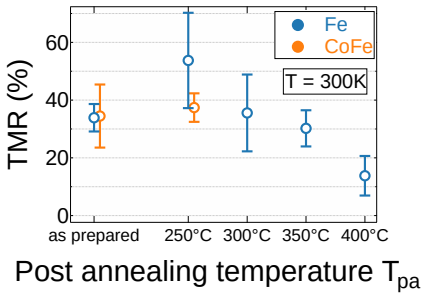

Figure 6.10 | TMR in multilayers with Fe (blue) and CoFe (orange) electrodes after post annealing for one hour at different temperatures. The unpinned F layer has an increased thickness of 3 nm. The values are averaged over about 20 MTJs, error bars reflect the corresponding standard deviations.

timum temperature $T_{\mathrm{pa}} = 250°\mathrm{C}$. The results are plotted in Fig. 6.11. Again, the results for Fe-based MTJs are plotted in blue (upper) and for CoFe in orange (lower), respectively. In the first graph, major loops are plotted. Due to the increased thickness of the unpinned F layer, its switching field in the positive field branch is shifted, so the distinct switching is now also resolved in this part. A slightly reduced exchange bias for the CoFe MTJ is evident. The TMR amplitude, as shown in the minor loop in the middle graph, is comparable at around 100%. Minor loops recorded for the annealed samples shown in the right graphs, however, reveal a significant difference: The Fe-based MTJ shows an increased TMR amplitude to 135% but also multidomain switching. This observation agrees with the previously found large scattering in the measured TMR amplitudes. In contrast, the minor loop of the CoFe-based MTJ did not change in shape at all. In addition, the TMR amplitude is not affected. We therefore conclude that the Fe crystal structure is crucially affected by the post annealing treatment, which is not the case for the CoFe based MTJs. As the TMR amplitude is comparable, CoFe is identified as a preferable material for RMG based TMR devices.

Because of the exchange bias we found in polycrystalline RMG / Fe bilayers as well, we also prepared MTJs using polycrystalline RMG as a pinning layer. Unfortunately, for these samples we did not observe any sizeable TMR. This is most likely due to rough tunneling barriers supporting the inclusion of pinholes mediated by the growth process and the polycrystalline RMG layer itself. Growth optimization to reduce the roughness is necessary in this case. Due to the working epitaxially grown MTJ devices and their ease of fabrication, we focused our work on those devices.

To summarize, we have demonstrated that the antiferromagnetic Heusler compound Ru_2MnGe induces sizeable exchange bias effects both in epitaxial and

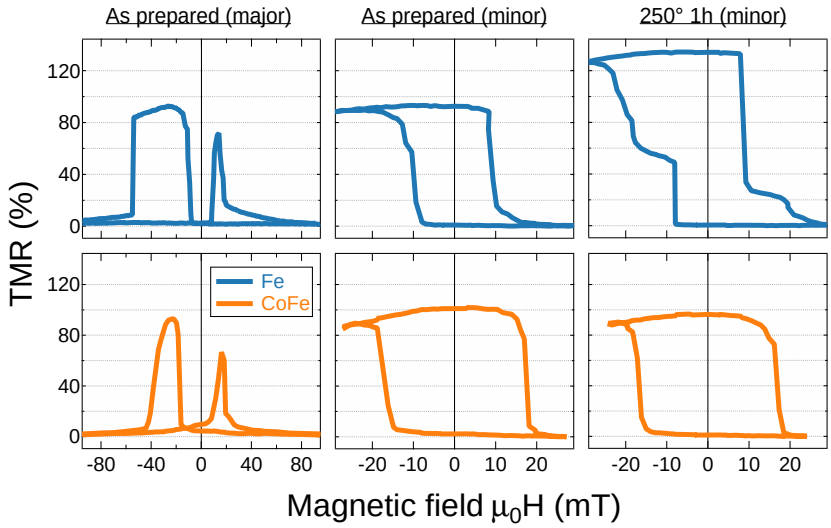

Figure 6.11. | TMR in post-annealed Fe- (blue, top) and CoFe-based (orange, bottom) multilayers. The left graphs show the major loop of samples without post-annealing. In the middle graphs the corresponding minor loops are plotted. The right graphs show the minor loop for samples annealed for one hour at 250°C.

polycrystalline form when in contact with ferromagnetic layers such as Fe and CoFe. The only shortcoming is a blocking temperature below room temperature. Using different microscopy techniques we showed that epitaxial growth of excellent quality throughout whole TMR stacks is easily achievable without the necessity of ex-situ treatment. To the best of our knowledge, our work is the first reported demonstration of a working exchange biased MTJ using an antiferromagnetic Heusler compound as a pinning layer. The TMR reaches values of around 100% at low temperatures, which is comparable to similar Fe-based TMR systems [171]. Furthermore, where Fe-based systems exhibit an increased TMR but with multidomain switching after post-annealing, CoFe-based ones are merely affected at all.

7

Perpendicular Ferrimagnet Mn_3Ge

The ferrimagnetic material Mn_3Ge, whose structure is quite related to the Heusler structure, is an interesting compound in several ways. In the recent years, it caught attention due to some promising properties for spintronic applications. In the following chapter we will discuss these as well as an approach to tune its magnetic properties: Using DFT we identify promising dopant elements, which we check experimentally for two cases.

The face centered tetragonal (fct) $D0_{22}$ (spacegroup $I4/mmm$, No. 139) ϵ_1-phase is found within the Mn-Ge phase diagram [172] in a narrow range of 76.5% - 78% atomic Mn content ($Mn_{3.4}Ge$). Considering the $L2_1$ Heusler structure with Mn occupying X and Y positions, and Ge the Z position, the $D0_{22}$ structure can be interpreted as a tetragonally distorted $L2_1$ structure. The stoichiometric Mn_3Ge crystal structure is depicted in Fig. 7.1. Here, Ge occupies the Wyckoff position $2a$ (● = Ge), whereas Mn occupies the two sublattices at positions $2b$ (● = Mn_I) and $4d$ (● = Mn_{II}). The two Mn sublattices are coupled antiferromagnetically due to their interatomic distances [24]. This results in an overall ferrimagnetic configuration with a magnetic easy axis in crystallographic c-direction.

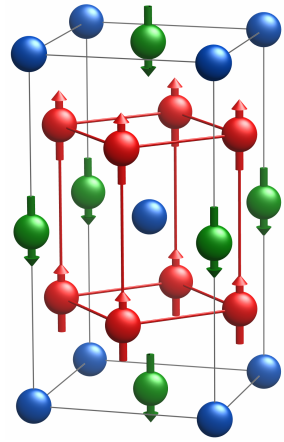

Figure 7.1 | $D0_{22}$ crystal structure of the ferrimagnetic Mn_3Ge compound. Wyckoff position $2a$ is occupied by Ge = ● , whereas Mn occupies positions $2b$ Mn_I = ● and $4d$ Mn_{II} = ●. Arrows indicate the ferrimagnetic configuration. Sketch created with VESTA [140].

The crystal structure was investigated in the 1970s by Kádár and Krén using neutron diffraction on bulk $Mn_{3.4}Ge$, where the $D0_{22}$ structure was found [173]. The lattice parameters of the tetragonal cell are $a = 3.816\,\text{Å}$ and $c = 7.261\,\text{Å}$. Furthermore, they estimated the magnetic moments located on the different Mn atoms to be $\mu_{\text{Mn}_\text{I}} = (-3.4 \pm 0.3)\,\mu_\text{B}$ and $\mu_{\text{Mn}_\text{II}} = (1.9 \pm 0.2)\,\mu_\text{B}$ resulting in a low net magnetization of about $0.4\,\mu_\text{B}$/f.u.. The structure was found to undergo a phase transition to the high temperature $D0_{19}$ ϵ-phase at 850 K. The Curie temperature is even higher and extrapolated to be 920 K.

In the recent years, several publications on epitaxially grown $Mn_{3+x}Ge$ in thin film form appeared. Kurt *et al.* reported on stoichiometric Mn_3Ge grown on $SrTiO_3$ (STO) substrates [24]. The lattice mismatch is as low as 2.4% ($a_\text{STO} = 3.91\,\text{Å}$). They found a large coercivity of 2.3 T in out-of-plane direction and a small, softmagnetic contribution in in-plane direction. By estimating the anisotropy field H_k from in-plane measurements they calculated a large anisotropy constant of $K_u = \mu_0 H_k M_\text{S}/2 = 0.91\,\text{MJm}^{-3}$. Using point contact Andreev reflection they measured the spin polarization to be 46%. Similar results were reported by Mizukami *et al.* [25]. They prepared $Mn_{3+x}Ge$ on MgO substrates and found the largest anisotropy for $x = 0.55$, which is of the same order as found by Kurt *et al.*. In a second publication, they reported on Cr buffered Mn_3Ge on MgO, where a high squareness in the hysteresis is found [174]. The high anisotropy is confirmed here as well. All reported magnetic measurements agree with the values obtained by neutron diffraction within the error margins.

Mizukami *et al.* furthermore reported on band structure investigations for stoichiometric Mn_3Ge [25]. They predict a fully spin-polarized Δ_1 band in c-direction, which, in conjunction with an MgO tunneling barrier, can lead to large TMR values due to orbital symmetry filtering [175]. This, of course, is highly recommended for electrode materials, e.g., in MTJ spin valves. Additionally, the low saturation magnetization and large out-of-plane anisotropy (both reducing the required critical switching current for spin transfer torque switching [56]) makes this rare-earth and noble metal free material a promising candidate for applications such as STT-MRAM. Furthermore, due to its large coercivity it is interesting as an alternative material for our main task, the replacement of common AFs mediating an exchange bias to create a magnetic reference. It can either act as an electrode material itself strongly resistant against external magnetic fields up to several Tesla, or in a "pseudo exchange bias" configuration, where the electrode material is coupled to the Mn_3Ge film and effectively pinned due to its large coercivity. Furthermore, by tuning the magnetic properties, a compensation of the ferrimagnet at room temperature may be achieved, a state hardly sensitive to external magnetic fields similar to AFs.

As already indicated, the stoichiometric $D0_{22}$ Mn_3Ge is metastable; the natural bulk composition is $Mn_{3.4}Ge$. By forced epitaxy on MgO or STO substrates this phase can be stabilized, however, this supports the formation of secondary impurity phases, which are found in any recent investigation [24, 25, 174]. Along with this comes a quite high roughness limiting the applicability in TMR spin valves. This can be reduced by increasing the Mn content or in a three-step self-seeding deposition process [176, 177]. However, the compound's magnetic properties are quite sensitive to the Mn:Ge ratio as well [178]. The epitaxial growth of $Mn_{3+x}Ge$ recently has been investigated in the two theses by M. Glas [178] and H. Dohmeier [177] confirming the structural and magnetic properties discussed above. Hence, we adopt the optimal growth parameters and focus on tuning of the magnetic properties in stoichiometric Mn_3Ge.

7.1. Investigation of Doping using DFT

The magnetic properties of Mn_3Ge are quite sensitive to the atomic Mn content and crystallographic order. Thus, it is suggestive to investigate the effect of

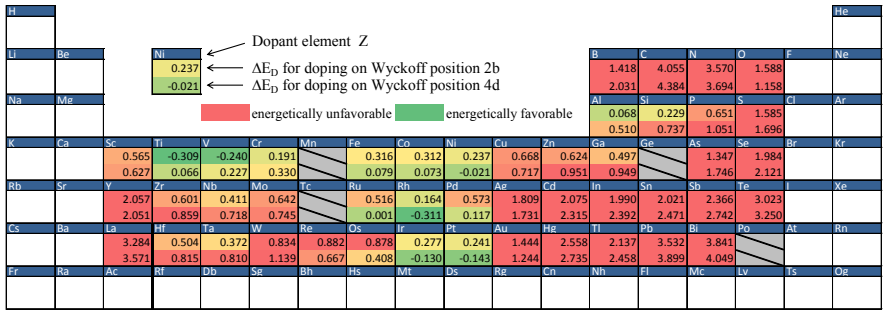

Figure 7.2. | Defect formation energies ΔE_D in eV of doped Mn_3Ge. For each dopant Z ΔE_D is given for doping Wyckoff position $2b$ (upper) and $4d$ (lower). The color encodes the energy gain ($\Delta E_\mathrm{D} < 0$ in red, $\Delta E_\mathrm{D} > 0$ in green).

doping on magnetic properties of the compound. In order to identify suitable dopants we investigate the Mn_3Ge compound by total energy comparisons using the DFT methods as introduced in Sec. 3.1. Here, we use the VASP code (cf. Sec. 3.2.1) as before. In a first step, we calculate the *defect formation energies* ΔE_D corresponding to the replacement of one atom with a dopant element. We do this in a supercell approach to achieve low doping concentrations, where we replace a single Mn atom in a 32-atom $2\times2\times2$ unit cell, i.e., replacing one of 24 Mn atoms. For both Mn sublattices $\mathrm{Mn_I}$ and $\mathrm{Mn_{II}}$ we calculate the effect of doping separately.

The resulting energy differences when replacing a single atom are on the eV scale, thus, strong convergence criteria as used in the previous Chapter 5 are not required for these considerations. We chose a moderate plane wave cutoff energy of 450 eV and a **k**-point mesh of $7\times7\times7$, which is sufficiently dense considering a $2\times2\times2$ supercell. The exchange and correlation contributions are modeled by the PBE GGA functional [86]. The total energy convergence is set to 0.1 meV.

The resulting composition is $Mn_{2.875}Z_{0.125}Ge$ within our supercell approach, where Z is the dopant element under investigation. The defect formation energy ΔE_D, the difference in formation energy between the undoped and doped compound, in this case is calculated as

$$\Delta E_\mathrm{D} = 8E(\mathrm{Mn_{2.875}Z_{0.125}Ge}) - 8E(\mathrm{Mn_3Ge}) + E(\mathrm{Mn}) - E(\mathrm{Z})\,, \tag{7.1}$$

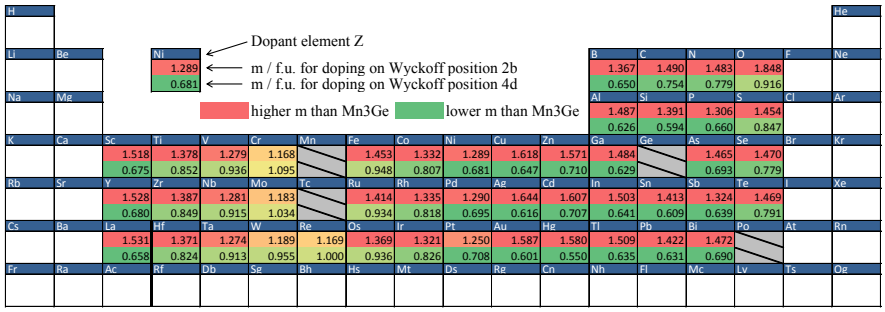

Figure 7.3. | Magnetic moment m in μ_B per formula unit of doped Mn_3Ge. For each dopant Z it is given for doping Wyckoff position $2b$ (upper) and $4d$ (lower). The color encodes the difference to the undoped Mn_3Ge of 1.034 μ_B/f.u. (smaller moment in green, larger moment in red).

where E(X) is the total energy of compound/element X. As the ground state total energies for all dopant elements are required, we performed calculations on the corresponding structures. The crystal structure and atomic positions are extracted from the Materials project [134, 135]. Calculations are repeated with our own set of numerical parameters using a dense **k**-point mesh to ensure consistency. Within our calculations, the PAW potentials as used for the elemental calculations in the Materials project are used.

Fig. 7.2 sums up the defect formation energies ΔE_D for several dopant elements throughout the periodic table of the elements. The two Mn sublattices are investigated separately. The value for doping Wyckoff position $2b$ is written in the upper field, whereas for Wyckoff position $4d$ in the lower one. The color encodes the energy gain ($\Delta E_D < 0$ in red, $\Delta E_D > 0$ in green). For six elements we find a negative ΔE_D, i.e. stabilizing the crystal structure. These are Ti and V when doping Wyckoff position $2b$, and Ni, Rh, Ir, and Pt when doping position $4d$. The energy gain is in the range of about 100-300 meV, except for Ni, where it is significantly lower at 21 meV.

In a same way, the magnetic moment per formula unit of the doped compound is presented in Fig. 7.3. As before, the corresponding value when doping Wyckoff position $2b$ is given in the upper field, and for doping Wyckoff position $4d$ in the lower one. The color encodes the difference to the undoped Mn_3Ge with a

magnetic moment of 1.034 μ_B/f.u.. Smaller moments are given in green, larger moments in red. An exclusive trend of increased moment is present when doping position $2b$. On the other hand, the moment decreases when doping position $4d$. Elements chemically similar to Mn (Cr, Mo, W, Re) show the least differences to the undoped case.

In conclusion, we found the six candidate dopants Ti, V, Ni, Rh, Ir, and Pt stabilizing the Mn_3Ge structure. For the first two, an increase in magnetization of 32% and 22% is predicted, whereas a decrease in the range of 18-35% for the rest. In the following, we investigate two of these experimentally.

7.2. Doped $Mn_{3-x}Z_xGe$

We chose Ti and Ni as dopant elements in experimental investigations. These two represent either an increased (32%) or decreased (35%) magnetization. Furthermore, among the elements decreasing the magnetization Ni is the one with the least supply risk. We prepared doped $Mn_{3-x}Z_xGe$ thin films by magnetron co-sputtering from elemental targets. As a substrate we use STO due to the low lattice mismatch already discussed in the introductory part of this chapter. The deposition was done on heated substrates at 550°C in the 2" sputtering apparatus with a processing pressure of $2.1 \cdot 10^{-3}$ mbar. After cooling down, a 2 nm protective Si layer is sputter-deposited on all samples.

The composition was adjusted to match the Mn_3Ge stoichiometry in advance. However, inconsistencies within the composition analysis lead to a detailed investigation including independent analyses by external service providers. Besides our own measurements using XRF and EDX (cf. Sec. 4.2.1, Sec. 4.2.2), we checked the composition by ICP-OES and Rutherford backscattering (cf. 4.2.3). This combined analysis revealed that the modeling of the electron excitation at the common maximum voltage of 20 kV in the electron microscope fails, as the Ge K lines (9.89 keV and 10.98 keV) are only half of the maximum excitation voltage. For proper modeling, the maximum voltage should reach 2.5 to 3 times the energy of the spectral line under investigation. Therefore, further EDX analysis is done using the Ge L_α line (1.10 keV). Despite the ICP-OES analysis (which gives a slightly too large Mn content), the results of the three other methods agree within 1% atomic content.

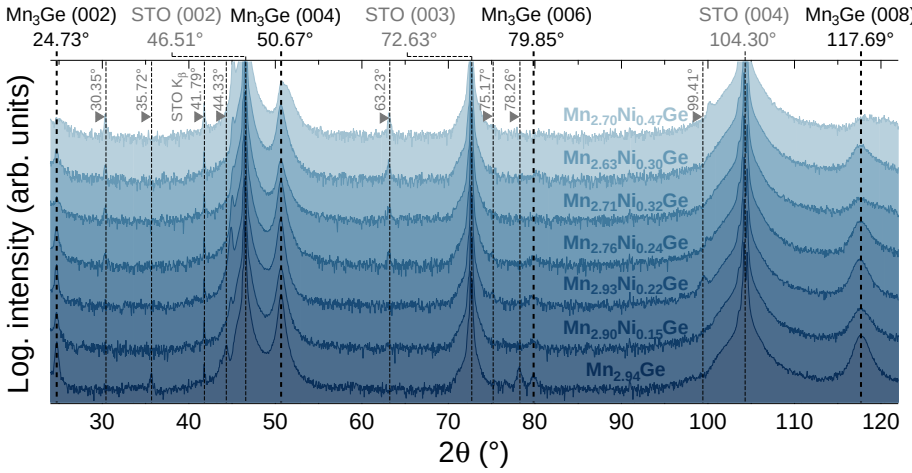

Figure 7.4. | XRD patterns of Ni doped Mn_3Ge deposited on STO substrates at 550°C. All samples have a nominal thickness of 47.8 nm.

The doped $Mn_{3-x}Z_xGe$ samples were then prepared by adding the dopant while decreasing the Mn sputter power during the deposition aiming at a constant ($Mn_{3-x}Z_x$):Ge ratio. We prepared samples with low doping concentrations resembling the theoretical investigations presented in the previous section. The final composition analysis was done using EDX to avoid the dominant diffraction artifacts of STO in XRF measurements. In the case of Z=Ni, measurements were done directly on the deposited sample. For Ti, as it is contained in STO itself, a second, amorphous glass substrate was added in the deposition process and the measurement carried out on this sample.

The film thickness for the samples was determined using XRR (cf. Sec. 4.3.2) and is 47.8 nm for all samples. XRD patterns (cf. Sec. 4.3.1) for the doped compounds can be found for Ni in Fig. 7.4 and for Ti in Fig. 7.5, respectively. For Z=Ni, all expected $D0_{22}$ peaks can be found in the patterns. The out-of-plane lattice parameter is 7.21 Å in good agreement with the results obtained for bulk Mn_3Ge reported elsewhere [173]. It does not change visibly when doping with Ni. A reduction in peak intensity can be found if the (Mn_{3-x},Z_x):Ge ratio exceeds 3:1. We explain this with the fact that in these cases Ge positions will be statistically occupied by Mn and also Ni destabilizing the crystal structure. A DFT investigation replacing one Ge atom with Ni supports this: The defect formation

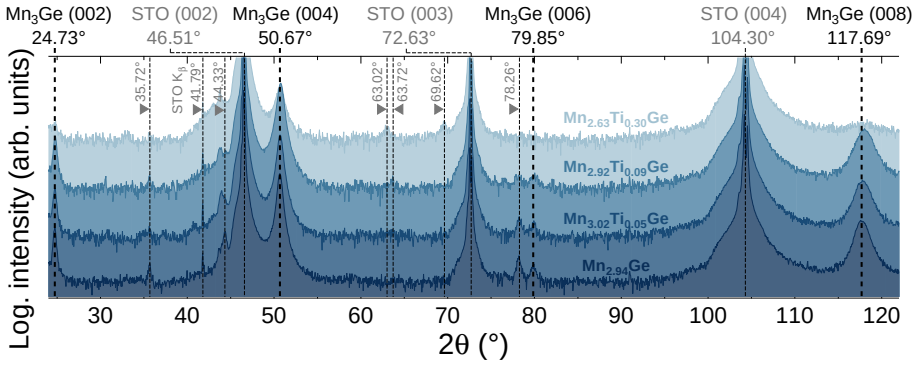

Figure 7.5. | XRD patterns of Ti doped Mn_3Ge deposited on STO substrates at 550°C. All samples have a nominal thickness of 47.8 nm.

energy in this case is clearly positive at 0.531 eV. In the case of Z=Ti as a dopant element we observe similar XRD patterns for low doping concentrations as in the undoped case. However, a shift to a smaller lattice parameter indicated by the (008) peak for $Mn_{2.92}Ti_{0.09}Ge$ is evident. For a large doping concentration the peak intensities are greatly reduced. Additionally, several unidentified peaks corresponding to impurity phases are present in all cases for both dopants as expected.

Using a vibrating sample magnetometer (VSM, cf. Sec. 4.4.1), we measured the magnetization and hysteresis loops for all samples. Hysteresis loops up to fields of 7 T were recorded both with the field swept in the sample plane as well as perpendicular to it. Together with the native Mn_3Ge reference, the corresponding measurements for Z=Ni are shown in Fig. 7.6 and for Z=Ti in Fig. 7.7. In the left graphs, the out-of-plane measurement is plotted in a blue hue, whereas the in-plane measurement in grey. All data is normalized to the sample volume by calculating the magnetic moment per formula unit. One major tick in y-direction corresponds to $0.5\,\mu_B \;\hat{=}\; 87.7\,\mathrm{kA/m}$. Interestingly, the resulting magnetization for Mn_3Ge is about half of the value predicted by DFT. This contradiction is also found by Sugihara *et al.* [174]. The deviation between theory and experiment is not yet understood and subject to current research. In all measurements a small, softmagnetic contribution is found, which is especially present in both in-plane and out-of-plane measurements. The corresponding saturation value is slightly

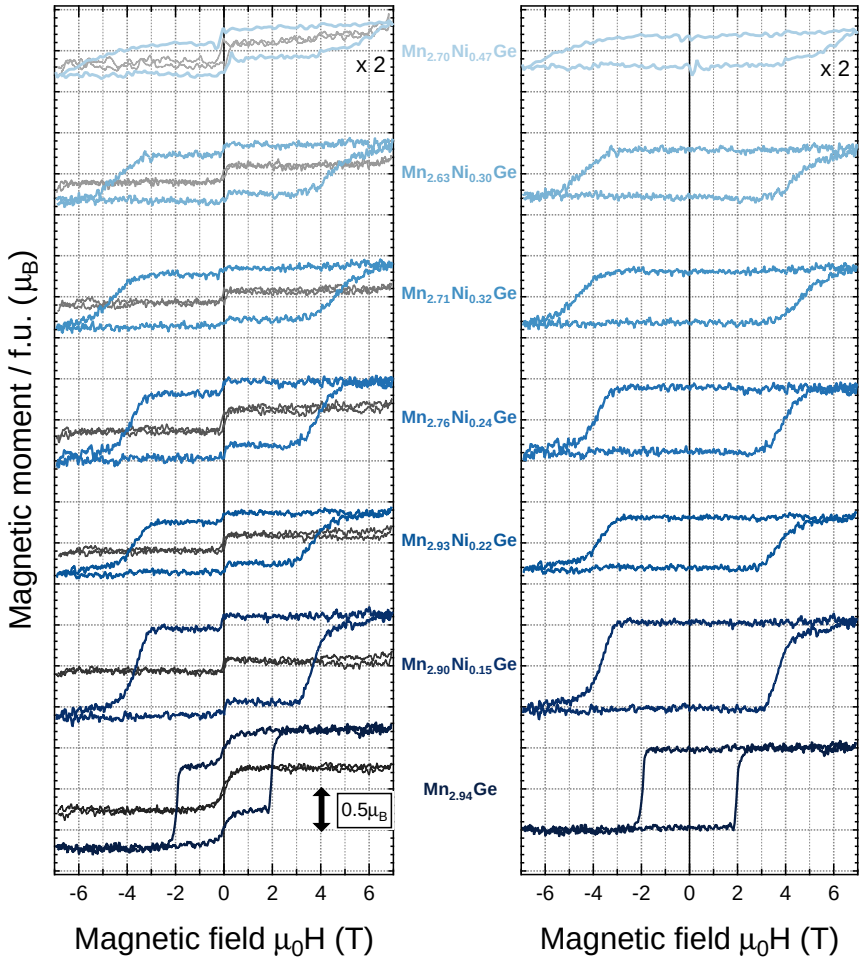

Figure 7.6. | Hysteresis loops for Ni doped Mn_3Ge. On the y-axis the magnetic moment per formula unit in terms of μ_B is plotted, where one major tick is equivalent to $0.5\,\mu_B \;\hat{=}\; 87.7\,kA/m$. Raw data is plotted on the left with the field oriented out-of-plane in blue and in-plane in grey. On the right, data where the softmagnetic contribution is fitted and removed using a Langevin function is plotted. Due to the small moment for $Mn_{2.70}Ni_{0.47}Ge$, the corresponding data is multiplied by 2. All data is corrected for the diamagnetic contribution of the substrate.

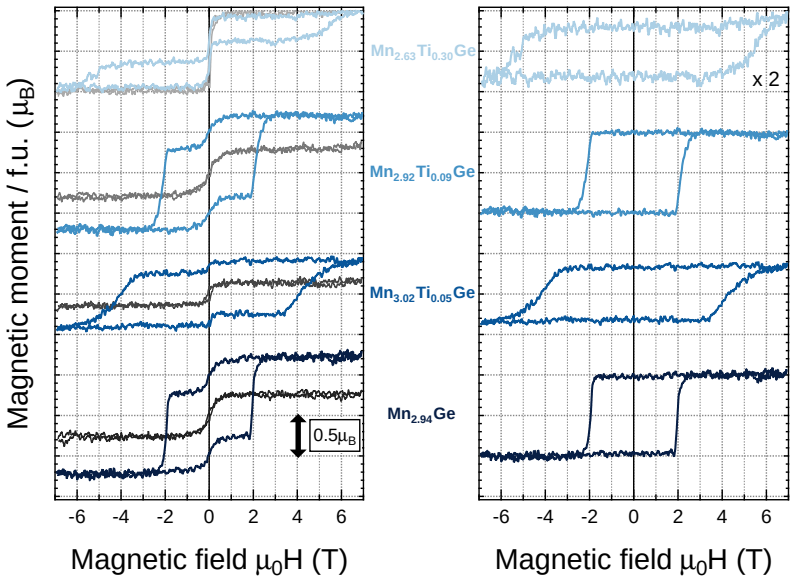

Figure 7.7. | Hysteresis loops for Ti doped Mn_3Ge. On the y-axis the magnetic moment per formula unit in terms of μ_B is plotted, where one major tick is equivalent to $0.5\,\mu_B \;\hat{=}\; 87.7\,kA/m$. Raw data is plotted on the left with the field oriented out-of-plane in blue and in-plane in grey. On the right, data where the softmagnetic contribution is fitted and removed using a Langevin function is plotted. Due to the small moment for $Mn_{2.63}Ti_{0.30}Ge$, the corresponding data is multiplied by 2. All data is corrected for the diamagnetic contribution of the substrate.

larger in the in-plane measurement in all cases. Due to this contribution, both figures include a second graph one on the right, where the softmagnetic contribution has been removed by a fit using a Langevin function $f(x) = \coth x - 1/x$. We account this softmagnetic contribution to secondary phases, which already have been observed in the XRD analysis. This assumption is supported by anomalous Hall effect [179] measurements on selected samples yielding the same results regarding switching of the hardmagnetic Mn_3Ge, however, not showing any softmagnetic switching. The conclusion is, that the softmagnetic contribution is due to secondary phases with a large Hall resistance and therefore not visible in these kind of measurements.

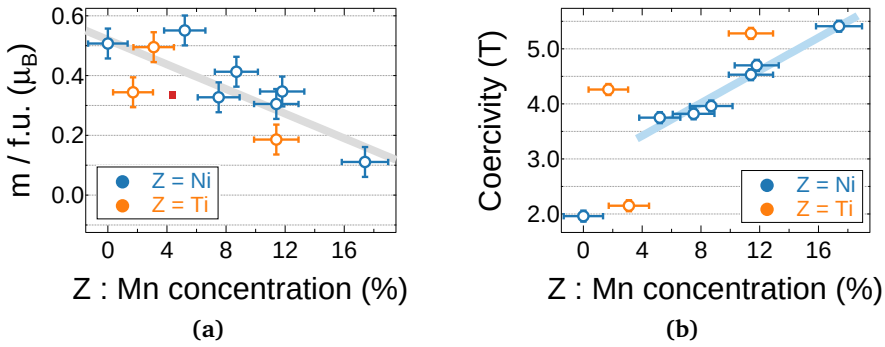

Figure 7.8. | Magnetization and coercivity depending on the dopant concentration. Values are extracted after removing the softmagnetic contribution. **(a)** The saturation magnetization shows a decreasing linear trend when increasing the dopant concentration. The shaded grey line is a linear fit to all data points. The red data point indicates the relative reduction compared to Mn_3Ge predicted by DFT. **(b)** The coercivity is proportional to the dopant concentration for Z=Ni as indicated by the blue line fitting these data points.

The magnetic measurements clearly reveal a significant effect of doping on the magnetic properties. The most striking feature is a large increase in coercivity compared to the undoped Mn_3Ge for all samples except $Mn_{2.92}Ti_{0.09}Ge$. This is accompanied by a reduction in saturation magnetization in most cases. After removing the softmagnetic contribution, the saturation magnetization and coercivity values are extracted from the VSM data. The results are plotted in Fig. 7.8 for Z=Ni in blue and for Z=Ti in orange. On the x-axes, the Z:Mn concentration is plotted, as these are the two magnetic species in the compound. The error bars are attributed to the typical accuracy in the composition analysis, and noise in the VSM measurement. The magnetization is decreasing for increasing doping concentrations for both dopants, plotted in Fig. 7.8a. The shaded grey line is a fit to all data points showing the roughly linear trend. Marked in red is the reduction in magnetization of 32% for Z=Ni compared to native Mn_3Ge predicted by DFT. The predicted relative reduction is at least in a similar order as measured in the experiment. In Fig. 7.8b, the coercivity is plotted against the dopant concentration. The coercivity depends linearly on the concentration when doped with Ni as

indicated by the linear fit plotted in light blue. Remarkably, compared to native Mn_3Ge the coercivity is increased by a factor of 2.8 to 5.41 T for $Mn_{2.70}Ni_{0.47}Ge$.

The doping with Z=Ti requires some additional discussion. Unfortunately, we don't find an increase in magnetization as predicted by the DFT calculation. Furthermore, the effect on the hysteresis loop seemingly depends strongly on the Ti concentration. For $Mn_{3.02}Ti_{0.05}Ge$, an increase in coercivity and reduction in saturation magnetization is found similar to the Ni-doped samples. Surprisingly, for $Mn_{2.92}Ti_{0.09}Ge$, both values and the whole hysteresis loop are almost equal to the undoped Mn_3Ge. Increasing the Ti concentration further to $Mn_{2.63}Ti_{0.30}Ge$, we find an effect similar to the Ni-doped samples again. A possible explanation for this behavior and the contrarily predicted increase in saturation magnetization are the defect formation energies for Z=Ti. We find $\Delta E_\mathrm{D} = -0.309\,\mathrm{eV}$ (position $2b$) and $\Delta E_\mathrm{D} = 0.066\,\mathrm{eV}$ (position $4d$). The latter value is small, so a not negligible occupation of the $4d$ positions by Ti atoms is possible, which may lead to a considerable effect on magnetic properties. To check this, an investigation of the doping with V not covered by this work is suggested, where the same increase in magnetization as for Ti is predicted. The defect formation energy for position $4d$ $\Delta E_\mathrm{D} = 0.227\,\mathrm{eV}$ is clearly positive, so a V occupation should be negligible.

We investigated selected samples using X-ray magnetic circular dichroism[1] (XMCD, cf. Sec. 4.5.1) techniques to get a better insight of the ferrimagnetic configuration. The measurements were done in total electron yield mode. As the samples exhibit two magnetic contributions, the soft- and hardmagnetic one, we followed two different approaches to separate the corresponding parts. In the first approach, four XMCD spectra measured perpendicular to the film plane have been recorded for all selected samples: one for both $+300\,\mathrm{mT}$ and $-300\,\mathrm{mT}$ magnetic field applied both in the forth and back loop of the hysteresis. These four spectra correspond to the four possible relative orientations of the two magnetic parts. This allows us to separate the two contributions by adding and/or subtracting the spectra in the correct order. We call this the additive approach in the following.

As the softmagnetic component has no preferred orientation, it is possible to align the two contributions perpendicularly, so only one is probed by the XMCD

[1] XMCD measurements were performed at beamline 4.0.2 of the Advanced Light Source in Berkeley, CA, U.S.

measurement. Using this second approach, the separative approach, we oriented the softmagnetic contribution in-plane using the external magnetic field. Under an angle of 20° between the X-rays and the sample plane we measured the softmagnetic contribution in in-plane geometry. In contrast, the hardmagnetic one was measured under an angle of 70°. This is necessary, as otherwise no signal is measured due to the electrons being redirected back onto the sample by the perpendicular applied magnetic field.

In Fig. 7.9, a comparison between the undoped $Mn_{2.94}Ge$ and samples doped with Ti and Ni is presented. The graphs show the XMCD difference at the Mn L_3 and L_2 edges obtained from XA spectra normalized to 1 before the L_3 edge (a normalized Mn XA spectrum is exemplarily shown in the inset of Fig. 7.9a). In blue, the hardmagnetic contribution is plotted, whereas in orange the softmagnetic one. The shaded lines represent data obtained in the additive approach, whereas the solid lines data obtained in the separative approach. Generally, the plots show that the two approaches yield equivalent results; despite small deviations in the softmagnetic part, neither the spectral form nor the absolute signal amplitudes are affected by the different approaches.

The XMCD spectrum for $Mn_{2.94}Ge$ plotted in Fig. 7.9a shows a distinct structure. We observe an overall negative tendency in the signal at the Mn L_3 edge. This is super-imposed by a second, positive contribution. We interpret this result as a superposition of two Mn XMCD spectra with different amplitude and sign, shifted on the energy axis. This is attributed to the two magnetic Mn sublattices in the ferrimagnetic configuration of $Mn_{2.94}Ge$. This superposition is observed at the L_2 edge as well. The softmagnetic component has a smaller amplitude and shows no distinct structure. This is indicative of an individual magnetic species independent of the ferrimagnetic $Mn_{2.94}Ge$ structure. It supports our previous assumption, that the softmagnetic component originates from secondary phases observed in the XRD analysis. Small deviations in the measurements between the additive and separative approach, like at the L_2 edge, are not yet understood. As previously discussed, the in-plane softmagnetic component is slightly larger than the out-of-plan component, which is possibly linked to the observed deviations.

In Fig. 7.9b and Fig. 7.9c XMCD spectra for Ti- and Ni-doped Mn_3Ge are shown in direct comparison to the ones for $Mn_{2.94}Ge$. In both cases we observe a general reduction in the signal amplitude. This corresponds to the reduced magnetization we already measured with the VSM. The softmagnetic contribution is reduced as

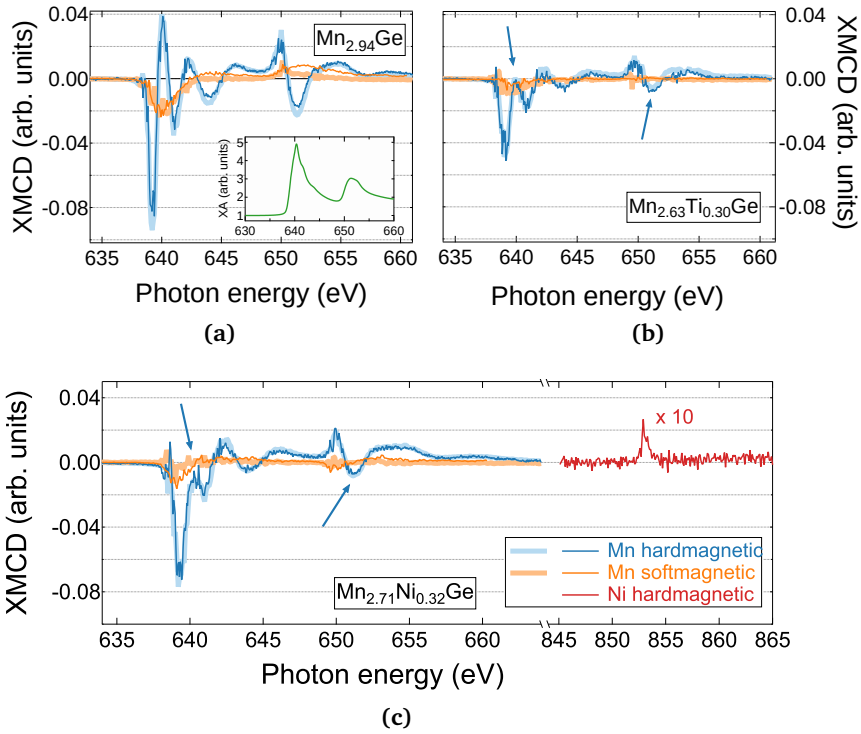

Figure 7.9. | XMCD analysis of undoped and doped Mn_3Ge samples using the additive (shaded lines) and separative (solid lines) approach. The hardmagnetic contribution is plotted in blue whereas the softmagnetic one in orange. Arrows mark peaks in the hardmagnetic spectrum exhibiting a slightly increased reduction in amplitude compared to the overall spectrum. **(a)** XMCD spectra of $Mn_{2.94}Ge$. The inset shows the averaged XA spectrum. **(b)** XMCD spectra of $Mn_{2.63}Ti_{0.30}Ge$. **(c)** XMCD spectra of $Mn_{2.71}Ni_{0.32}Ge$. Additionally plotted in red is the Ni XMCD signal at the L_3 edge. This data is multiplied by ten.

well, making a quantitative analysis difficult. In the hardmagnetic contribution we make an interesting observation marked by the arrows (⇓) in both graphs. Compared to the overall spectrum, the partial XMCD signal with positive sign at the L_3 edge is considerably more reduced and suppressed. This can also be observed for the corresponding part at the L_2 edge. Thus, we conclude that one Mn sublattice is magnetically more affected by the doping than the other. We

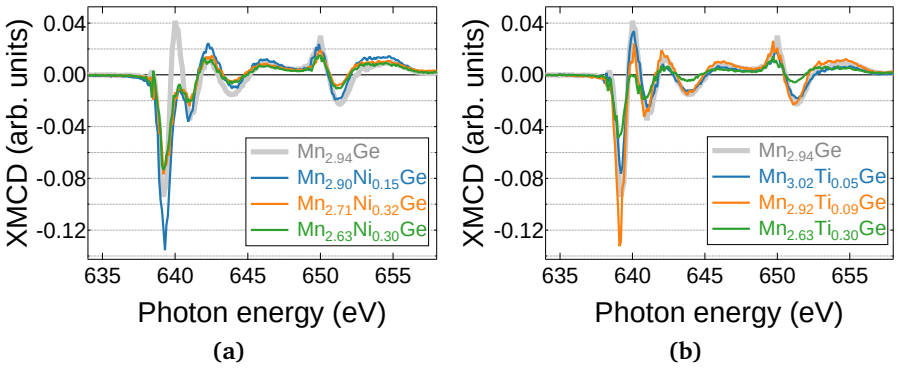

Figure 7.10. | Mn XMCD spectra for different dopant concentrations. **(a)** Spectra for Ni-doped samples. **(b)** Spectra for Ti-doped samples.

attribute the larger net signal (negative sign at the L_3 edge) to the $4d$ sublattice, which has the larger net magnetic moment in sum.

We also investigated the XMCD of Ni and Ti in order to learn about the relative coupling between the dopant element and Mn. Unfortunately, due to the low doping concentrations, a reasonable signal for Ti could not be measured. For Ni we were able to measure an XMCD spectrum using the separative approach. It is plotted additionally in red in Fig. 7.9c. Due to the tiny signal amplitude the data is multiplied by ten. We observe a clearly positive signal at the Ni L_3 edge. Combined with the Mn XMCD analysis we conclude that the Ni moment is antiparallel coupled to the overall Mn moment, and oriented parallel (antiparallel) to the Mn moments on the $2b$ ($4d$) sublattice. This relative orientation agrees with the prediction from our DFT calculation. However, from this analysis we cannot deduce which sublattice the Ni atoms occupy.

Mn XMCD spectra for different dopant concentrations are plotted in Fig. 7.10. All shown spectra are recorded using the additive approach. In Fig. 7.10a, for a low Ni concentration in $Mn_{2.90}Ni_{0.15}Ge$ we already observe a significant reduction in the positive peak at the L_3 edge compared to the $Mn_{2.94}Ge$ spectrum. On the other hand, the negative dip is more pronounced. This is consistent with the magnetization measurements in the VSM, where a slightly increased saturation magnetization is observed for this sample. For $Mn_{2.71}Ni_{0.32}Ge$ and

$Mn_{2.63}Ni_{0.30}Ge$, the negative dip is considerably reduced as well. The spectra for these two samples are nearly identical. Thus, the slightly different Mn content does not significantly affect the overall spectrum.

The analysis of the Ti doped samples in Fig. 7.10b supports the observation obtained from the hysteresis loop measurements: For $Mn_{3.02}Ti_{0.05}Ge$, the overall signal amplitude is reduced just as the saturation magnetization is reduced. For $Mn_{2.92}Ti_{0.09}Ge$, the overall signal amplitude is increased again, especially for the negative dip at the L_3 edge. Further increasing the concentration to $Mn_{2.63}Ti_{0.30}Ge$ again reduces the signal amplitude. Considering the partial XMCD signal with positive sign at the L_3 edge suggests that the asymmetry in the effect on the two sublattices is less than for Z=Ni. This supports our hypothesis that Ti does not exclusively occupy (or, at least, affect) one sublattice.

Using the *sum rules* [180], it is possible to deduce the magnetic moment per atom from the XAS and XMCD data [181, 182]. Unfortunately, an application to the data presented in this work yielded no reasonable results. This may have several reasons. First, the Mn L_3 and L_2 edges considerably overlap (see the inset of Fig. 7.9a). This makes an evaluation of the required integrals restricted to one of the edges difficult. Second, in the XAS spectrum of Mn, small shoulders can be observed. It is yet unclear if these are attributed to the ferrimagnetic structure of the compound or slight oxidation effects possibly caused by the samples' high roughness. As shown by Meinert *et al.* [181, 182], DFT allows to calculate the XMCD spectrum and separate the sublattice contributions. Within future work, we will calculate these and compare the data to the measured spectra to gain a better understanding of the different contributions and couplings.

To summarize, this chapter successfully combined theoretical and experimental methods to tune the magnetic properties of the ferrimagnetic Mn_3Ge compound. Using DFT we are able to predict suitable dopant elements. In the case of Z=Ni, we demonstrated that even a precise qualitative prediction for the internal ferrimagnetic structure is possible. The doped samples exhibit a giant coercivity of up to more than 5 T combined with a very low saturation magnetization of roughly $0.1\mu_B$/f.u., which are interesting parameters for the application in spintronic devices. In a next step, subsequent work will investigate the combination of the material and a thin, ferromagnetic layer deposited on top of it in order to realize spin valves and TMR devices.

8

Summary and Outlook

Antiferromagnets are a crucial part of spintronics. Not only used to mediate the exchange bias effect, recently they are used itself to store data in. Their fundamental importance cannot be denied, therefore it is all the more problematic that the most commonly used antiferromagnet consists of the rare and costly Ir.

In combining powerful theoretical methods with experiments, this work describes a guideline to discover novel antiferromagnetic materials in order to replace the common antiferromagnet IrMn. In the first part of this thesis, Chapter 5, we demonstrate how density functional theory can predict hitherto unknown antiferromagnetic materials. We utilize the AFLOWLib, a high-throughput computational material database forming compounds combinatorically to investigate structural and magnetic properties of, e.g., Heusler compounds. This ternary family is known to exhibit a large variety of properties, hence an investigation among them is meaningful.

We did this in a high-throughput framework with the AFLOWLib as the basis of our work. Out of about 80 000 Heusler compounds in the database, we identified magnetic ones with a negative formation energy, which is a necessary condition for thermodynamic stability. As compounds with the same constituents in different compositions may be energetically favored, we extended this consideration by calculating the convex hull of the formation energy for all of our candidates. The distance to this mathematical construct is a more reliable measure for the

thermodynamic stability than the formation energy, and serves as a guideline for experimentalists to synthesize novel materials. In supercell calculations forming the AF1 and AF2 antiferromagnetic states we determined the magnetic ground state for 291 Heusler compounds and found 70 with an antiferromagnetic ground state. This small number, compared to the initial basis, demonstrates the difficulty of this problem, which is hard to face by experiments alone.

The Néel temperature plays an important role for applications. Therefore, we estimated it for the candidate materials by calculating the Heisenberg exchange parameters using multiple scattering theory. Atomistic spin dynamic calculations on the temperature dependence of magnetic properties using these parameters in a Monte Carlo simulation gave us reliable estimations. All in all, we identified 21 antiferromagnetic Heusler compounds with a Néel temperature above room temperature. For about a third of these, the antiferromagnetic ground state is confirmed by experiments. A further review on the literature reveals the excellent selectivity of our method: Out of the 70 compounds predicted to be antiferromagnetic, we find discrepancies with experimental results in only four cases. These, however, can be explained by systematic shortcomings of our method.

These shortcomings are mainly conceptual. The thermodynamic stability evaluated using the convex hull critically relies on the completeness of the underlying database. Although it is nearly impossible to include every composition / crystal structure combination, this problem is already continuously minimized by the AFLOW consortium by adding more and more data sets. This goes similarly for atomic disorder in the compound. Furthermore, our considerations only included two highly symmetric antiferromagnetic states. There are many other, more complex antiferromagnetic states including frustrated and spin spiral states. It is also not possible to include all of these in the workflow. All the more, the accuracy of predictions at the current level revealed by our comparison with published experimental data is astonishing. Finally, our Monte Carlo simulations indicate that the magnetic ground state is often different and more complex than we assumed. A detailed investigation of selected cases is left to be investigated by future work. A hybrid DFT - Monte Carlo theory feeding the magnetic ground state found by the spin dynamic calculation back into a DFT cycle could determine the true ground state self consistently.

Many of these obstacles can be overcome with the steadily increasing available computational power. In the near future it will be possible to include a much

more extended database to improve the quality of results. Furthermore, this method is not restricted to the Heusler structure and can be easily extended for other systems. Even an investigation of quarternary compounds will be possible with a decent amount of computational power.

In the second part of this thesis we investigated one of the candidate materials, the Ru_2MnGe compound, in Chapter 6. Using magnetron co-sputtering we prepared epitaxial and polycrystalline Ru_2MnGe thin films. Especially the epitaxial films show very good crystalline growth. Utilizing the anisotropic magnetoresistance, we measured the exchange bias in Ru_2MnGe / Fe bilayers. We find sizable exchange bias fields of $H_{ex} = 60.0\,\mathrm{mT}$ for epitaxial films and $H_{ex} = 44.5\,\mathrm{mT}$ for polycrystalline films at 3 K. By adding a few monolayers thick intermediate Mn layer we were able to increase the exchange bias by 40% for polycrystalline samples. Measuring the exchange bias at different temperatures we find an upper limit for the blocking temperature T_B of 130 K for epitaxial samples and 30 K for polycrystalline ones. We explain this difference with the different types of crystalline growth either using heated substrates or rapid thermal annealing. Already published work on IrMn-based exchange bias systems indicate that the temperature stability in epitaxial films can be improved by doping. We investigated this for small doping concentrations of Ta, however, we could not observe an improvement. A more extensive investigation using different dopant materials and concentrations is yet to be done.

In the next part we demonstrate the integration of Ru_2MnGe into spintronic devices as a pinning layer. Detailed analyses of epitaxial Ru_2MnGe thin films and full magnetic tunneling stacks using different microscopy techniques underlined the good crystalline quality of our films and the tunneling barrier. By patterning magnetic tunneling junctions using UV lithography and measuring the magnetoresistance at low temperatures we show a distinct magnetic switching of the resistance with a tunneling magnetoresistance amplitude of around 100%, which can be increased by post annealing. To the best of our knowledge, this is the first demonstration of a magnetoresistive device using an antiferromagnetic Heusler as a pinning layer. Unfortunately, a working device using polycrystalline Ru_2MnGe could not be realized, yet.

A promising, alternative material is investigated in the last part of this work presented in Chapter 7. The Mn_3Ge compound is known for its combination of high coercivity and low saturation magnetization. These parameters are in-

teresting for spintronic applications, as a material of sufficiently large coercivity might provide a similar magnetically stable reference as exchange biased materials. Based on already published work we investigate the possibility of tuning the magnetic properties via doping. In order to do so, using density functional theory we calculate the defect formation energies arising when substituting one of 23 Mn atoms in a $2 \times 2 \times 2$ supercell. We identify six suitable dopant elements with a negative defect formation energy. Depending on whether the $2b$ or $4d$ Mn sublattice is occupied by a specific dopant, an increase or decrease in the magnetization is predicted.

We experimentally investigated two of the six suggested dopant elements: Ni and Ti. Our calculations predict a decrease in magnetization for Ni and an increase for Ti. We prepared a series of samples for both dopant elements with different concentrations using magnetron co-sputtering. Indeed, we find a crystallization of the Mn_3Ge phase for doped samples. These were further investigated in a vibrating sample magnetometer measuring the saturation magnetization. These measurements show two interesting features: Generally, the coercivity is greatly enlarged, reaching up to more than 5 T for some of the samples. For doping with Ni we find a decrease in the magnetization just as predicted. The absolute values of the saturation magnetization, however, deviate from the calculations. This deviation is known for the Mn_3Ge compound and not understood, yet. For doping with Ti we find deviating results strongly depending on the dopant concentration. We explain this by the positive, but small Ti defect formation energy for the second Mn sublattice, which may lead a to non negligible occupation of both sublattices by Ti.

The element specific magnetism can be probed by X-ray magnetic circular dichroism. We performed measurements on selected samples at beamline 4.0.2. of the Advanced Light Source in Berkeley, CA. This gives us information about the element specific magnetic configuration. Our results indicate that the net magnetic moment of one Mn sublattice is preferably suppressed by doping especially in the case of Ni. Furthermore, the magnetic coupling of the Mn sublattices in relation to the Ni moments is as predicted by our calculations. A small softmagnetic contribution is present for all characterized samples, which is often observed for the Mn based $D0_{22}$ systems. By separating this contribution from the hardmagnetic part we are able to investigate its origins. The distinct structure attributed to the ferrimagnetic configuration observed in the Mn spectrum for the hardmag-

netic part is missing in the softmagnetic part. Therefore, we conclude that this contribution is due to unknown, secondary phases, which are already observed in the X-ray diffraction patterns for all samples, and is not accounted to the Mn_3Ge phase itself.

All in all, we successfully reduced the saturation magnetization of the Mn_3Ge compound by doping, which involves a large increase in coercivity. The combination of these effects makes this compound even further interesting for the integration into spintronic devices. As a next step, the magnetic properties of samples with an additional ferromagnetic layer on top are to be investigated. Furthermore, the metastable Mn_3Ge is formed by forced epitaxy. A drawback in this compound is the interface roughness, which is reduced in the native bulk composition $Mn_{3.4}Ge$. Thus, an investigation of doping $Mn_{3.4}Ge$ as well is suggestive. In addition, as outlined in Chapter 7, reports on special deposition procedures successfully reducing the roughness greatly even for Mn_3Ge exist.

To conclude this thesis, we point out the powerful combination of theoretical and experimental methods. The state-of-the-art density functional theory is a wide spread method with enormous potential in predicting, tuning and understanding the electronic structure of atoms, molecules and solids. Within this work we demonstrate this by the prediction of new materials and the tuning of specific material properties. The theoretical support guides our experiments and helps to understand and interpret our results. For certain tasks, such as a high-throughput search for novel materials, this is even indispensable, as one side alone cannot handle all necessities.

A

Antiferromagnetic Unit Cells

The following Tab. A.1 lists the geometry of the AF unit cells used in the supercell calculations. The unit cell vectors $\mathbf{a}_1$, $\mathbf{a}_2$ and $\mathbf{a}_3$ are given in terms of the lattice parameter a. For each of the eight given atomic positions, an arrow indicates the relative orientation (either "up" or "down") of the initial magnetic moment.

Table A.1. | Unit cell vectors and atomic positions for AF1 and AF2 unit cells. a is the lattice parameter. Arrows denote the initial orientation of the magnetic moments.

	AF1 State		AF2 State	
$\mathbf{a}_1$	(0.5a, 0.5a, 0.00)		(0.00, 0.5a, -0.5a)	
$\mathbf{a}_2$	(0.00, 0.00, a)		(a, 0.5a, 0.5a)	
$\mathbf{a}_3$	(0.5a, -0.5a, 0.00)		(0.5a, 0.00, -0.5a)	
X_1	(0.00, 0.00, 0.50)	↑	(0.500, 0.500, 0.000)	↑
X_2	(0.50, 0.00, 0.00)	↑	(0.000, 0.000, 0.000)	↓
X_3	(0.00, 0.50, 0.50)	↓	(0.750, 0.250, 0.500)	↑
X_4	(0.50, 0.50, 0.00)	↓	(0.250, 0.750, 0.500)	↓
Y_1	(0.00, 0.25, 0.00)	↑	(0.625, 0.875, 0.750)	↑
Y_2	(0.50, 0.75, 0.50)	↓	(0.125, 0.375, 0.750)	↓
Z_1	(0.50, 0.25, 0.50)	↑	(0.375, 0.125, 0.250)	↑
Z_2	(0.00, 0.75, 0.00)	↓	(0.875, 0.625, 0.250)	↓

B

Convergence Tests

B.1. VASP

In order to achieve accurate predictions, the total energies and especially the energy differences ΔE_{AF1} and ΔE_{AF2} need to be converged to an adequate energy scale. For the difference between magnetic couplings this scale is of the order of 1 meV, which is set as our convergence target. We investigated the convergence depending on several numerical parameters. The total energy convergence target for a self-consistent calculation has been set to 5×10^{-5} eV. An investigation of different values revealed no significant influence on the total energy convergence. The same results are obtained from a convergence test for the plane wave cutoff energy. For all calculations we use a cutoff of 500 eV, which is of the same order as used in the AFLOWLib.

The most significant numerical parameter is the number of **k**-points used for Brillouin zone integration. For the integration we use the tetrahedron method with Blöchl corrections [183]. The results of a corresponding convergence test using a Γ-centered **k**-point mesh are plotted in Fig. B.1. Here, the convergence of E_{FM}, E_{AF1}, E_{AF2}, ΔE_{AF2}, and ΔE_{AF2} with respect to the number of **k**-points N_{k} is plotted. The values given are energy differences to the calculation using the most **k**-points $N_{\mathrm{k}}^{\mathrm{max}}$, e.g., for the FM state $E_{\mathrm{FM}}(N_{\mathrm{k}}) - E_{\mathrm{FM}}(N_{\mathrm{k}}^{\mathrm{max}})$. The maximum

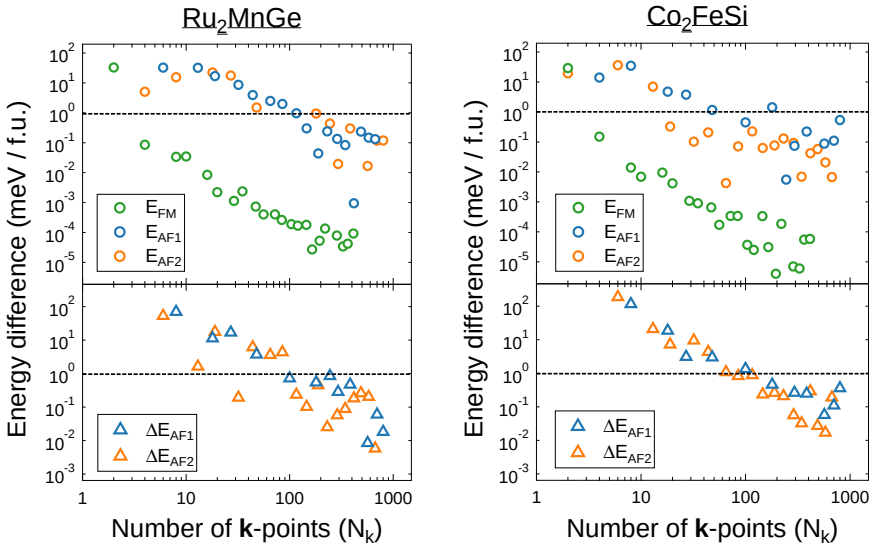

Figure B.1. | Convergence of total energies (upper) and energy differences between FM and AF states (lower). Given values are with respect to the calculation using the most **k**-points. Dashed lines mark the 1 meV convergence target. **(a)** Convergence for antiferromagnetic Ru_2MnGe. **(b)** Convergence for ferromagnetic Co_2FeSi.

numbers are: For the FM state $N_{\mathrm{k}}^{\mathrm{max}} = 455$, for the AF1 state $N_{\mathrm{k}}^{\mathrm{max}} = 968$, and for the AF2 state $N_{\mathrm{k}}^{\mathrm{max}} = 781$. This corresponds to a $25 \times 25 \times 25$ **k**-points mesh for the FM state and a $20 \times 20 \times 20$ mesh for the AF configurations. Furthermore, due to the asymmetric elongation in the [001] direction for AF1, the sampling in this direction is reduced accordingly.

To cover the most possible outcomes, the convergence check was done for two different systems: The antiferromagnetic Ru_2MnGe (Fig. B.1a) and the ferromagnetic Co_2FeSi (Fig. B.1b). A similar convergence behavior is found for both systems, however, in the case of Co_2FeSi the scattering is larger, most likely due to the fact that Co_2FeSi is not antiferromagnetic. For the FM state, which only includes four atoms, a convergence to 1 meV is easily achieved. For the AF states, however, significantly more **k**-points are required. Generally, at least 200

k-points are required to achieve the 1 meV accuracy. In the following, to ensure convergence in every case, for the FM state a $20 \times 20 \times 20$ mesh is used as well as a $16 \times 16 \times 16$ mesh as a basis for the AF configurations. This corresponds to 256 **k**-points for the FM state, 567 for the AF1 state and 417 for the AF2 state.

B.2. Monte Carlo

For the MC simulations, extensive convergence tests were also performed. All presented calculations in this chapter are for the Rh_2MnAl system in the AF2 state. We started investigating the effect of a finite simulation box. The results are plotted in Fig. B.2a. The plot shows the heat capacity calculated from fluctuation (c_F, open circles) and as a derivative of the total energy (c_S, thick, shaded line). Plots which use parameters as used in all final calculations are marked with a red asterisk (*). Results for a simulation box of $8\times8\times8$, $10\times10\times10$, $15\times15\times15$ and

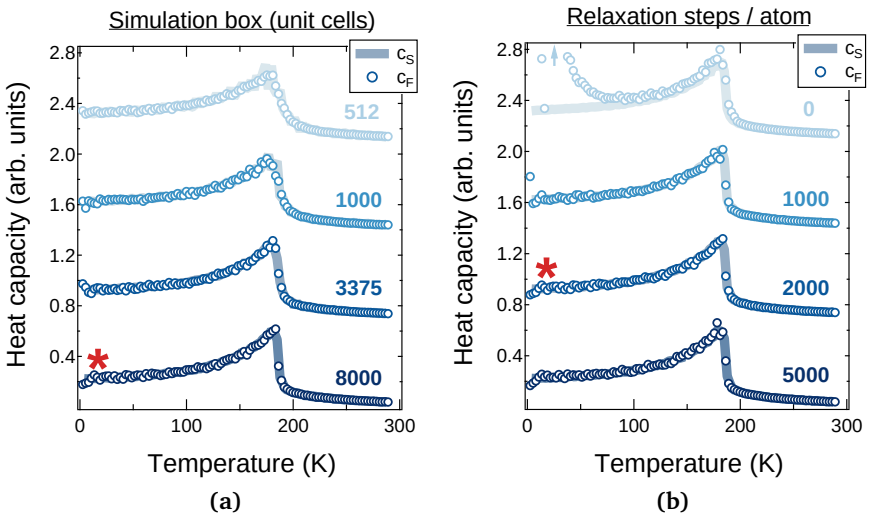

Figure B.2. | Influence of MC parameters on calculated values. A red asterisk (*) marks calculations with parameters used throughout the screening process. **(a)** Dependence on the simulation box size, or, equivalently, number of included unit cells. **(b)** Dependence on the number of relaxation steps made at each temperature.

$20 \times 20 \times 20$ unit cells are shown. To avoid unwanted finite size effects not visible in these checks, we chose the largest box of $20 \times 20 \times 20$ as our final parameter. The results are barely affected by the finite size, however, c_{S} fluctuations around the transition temperature are found for small box sizes. The effect of relaxing the system before MC integration at each temperature is investigated in Fig. B.2b. Too few relaxation steps clearly affects the results. We chose 2 000 steps per atom, as further increasing the number of steps did not affect the results.

We find the parameter, the quality of results is most sensitive to, is the number of performed MC steps within the MC integration. Results for a variety of different numbers are plotted in Fig. B.3a. Heavy fluctuations in the results are found for small numbers of MC steps making an analysis difficult. The effect ceases at around 10 000 steps per atom. We further increased the final parameter to 20 000 MC steps per atom to ensure high quality results in every case. Finally, we investigated the dependence of the obtained transition temperature on the included interaction radius. Primarily, the mean field Néel temperature $T_{\mathrm{N}}^{\mathrm{MF}}$ is plotted against the included interaction radius r in terms of the lattice constant in Fig. B.3b. Here we see a convergence of $T_{\mathrm{N}}^{\mathrm{MF}}$ beyond $r = 3.5a$. We support this by MC simulations using different interaction radii. As the susceptibility visually yields the easiest plot to determine the transition temperature, it is plotted for several interaction radii in Fig. B.3c. The transition temperature is crucially affected by this, however, for a larger interaction radius $r > 3.0a$, the deviations are small. We chose to include all interactions we obtained from the exchange parameter calculation, i.e., up to an interaction radius of $r = 4.5a$.

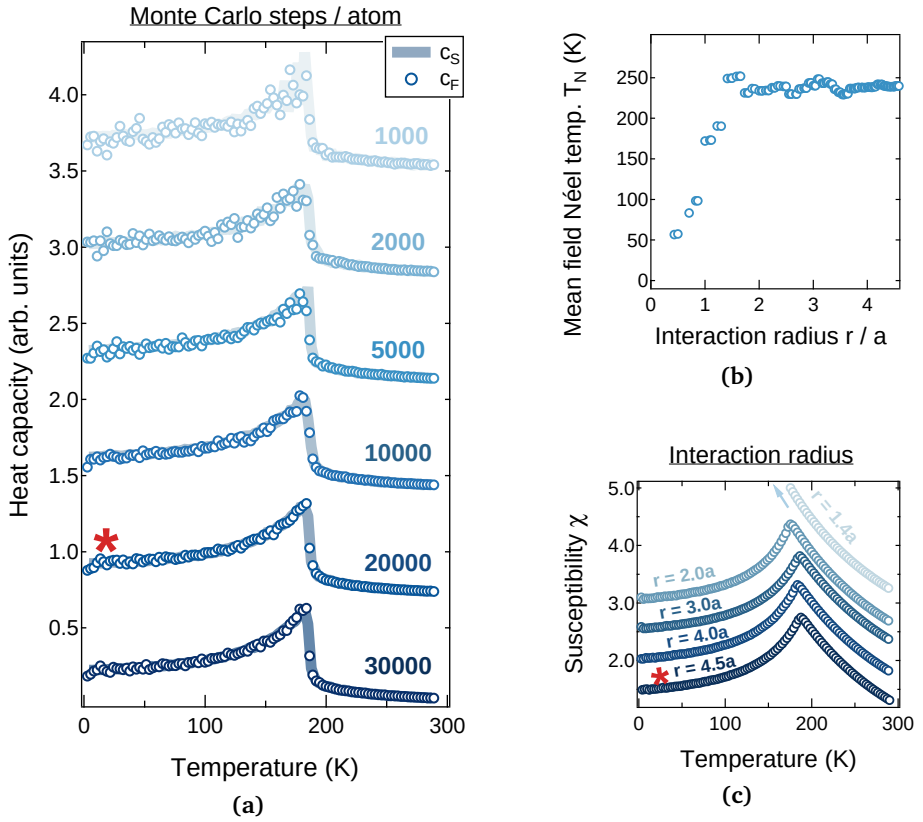

Figure B.3. | Influence of the used interaction radius and number of MC steps on calculated values. A red asterisk (*) marks calculations with parameters used throughout the screening process. **(a)** Calculated heat capacity for different number of MC steps. **(b)** Interaction radius dependence of the mean field Néel temperature $T_{\mathrm{N}}^{\mathrm{MF}}$. **(c)** Position of the magnetic phase transition depending on the included interaction radius r.

C

Antiferromagnetic Heusler Compounds: Detailed Results

The two graphs filling the next two pages show all calculated Néel temperatures in comparison (conventional Heusler in Fig. C.1 and unconventional ones in Fig. C.2). In the following, then a detailed data set for all 70 AF Heusler compounds predicted by the DFT screening from Chapter 5 is provided. For each compound information about the ground state as well as a table containing all relevant data obtained by the calculations is given. For the sake of legibility, units are omitted in the tables. The tables contain information about:

- The crystal structure (lattice parameter a in Å, c/a ratio with the lattice parameter c in [001] direction)
- Magnetic configuration (average absolute magnetic moment per site m_{X}, m_{Y}, m_{Z}, and absolute total moment per f.u. m_{tot}, all in terms of μ_{B})
- Transition temperatures in K (calculated in MFA ($T_{\mathrm{N}}^{\mathrm{MF}}$), by MC ($T_{\mathrm{N}}^{\mathrm{MC}}$), and in a second nearest neighbor model if applicable ($T_{\mathrm{N}}^{\mathrm{2nn}}$))
- The spin-spin correlation function ζ (cf. Eq. (5.5)). If the MC ground state matches the expectation this is marked with an asterisk.

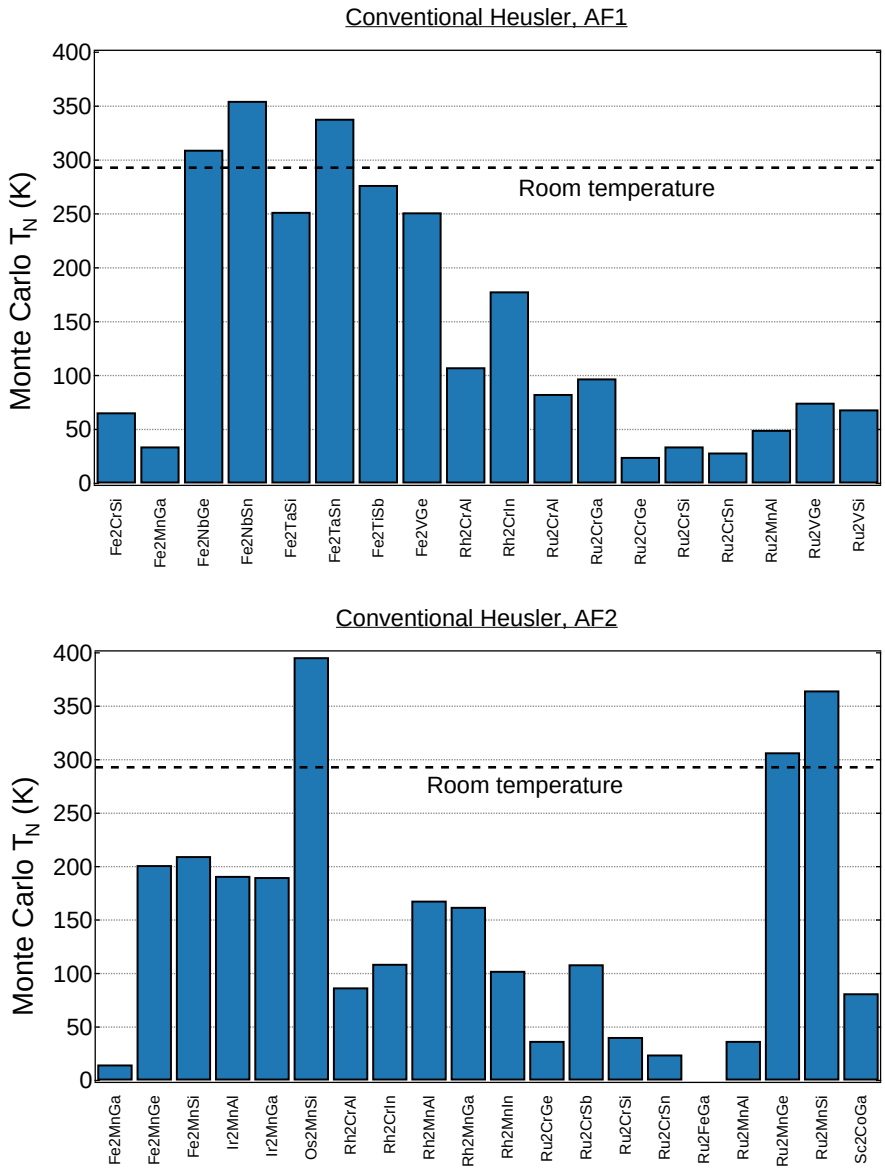

Figure C.1. | Calculated Néel temperatures for all conventional AF Heusler compounds. The top graph shows compounds in AF1 state, the bottom one in AF2 state.

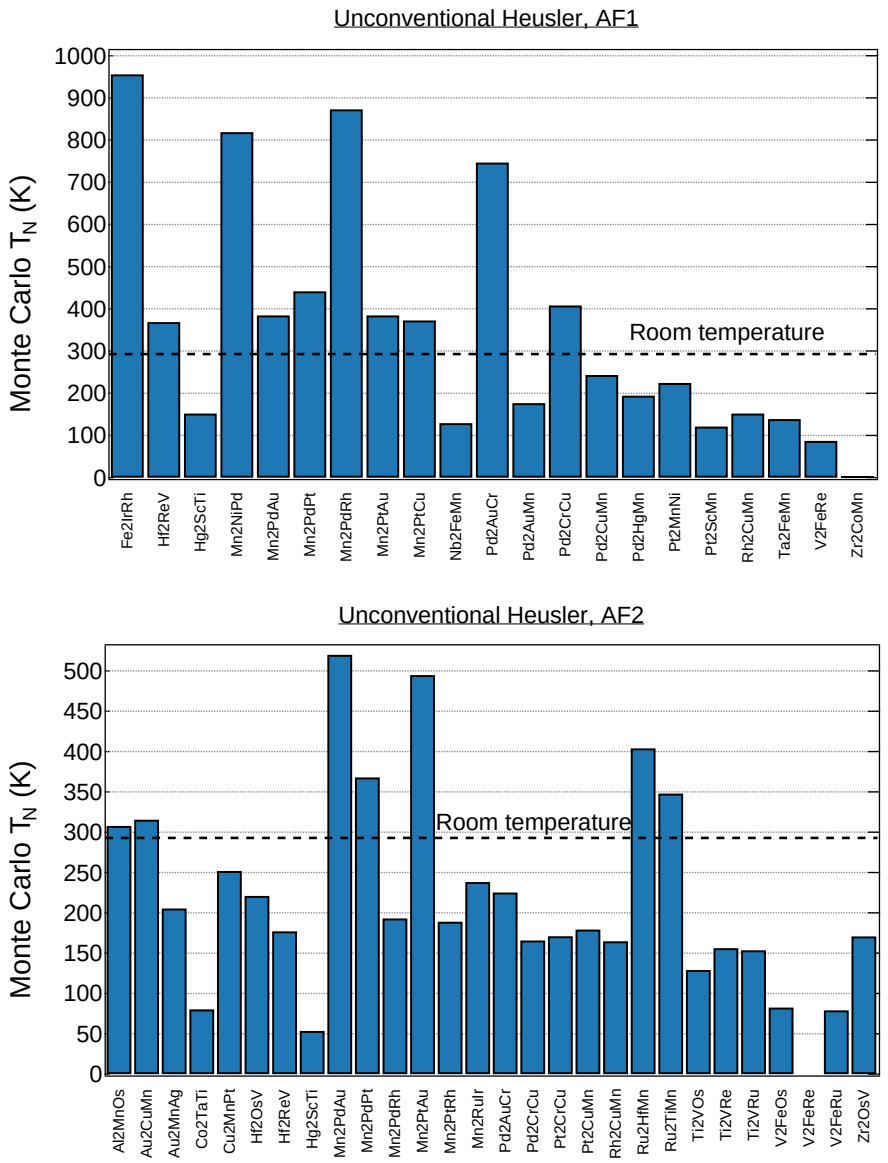

Figure C.2. | Calculated Néel temperatures for all unconventional AF Heusler compounds. The top graph shows compounds in AF1 state, the bottom one in AF2 state.

Al_2MnOs

Unconventional Heusler

Ground state: AF2

Literature: –

ΔE	=	-0.358 eV/atom
ΔE_{H}	=	71.678 meV/atom
ΔE_{AF1}	=	1.389 meV/f.u.
ΔE_{AF2}	=	-21.436 meV/f.u.

	FM	AF1	AF2
a	6.004	—	6.004
c/a	1.00	—	1.00
m_{X}	0.0	—	0.0
m_{Y}	2.6	—	2.6
m_{Z}	0.0	—	0.0
m_{tot}	2.7	—	2.6
$T_{\mathrm{N}}^{\mathrm{MF}}$		—	191
$T_{\mathrm{N}}^{\mathrm{MC}}$		—	308
ζ		—	0.95

Au_2CuMn

Unconventional Heusler

Ground state: AF2

Literature: AF [184]

ΔE	=	-0.053 eV/atom
ΔE_{H}	=	30.840 meV/atom
ΔE_{AF1}	=	39.811 meV/f.u.
ΔE_{AF2}	=	-3.248 meV/f.u.

	FM	AF1	AF2
a	6.317	—	6.319
c/a	1.00	—	1.00
m_{X}	0.0	—	0.0
m_{Y}	0.0	—	0.0
m_{Z}	3.9	—	3.9
m_{tot}	4.0	—	4.0
$T_{\mathrm{N}}^{\mathrm{MF}}$		—	346
$T_{\mathrm{N}}^{\mathrm{MC}}$		—	316
ζ		—	1.00 *

Au_2MnAg

Unconventional Heusler

Ground state: AF2

Literature: –

ΔE	=	-0.022 eV/atom
ΔE_{H}	=	63.340 meV/atom
ΔE_{AF1}	=	44.820 meV/f.u.
ΔE_{AF2}	=	-9.584 meV/f.u.

	FM	AF1	AF2
a	6.527	—	6.523
c/a	1.00	—	1.00
m_{X}	0.0	—	0.0
m_{Y}	4.0	—	4.0
m_{Z}	0.1	—	0.0
m_{tot}	4.2	—	4.1
$T_{\mathrm{N}}^{\mathrm{MF}}$		—	217
$T_{\mathrm{N}}^{\mathrm{MC}}$		—	205
ζ		—	0.65

Co_2TaTi

Unconventional Heusler

Ground state: AF2

Literature: –

ΔE	=	-0.237 eV/atom
ΔE_{H}	=	79.804 meV/atom
ΔE_{AF1}	=	23.036 meV/f.u.
ΔE_{AF2}	=	-31.422 meV/f.u.

	FM	AF1	AF2
a	6.058	—	6.055
c/a	1.00	—	1.00
m_{X}	1.1	—	0.9
m_{Y}	0.1	—	0.0
m_{Z}	0.2	—	0.0
m_{tot}	2.4	—	1.8
$T_{\mathrm{N}}^{\mathrm{MF}}$		—	91
$T_{\mathrm{N}}^{\mathrm{MC}}$		—	80
ζ		—	0.63

Cu_2MnPt

Unconventional Heusler

Ground state: AF2

Literature: –

ΔE	=	-0.105 eV/atom
ΔE_{H}	=	54.180 meV/atom
ΔE_{AF1}	=	15.463 meV/f.u.
ΔE_{AF2}	=	-33.991 meV/f.u.

	FM	AF1	AF2
a	6.004	—	5.998
c/a	1.00	—	1.00
m_{X}	0.1	—	0.0
m_{Y}	3.8	—	3.8
m_{Z}	0.0	—	0.0
m_{tot}	4.0	—	3.8
$T_{\mathrm{N}}^{\mathrm{MF}}$		—	196
$T_{\mathrm{N}}^{\mathrm{MC}}$		—	252
ζ		—	0.63

Fe_2CrSi

Conventional Heusler

Ground state: AF1

Literature: unstable [185]

ΔE	=	-0.254 eV/atom
ΔE_{H}	=	76.114 meV/atom
ΔE_{AF1}	=	-14.719 meV/f.u.
ΔE_{AF2}	=	193.607 meV/f.u.

	FM	AF1	AF2
a	5.586	5.586	—
c/a	1.00	1.00	—
m_{X}	0.3	0.1	—
m_{Y}	1.5	1.8	—
m_{Z}	0.0	0.0	—
m_{tot}	2.0	2.0	—
$T_{\mathrm{N}}^{\mathrm{MF}}$		110	—
$T_{\mathrm{N}}^{\mathrm{MC}}$		66	—
ζ		0.53	—

Fe_2IrRh

Unconventional Heusler

Ground state: AF1

Literature: –

ΔE	=	-0.006 eV/atom
ΔE_{H}	=	53.585 meV/atom
ΔE_{AF1}	=	-182.818 meV/f.u.
ΔE_{AF2}	=	125.459 meV/f.u.

	FM	AF1	AF2
a	6.026	6.022	—
c/a	1.00	0.98	—
m_{X}	3.2	3.1	—
m_{Y}	1.0	0.0	—
m_{Z}	1.1	0.0	—
m_{tot}	8.4	6.2	—
$T_{\mathrm{N}}^{\mathrm{MF}}$		1054	—
$T_{\mathrm{N}}^{\mathrm{MC}}$		956	—
ζ		1.00 *	—

Fe_2MnGa

Conventional Heusler

Ground state: AF1

Literature: AF $<$ 250 K [186, 187]

ΔE	=	-0.076 eV/atom
ΔE_{H}	=	53.170 meV/atom
ΔE_{AF1}	=	-14.740 meV/f.u.
ΔE_{AF2}	=	-14.603 meV/f.u.
$T_{\mathrm{N}}^{\mathrm{2nn}}$	=	198 K

	FM	AF1	AF2
a	5.701	5.694	5.695
c/a	1.00	1.00	1.00
m_{X}	0.3	0.0	0.0
m_{Y}	2.5	2.4	2.4
m_{Z}	0.0	0.0	0.0
m_{tot}	3.0	2.4	2.5
$T_{\mathrm{N}}^{\mathrm{MF}}$		60	67
$T_{\mathrm{N}}^{\mathrm{MC}}$		34	15
ζ		1.00	0.95

Fe_2MnGe

Conventional Heusler

Ground state: AF2

Literature: stable [188, 189]

ΔE	=	-0.102 eV/atom
ΔE_{H}	=	14.044 meV/atom
ΔE_{AF1}	=	40.921 meV/f.u.
ΔE_{AF2}	=	-24.954 meV/f.u.

	FM	AF1	AF2
a	5.698	—	5.705
c/a	1.00	—	1.00
m_{X}	0.2	—	0.6
m_{Y}	2.7	—	2.7
m_{Z}	0.0	—	0.0
m_{tot}	3.0	—	3.9
$T_{\mathrm{N}}^{\mathrm{MF}}$		—	238
$T_{\mathrm{N}}^{\mathrm{MC}}$		—	202
ζ		—	1.00 *

Fe_2MnSi

Conventional Heusler

Ground state: AF2

Literature: AF $<$ 69 K [190]

ΔE	=	-0.331 eV/atom
ΔE_{H}	=	6.049 meV/atom
ΔE_{AF1}	=	80.038 meV/f.u.
ΔE_{AF2}	=	-21.520 meV/f.u.

	FM	AF1	AF2
a	5.583	—	5.585
c/a	1.00	—	1.00
m_{X}	0.2	—	0.5
m_{Y}	2.6	—	2.6
m_{Z}	0.0	—	0.0
m_{tot}	3.0	—	3.6
$T_{\mathrm{N}}^{\mathrm{MF}}$		—	258
$T_{\mathrm{N}}^{\mathrm{MC}}$		—	210
ζ		—	1.00 *

Fe_2NbGe

Conventional Heusler

Ground state: AF1

Literature: –

ΔE	=	-0.196 eV/atom
ΔE_{H}	=	15.666 meV/atom
ΔE_{AF1}	=	-81.563 meV/f.u.
ΔE_{AF2}	=	73.405 meV/f.u.

	FM	AF1	AF2
a	5.926	6.032	—
c/a	1.00	0.96	—
m_{X}	0.6	0.8	—
m_{Y}	0.2	0.0	—
m_{Z}	0.0	0.0	—
m_{tot}	1.4	1.7	—
$T_{\mathrm{N}}^{\mathrm{MF}}$		371	—
$T_{\mathrm{N}}^{\mathrm{MC}}$		310	—
ζ		1.00 *	—

Fe_2NbSn

Conventional Heusler

Ground state: AF1

Literature: –

ΔE	=	-0.071 eV/atom
ΔE_{H}	=	43.642 meV/atom
ΔE_{AF1}	=	-130.093 meV/f.u.
ΔE_{AF2}	=	49.362 meV/f.u.

	FM	AF1	AF2
a	6.140	6.230	—
c/a	1.00	0.98	—
m_{X}	0.7	1.4	—
m_{Y}	0.2	0.0	—
m_{Z}	0.0	0.0	—
m_{tot}	1.6	2.8	—
$T_{\mathrm{N}}^{\mathrm{MF}}$		427	—
$T_{\mathrm{N}}^{\mathrm{MC}}$		355	—
ζ		1.00 *	—

Fe_2TaSi

Conventional Heusler

Ground state: AF1

Literature: –

ΔE	=	-0.409 eV/atom
ΔE_{H}	=	71.371 meV/atom
ΔE_{AF1}	=	-35.021 meV/f.u.
ΔE_{AF2}	=	92.435 meV/f.u.

	FM	AF1	AF2
a	5.840	5.922	—
c/a	1.00	0.96	—
m_{X}	0.6	0.9	—
m_{Y}	0.1	0.0	—
m_{Z}	0.0	0.0	—
m_{tot}	1.4	1.8	—
$T_{\mathrm{N}}^{\mathrm{MF}}$		315	—
$T_{\mathrm{N}}^{\mathrm{MC}}$		252	—
ζ		1.00 *	—

Fe_2TaSn

Conventional Heusler

Ground state: AF1

Literature: –

ΔE	=	-0.094 eV/atom
ΔE_{H}	=	67.838 meV/atom
ΔE_{AF1}	=	-96.254 meV/f.u.
ΔE_{AF2}	=	70.950 meV/f.u.

	FM	AF1	AF2
a	6.136	6.229	—
c/a	1.00	0.97	—
m_{X}	0.4	1.2	—
m_{Y}	0.7	0.0	—
m_{Z}	0.2	0.0	—
m_{tot}	1.5	2.5	—
$T_{\mathrm{N}}^{\mathrm{MF}}$		407	—
$T_{\mathrm{N}}^{\mathrm{MC}}$		338	—
ζ		1.00 *	—

Fe_2TiSb

Conventional Heusler

Ground state: AF1

Literature: $Fe_{1.5}TiSb$ ground state [158]

ΔE	=	-0.306 eV/atom
ΔE_{H}	=	14.166 meV/atom
ΔE_{AF1}	=	-58.982 meV/f.u.
ΔE_{AF2}	=	79.342 meV/f.u.

	FM	AF1	AF2
a	6.035	6.129	—
c/a	1.00	0.97	—
m_{X}	0.7	1.1	—
m_{Y}	0.2	0.0	—
m_{Z}	0.0	0.0	—
m_{tot}	1.7	2.2	—
$T_{\mathrm{N}}^{\mathrm{MF}}$		338	—
$T_{\mathrm{N}}^{\mathrm{MC}}$		277	—
ζ		1.00 *	—

Fe_2VGe

Conventional Heusler

Ground state: AF1

Literature: –

ΔE	=	-0.236 eV/atom
ΔE_{H}	=	0.000 meV/atom
ΔE_{AF1}	=	-44.959 meV/f.u.
ΔE_{AF2}	=	47.256 meV/f.u.

	FM	AF1	AF2
a	5.727	5.814	—
c/a	1.00	0.96	—
m_{X}	0.5	0.8	—
m_{Y}	0.2	0.0	—
m_{Z}	0.0	0.0	—
m_{tot}	1.3	1.6	—
$T_{\mathrm{N}}^{\mathrm{MF}}$		294	—
$T_{\mathrm{N}}^{\mathrm{MC}}$		252	—
ζ		1.00 *	—

Hf_2VOs

Unconventional Heusler

Ground state: AF2

Literature: –

ΔE	=	-0.327 eV/atom
ΔE_{H}	=	32.298 meV/atom
ΔE_{AF1}	=	22.488 meV/f.u.
ΔE_{AF2}	=	-63.766 meV/f.u.

	FM	AF1	AF2
a	6.573	—	6.573
c/a	1.00	—	1.00
m_{X}	0.1	—	0.0
m_{Y}	0.0	—	0.0
m_{Z}	0.1	—	2.0
m_{tot}	0.4	—	2.1
$T_{\mathrm{N}}^{\mathrm{MF}}$		—	288
$T_{\mathrm{N}}^{\mathrm{MC}}$		—	221
ζ		—	1.00 *

Hf_2ReV

Unconventional Heusler

Ground state: AF2

Literature: –

ΔE	=	-0.156 eV/atom
ΔE_{H}	=	71.729 meV/atom
ΔE_{AF1}	=	-8.049 meV/f.u.
ΔE_{AF2}	=	-64.440 meV/f.u.
$T_{\mathrm{N}}^{\mathrm{2nn}}$	=	545 K

	FM	AF1	AF2
a	6.615	6.615	6.605
c/a	1.00	1.00	1.00
m_{X}	0.2	0.0	0.0
m_{Y}	0.0	0.1	0.0
m_{Z}	2.1	2.0	2.1
m_{tot}	2.5	2.1	2.1
$T_{\mathrm{N}}^{\mathrm{MF}}$		19	199
$T_{\mathrm{N}}^{\mathrm{MC}}$		369	177
ζ		0.53	0.70

Hg_2ScTi

Unconventional Heusler

Ground state: AF1

Literature: –

ΔE	=	-0.182 eV/atom
ΔE_{H}	=	78.002 meV/atom
ΔE_{AF1}	=	-18.250 meV/f.u.
ΔE_{AF2}	=	-1.745 meV/f.u.
$T_{\mathrm{N}}^{\mathrm{2nn}}$	=	119 K

	FM	AF1	AF2
a	6.900	6.900	6.900
c/a	1.00	1.00	1.00
m_{X}	0.0	0.0	0.0
m_{Y}	0.2	0.0	0.0
m_{Z}	0.8	1.1	1.1
m_{tot}	1.0	1.1	1.1
$T_{\mathrm{N}}^{\mathrm{MF}}$		117	58
$T_{\mathrm{N}}^{\mathrm{MC}}$		152	54
ζ		0.64	1.00 *

Ir_2MnAl

Conventional Heusler

Ground state: AF2

Literature: $T_{\mathrm{N}} = 500\,\mathrm{K}$ [150]

ΔE	=	-0.579 eV/atom
ΔE_{H}	=	0.000 meV/atom
ΔE_{AF1}	=	47.172 meV/f.u.
ΔE_{AF2}	=	-9.504 meV/f.u.

	FM	AF1	AF2
a	6.061	—	6.061
c/a	1.00	—	1.00
m_{X}	0.3	—	0.1
m_{Y}	3.4	—	3.5
m_{Z}	0.0	—	0.0
m_{tot}	3.9	—	3.7
$T_{\mathrm{N}}^{\mathrm{MF}}$		—	250
$T_{\mathrm{N}}^{\mathrm{MC}}$		—	192
ζ		—	1.00 *

Ir_2MnGa

Conventional Heusler

Ground state: AF2

Literature: $T_N = 65\,K$ [151]

ΔE	=	-0.346 eV/atom
ΔE_H	=	0.000 meV/atom
ΔE_{AF1}	=	41.016 meV/f.u.
ΔE_{AF2}	=	-5.281 meV/f.u.

	FM	AF1	AF2
a	6.090	—	6.090
c/a	1.00	—	1.00
m_X	0.3	—	0.0
m_Y	3.4	—	3.5
m_Z	0.0	—	0.1
m_{tot}	3.9	—	3.7
T_N^{MF}		—	245
T_N^{MC}		—	190
ζ		—	1.00 *

Mn_2NiPd

Unconventional Heusler

Ground state: AF1

Literature: –

ΔE	=	-0.069 eV/atom
ΔE_H	=	70.981 meV/atom
ΔE_{AF1}	=	-87.340 meV/f.u.
ΔE_{AF2}	=	18.794 meV/f.u.

	FM	AF1	AF2
a	6.071	6.293	—
c/a	1.00	0.87	—
m_X	3.8	3.6	—
m_Y	0.8	0.0	—
m_Z	0.4	0.0	—
m_{tot}	8.7	7.3	—
T_N^{MF}		566	—
T_N^{MC}		819	—
ζ		0.83	—

Mn_2PdAu

Unconventional Heusler

Ground state: AF1

Literature: –

ΔE	=	-0.103 eV/atom
ΔE_{H}	=	39.803 meV/atom
ΔE_{AF1}	=	-146.848 meV/f.u.
ΔE_{AF2}	=	-52.745 meV/f.u.
$T_{\mathrm{N}}^{\mathrm{2nn}}$	=	1260 K

	FM	AF1	AF2
a	6.338	6.336	6.335
c/a	1.00	1.00	1.00
m_{X}	3.9	3.9	4.0
m_{Y}	0.3	0.0	0.1
m_{Z}	0.1	0.0	0.0
m_{tot}	8.2	7.8	8.0
$T_{\mathrm{N}}^{\mathrm{MF}}$		423	361
$T_{\mathrm{N}}^{\mathrm{MC}}$		385	520
ζ		1.00 *	1.00

Mn_2PdPt

Unconventional Heusler

Ground state: AF1

Literature: –

ΔE	=	-0.288 eV/atom
ΔE_{H}	=	0.000 meV/atom
ΔE_{AF1}	=	-214.584 meV/f.u.
ΔE_{AF2}	=	-90.451 meV/f.u.
$T_{\mathrm{N}}^{\mathrm{2nn}}$	=	1945 K

	FM	AF1	AF2
a	6.240	6.438	6.234
c/a	1.00	0.90	1.00
m_{X}	3.9	3.8	3.9
m_{Y}	0.3	0.0	0.1
m_{Z}	0.4	0.0	0.0
m_{tot}	8.5	7.6	7.9
$T_{\mathrm{N}}^{\mathrm{MF}}$		537	409
$T_{\mathrm{N}}^{\mathrm{MC}}$		442	368
ζ		0.63	0.70

Mn_2PdRh

Unconventional Heusler

Ground state: AF2

Literature: –

ΔE	=	-0.189 eV/atom
ΔE_{H}	=	6.010 meV/atom
ΔE_{AF1}	=	-0.602 meV/f.u.
ΔE_{AF2}	=	-98.303 meV/f.u.
$T_{\mathrm{N}}^{\mathrm{2nn}}$	=	764 K

	FM	AF1	AF2
a	6.168	6.169	6.160
c/a	1.00	1.00	1.00
m_{X}	3.8	3.8	3.8
m_{Y}	0.4	0.0	0.1
m_{Z}	0.7	0.0	0.0
m_{tot}	8.8	7.7	7.7
$T_{\mathrm{N}}^{\mathrm{MF}}$		288	202
$T_{\mathrm{N}}^{\mathrm{MC}}$		873	193
ζ		0.63	0.55

Mn_2PtAu

Unconventional Heusler

Ground state: AF1

Literature: –

ΔE	=	-0.163 eV/atom
ΔE_{H}	=	34.875 meV/atom
ΔE_{AF1}	=	-239.439 meV/f.u.
ΔE_{AF2}	=	-27.804 meV/f.u.
$T_{\mathrm{N}}^{\mathrm{2nn}}$	=	1604 K

	FM	AF1	AF2
a	6.338	6.357	6.332
c/a	1.00	0.97	1.00
m_{X}	3.9	3.8	3.9
m_{Y}	0.3	0.0	0.2
m_{Z}	0.1	0.0	0.0
m_{tot}	8.2	7.7	8.0
$T_{\mathrm{N}}^{\mathrm{MF}}$		530	389
$T_{\mathrm{N}}^{\mathrm{MC}}$		462	495
ζ		1.00 *	1.00

Mn_2PtCu

Unconventional Heusler

Ground state: AF1

Literature: –

ΔE = -0.113 eV/atom

ΔE_{H} = 53.198 meV/atom

ΔE_{AF1} = -200.012 meV/f.u.

ΔE_{AF2} = 27.639 meV/f.u.

	FM	AF1	AF2
a	6.131	6.138	—
c/a	1.00	0.98	—
m_{X}	3.8	3.7	—
m_{Y}	0.3	0.0	—
m_{Z}	0.1	0.0	—
m_{tot}	8.0	7.4	—
$T_{\mathrm{N}}^{\mathrm{MF}}$		465	—
$T_{\mathrm{N}}^{\mathrm{MC}}$		373	—
ζ		1.00 *	—

Mn_2PtRh

Unconventional Heusler

Ground state: AF2

Literature: –

ΔE = -0.291 eV/atom

ΔE_{H} = 0.000 meV/atom

ΔE_{AF1} = 66.829 meV/f.u.

ΔE_{AF2} = -28.251 meV/f.u.

	FM	AF1	AF2
a	6.164	—	6.157
c/a	1.00	—	1.00
m_{X}	3.8	—	3.8
m_{Y}	0.5	—	0.1
m_{Z}	0.8	—	0.0
m_{tot}	8.8	—	7.6
$T_{\mathrm{N}}^{\mathrm{MF}}$		—	248
$T_{\mathrm{N}}^{\mathrm{MC}}$		—	189
ζ		—	0.50

Mn_2RuIr

Unconventional Heusler

Ground state: AF2

Literature: –

ΔE	=	-0.084 eV/atom
ΔE_{H}	=	47.376 meV/atom
ΔE_{AF1}	=	255.524 meV/f.u.
ΔE_{AF2}	=	-53.743 meV/f.u.

	FM	AF1	AF2
a	6.033	—	6.028
c/a	1.00	—	1.00
m_{X}	3.3	—	3.2
m_{Y}	0.1	—	0.2
m_{Z}	0.2	—	0.0
m_{tot}	6.8	—	6.6
$T_{\mathrm{N}}^{\mathrm{MF}}$		—	249
$T_{\mathrm{N}}^{\mathrm{MC}}$		—	238
ζ		—	0.50

Nb_2FeMn

Unconventional Heusler

Ground state: AF1

Literature: –

ΔE	=	-0.081 eV/atom
ΔE_{H}	=	52.788 meV/atom
ΔE_{AF1}	=	-3.995 meV/f.u.
ΔE_{AF2}	=	44.371 meV/f.u.

	FM	AF1	AF2
a	6.122	6.122	—
c/a	1.00	1.00	—
m_{X}	0.1	0.0	—
m_{Y}	1.2	1.2	—
m_{Z}	0.2	0.0	—
m_{tot}	1.7	1.2	—
$T_{\mathrm{N}}^{\mathrm{MF}}$		152	—
$T_{\mathrm{N}}^{\mathrm{MC}}$		129	—
ζ		1.00 *	—

Os_2MnSi

Conventional Heusler

Ground state: AF2

Literature: –

ΔE	=	-0.225 eV/atom
ΔE_{H}	=	18.163 meV/atom
ΔE_{AF1}	=	62.443 meV/f.u.
ΔE_{AF2}	=	-32.491 meV/f.u.

	FM	AF1	AF2
a	5.947	—	5.948
c/a	1.00	—	1.00
m_{X}	0.0	—	0.1
m_{Y}	2.9	—	2.9
m_{Z}	0.0	—	0.0
m_{tot}	2.9	—	3.0
$T_{\mathrm{N}}^{\mathrm{MF}}$		—	373
$T_{\mathrm{N}}^{\mathrm{MC}}$		—	396
ζ		—	0.60

Pd_2AuCr

Unconventional Heusler

Ground state: AF2

Literature: –

ΔE	=	-0.010 eV/atom
ΔE_{H}	=	65.246 meV/atom
ΔE_{AF1}	=	-46.140 meV/f.u.
ΔE_{AF2}	=	-75.681 meV/f.u.
$T_{\mathrm{N}}^{\mathrm{2nn}}$	=	853 K

	FM	AF1	AF2
a	6.355	6.354	6.354
c/a	1.00	1.00	1.00
m_{X}	0.1	0.0	0.0
m_{Y}	0.0	0.0	0.0
m_{Z}	3.4	0.0	3.4
m_{tot}	3.5	0.1	3.4
$T_{\mathrm{N}}^{\mathrm{MF}}$		10	196
$T_{\mathrm{N}}^{\mathrm{MC}}$		747	225
ζ		0.60	0.63

Pd_2AuMn

Unconventional Heusler

Ground state: AF1

Literature: –

ΔE	=	-0.197 eV/atom
ΔE_{H}	=	0.000 meV/atom
ΔE_{AF1}	=	-7.283 meV/f.u.
ΔE_{AF2}	=	9.275 meV/f.u.

	FM	AF1	AF2
a	6.356	6.352	—
c/a	1.00	1.00	—
m_{X}	0.2	0.0	—
m_{Y}	0.0	0.0	—
m_{Z}	4.1	0.0	—
m_{tot}	4.4	0.0	—
$T_{\mathrm{N}}^{\mathrm{MF}}$		27	—
$T_{\mathrm{N}}^{\mathrm{MC}}$		177	—
ζ		0.63	—

Pd_2CrCu

Unconventional Heusler

Ground state: AF2

Literature: –

ΔE	=	-0.028 eV/atom
ΔE_{H}	=	61.434 meV/atom
ΔE_{AF1}	=	-58.403 meV/f.u.
ΔE_{AF2}	=	-65.991 meV/f.u.
$T_{\mathrm{N}}^{\mathrm{2nn}}$	=	849 K

	FM	AF1	AF2
a	6.133	6.132	6.135
c/a	1.00	1.00	1.00
m_{X}	0.1	0.0	0.0
m_{Y}	3.2	3.2	3.3
m_{Z}	0.0	0.0	0.0
m_{tot}	3.4	3.3	3.3
$T_{\mathrm{N}}^{\mathrm{MF}}$		80	98
$T_{\mathrm{N}}^{\mathrm{MC}}$		408	166
ζ		0.95	0.63

Pd_2CuMn

Unconventional Heusler

Ground state: AF1

Literature: –

ΔE = -0.223 eV/atom

ΔE_{H} = 0.000 meV/atom

ΔE_{AF1} = -0.499 meV/f.u.

ΔE_{AF2} = 3.581 meV/f.u.

	FM	AF1	AF2
a	6.132	6.125	—
c/a	1.00	1.00	—
m_{X}	0.2	0.0	—
m_{Y}	0.0	0.0	—
m_{Z}	3.9	0.0	—
m_{tot}	4.4	0.0	—
$T_{\mathrm{N}}^{\mathrm{MF}}$		7	—
$T_{\mathrm{N}}^{\mathrm{MC}}$		244	—
ζ		0.63	—

Pd_2HgMn

Unconventional Heusler

Ground state: AF1

Literature: –

ΔE = -0.167 eV/atom

ΔE_{H} = 40.199 meV/atom

ΔE_{AF1} = -22.238 meV/f.u.

ΔE_{AF2} = 6.225 meV/f.u.

	FM	AF1	AF2
a	6.438	6.434	—
c/a	1.00	1.00	—
m_{X}	0.1	0.0	—
m_{Y}	0.0	0.1	—
m_{Z}	4.0	0.0	—
m_{tot}	4.3	0.1	—
$T_{\mathrm{N}}^{\mathrm{MF}}$		204	—
$T_{\mathrm{N}}^{\mathrm{MC}}$		194	—
ζ		1.00 *	—

Pt_2CrCu

Unconventional Heusler

Ground state: AF2

Literature: –

ΔE = -0.144 eV/atom

ΔE_{H} = 54.577 meV/atom

ΔE_{AF1} = 2.409 meV/f.u.

ΔE_{AF2} = -8.472 meV/f.u.

	FM	AF1	AF2
a	6.114	—	6.114
c/a	1.00	—	1.00
m_{X}	0.2	—	0.0
m_{Y}	2.8	—	2.9
m_{Z}	0.0	—	0.0
m_{tot}	3.1	—	2.9
$T_{\mathrm{N}}^{\mathrm{MF}}$		—	34
$T_{\mathrm{N}}^{\mathrm{MC}}$		—	171
ζ		—	0.63

Pt_2CuMn

Unconventional Heusler

Ground state: AF2

Literature: FM (ab initio) [191]

ΔE = -0.282 eV/atom

ΔE_{H} = 7.962 meV/atom

ΔE_{AF1} = 2.686 meV/f.u.

ΔE_{AF2} = -20.551 meV/f.u.

	FM	AF1	AF2
a	6.124	—	6.115
c/a	1.00	—	1.00
m_{X}	0.2	—	0.1
m_{Y}	0.0	—	0.0
m_{Z}	3.7	—	3.7
m_{tot}	4.2	—	3.8
$T_{\mathrm{N}}^{\mathrm{MF}}$		—	48
$T_{\mathrm{N}}^{\mathrm{MC}}$		—	179
ζ		—	0.51

Pt_2MnNi

Unconventional Heusler

Ground state: AF1

Literature: –

ΔE	=	-0.206 eV/atom
ΔE_{H}	=	74.878 meV/atom
ΔE_{AF1}	=	-35.227 meV/f.u.
ΔE_{AF2}	=	24.870 meV/f.u.

	FM	AF1	AF2
a	6.083	6.089	—
c/a	1.00	1.00	—
m_{X}	0.1	0.0	—
m_{Y}	3.6	3.6	—
m_{Z}	0.7	0.0	—
m_{tot}	4.5	3.6	—
$T_{\mathrm{N}}^{\mathrm{MF}}$		278	—
$T_{\mathrm{N}}^{\mathrm{MC}}$		224	—
ζ		1.00 *	—

Pt_2ScMn

Unconventional Heusler

Ground state: AF1

Literature: –

ΔE	=	-0.805 eV/atom
ΔE_{H}	=	52.358 meV/atom
ΔE_{AF1}	=	-8.086 meV/f.u.
ΔE_{AF2}	=	27.422 meV/f.u.

	FM	AF1	AF2
a	6.428	6.428	—
c/a	1.00	1.00	—
m_{X}	0.2	0.0	—
m_{Y}	0.0	0.1	—
m_{Z}	4.0	0.0	—
m_{tot}	4.3	0.1	—
$T_{\mathrm{N}}^{\mathrm{MF}}$		112	—
$T_{\mathrm{N}}^{\mathrm{MC}}$		121	—
ζ		0.64	—

Rh_2CrAl

Conventional Heusler

Ground state: AF2

Literature: –

ΔE	=	-0.542 eV/atom
ΔE_{H}	=	50.899 meV/atom
ΔE_{AF1}	=	-2.097 meV/f.u.
ΔE_{AF2}	=	-30.036 meV/f.u.
$T_{\mathrm{N}}^{\mathrm{2nn}}$	=	245 K

	FM	AF1	AF2
a	6.040	6.044	6.040
c/a	1.00	1.00	1.00
m_{X}	0.2	0.0	0.0
m_{Y}	2.6	2.7	2.8
m_{Z}	0.0	0.0	0.0
m_{tot}	3.0	2.7	2.8
$T_{\mathrm{N}}^{\mathrm{MF}}$		4	117
$T_{\mathrm{N}}^{\mathrm{MC}}$		108	87
ζ		0.52	0.51

Rh_2CrIn

Conventional Heusler

Ground state: AF2

Literature: –

ΔE	=	-0.189 eV/atom
ΔE_{H}	=	73.282 meV/atom
ΔE_{AF1}	=	-5.090 meV/f.u.
ΔE_{AF2}	=	-39.892 meV/f.u.
$T_{\mathrm{N}}^{\mathrm{2nn}}$	=	338 K

	FM	AF1	AF2
a	6.282	6.287	6.282
c/a	1.00	1.00	1.00
m_{X}	0.1	0.0	0.0
m_{Y}	2.8	2.9	3.0
m_{Z}	0.0	0.0	0.0
m_{tot}	3.0	3.0	3.0
$T_{\mathrm{N}}^{\mathrm{MF}}$		2	117
$T_{\mathrm{N}}^{\mathrm{MC}}$		178	109
ζ		0.98	0.55

Rh_2CuMn

Unconventional Heusler

Ground state: AF2

Literature: –

ΔE	=	-0.053 eV/atom
ΔE_{H}	=	57.035 meV/atom
ΔE_{AF1}	=	-44.019 meV/f.u.
ΔE_{AF2}	=	-90.939 meV/f.u.
$T_{\mathrm{N}}^{\mathrm{2nn}}$	=	959 K

	FM	AF1	AF2
a	5.980	5.980	5.979
c/a	1.00	1.00	1.00
m_{X}	0.2	0.0	0.0
m_{Y}	0.1	0.1	0.0
m_{Z}	3.1	0.0	3.2
m_{tot}	3.6	0.1	3.3
$T_{\mathrm{N}}^{\mathrm{MF}}$		6	144
$T_{\mathrm{N}}^{\mathrm{MC}}$		152	165
ζ		0.51	0.65

Rh_2MnAl

Conventional Heusler

Ground state: AF2

Literature: stable [152], FM (ab initio) [192], AF $<$ 26 K [150]

ΔE	=	-0.693 eV/atom
ΔE_{H}	=	0.356 meV/atom
ΔE_{AF1}	=	35.343 meV/f.u.
ΔE_{AF2}	=	-13.690 meV/f.u.

	FM	AF1	AF2
a	6.030	—	6.034
c/a	1.00	—	1.00
m_{X}	0.3	—	0.1
m_{Y}	3.4	—	3.6
m_{Z}	0.0	—	0.0
m_{tot}	4.1	—	3.8
$T_{\mathrm{N}}^{\mathrm{MF}}$		—	240
$T_{\mathrm{N}}^{\mathrm{MC}}$		—	168
ζ		—	1.00 *

Rh_2MnGa

Conventional Heusler

Ground state: AF2

Literature: stable [152]

ΔE	=	-0.542 eV/atom
ΔE_{H}	=	0.000 meV/atom
ΔE_{AF1}	=	27.515 meV/f.u.
ΔE_{AF2}	=	-8.975 meV/f.u.

	FM	AF1	AF2
a	6.060	—	6.067
c/a	1.00	—	1.00
m_{X}	0.3	—	0.1
m_{Y}	3.5	—	3.6
m_{Z}	0.0	—	0.0
m_{tot}	4.1	—	3.8
$T_{\mathrm{N}}^{\mathrm{MF}}$		—	213
$T_{\mathrm{N}}^{\mathrm{MC}}$		—	163
ζ		—	1.00 *

Rh_2MnIn

Conventional Heusler

Ground state: AF2

Literature: stable [152]

ΔE	=	-0.345 eV/atom
ΔE_{H}	=	0.000 meV/atom
ΔE_{AF1}	=	8.437 meV/f.u.
ΔE_{AF2}	=	-19.437 meV/f.u.

	FM	AF1	AF2
a	6.290	—	6.290
c/a	1.00	—	1.00
m_{X}	0.3	—	0.1
m_{Y}	3.7	—	3.8
m_{Z}	0.0	—	0.0
m_{tot}	4.4	—	3.9
$T_{\mathrm{N}}^{\mathrm{MF}}$		—	150
$T_{\mathrm{N}}^{\mathrm{MC}}$		—	103
ζ		—	1.00 *

Ru_2CrAl

Conventional Heusler

Ground state: AF1

Literature: –

ΔE = -0.357 eV/atom

ΔE_{H} = 0.000 meV/atom

ΔE_{AF1} = -14.102 meV/f.u.

ΔE_{AF2} = 8.435 meV/f.u.

	FM	AF1	AF2
a	5.974	5.968	—
c/a	1.00	1.00	—
m_{X}	0.1	0.0	—
m_{Y}	1.3	1.3	—
m_{Z}	0.0	0.0	—
m_{tot}	1.6	1.3	—
$T_{\mathrm{N}}^{\mathrm{MF}}$		91	—
$T_{\mathrm{N}}^{\mathrm{MC}}$		83	—
ζ		0.95	—

Ru_2CrGa

Conventional Heusler

Ground state: AF1

Literature: –

ΔE = -0.197 eV/atom

ΔE_{H} = 0.000 meV/atom

ΔE_{AF1} = -11.052 meV/f.u.

ΔE_{AF2} = 25.613 meV/f.u.

	FM	AF1	AF2
a	5.995	5.993	—
c/a	1.00	1.00	—
m_{X}	0.2	0.0	—
m_{Y}	1.5	1.5	—
m_{Z}	0.0	0.0	—
m_{tot}	1.8	1.5	—
$T_{\mathrm{N}}^{\mathrm{MF}}$		126	—
$T_{\mathrm{N}}^{\mathrm{MC}}$		98	—
ζ		1.00 *	—

Ru_2CrGe

Conventional Heusler

Ground state: AF2

Literature: $T_N = 13\,K$ (AF2) [153]

ΔE	=	-0.215 eV/atom
ΔE_H	=	0.000 meV/atom
ΔE_{AF1}	=	-47.633 meV/f.u.
ΔE_{AF2}	=	-57.941 meV/f.u.
T_N^{2nn}	=	725 K

	FM	AF1	AF2
a	6.011	6.011	6.011
c/a	1.00	1.00	1.00
m_X	0.2	0.0	0.1
m_Y	2.2	2.3	2.3
m_Z	0.0	0.0	0.0
m_{tot}	2.5	2.3	2.4
T_N^{MF}		7	81
T_N^{MC}		25	37
ζ		0.52	0.53

Ru_2CrSb

Conventional Heusler

Ground state: AF2

Literature: –

ΔE	=	-0.078 eV/atom
ΔE_H	=	76.429 meV/atom
ΔE_{AF1}	=	18.050 meV/f.u.
ΔE_{AF2}	=	-8.168 meV/f.u.

	FM	AF1	AF2
a	6.244	—	6.244
c/a	1.00	—	1.00
m_X	0.0	—	0.1
m_Y	2.8	—	2.9
m_Z	0.0	—	0.0
m_{tot}	2.8	—	3.1
T_N^{MF}		—	146
T_N^{MC}		—	109
ζ		—	0.62

Ru_2CrSi

Conventional Heusler

Ground state: AF2

Literature: $T_N = 14\,K$ [154]

ΔE	=	-0.413 eV/atom
ΔE_H	=	0.000 meV/atom
ΔE_{AF1}	=	-59.577 meV/f.u.
ΔE_{AF2}	=	-71.118 meV/f.u.
T_N^{2nn}	=	896 K

	FM	AF1	AF2
a	5.926	5.920	5.920
c/a	1.00	1.00	1.00
m_X	0.1	0.0	0.0
m_Y	2.1	2.2	2.2
m_Z	0.0	0.0	0.0
m_{tot}	2.4	2.2	2.3
T_N^{MF}		7	91
T_N^{MC}		34	41
ζ		0.52	0.50

Ru_2CrSn

Conventional Heusler

Ground state: AF2

Literature: Spin glass $< 7\,K$ [153]

ΔE	=	-0.080 eV/atom
ΔE_H	=	11.644 meV/atom
ΔE_{AF1}	=	-44.172 meV/f.u.
ΔE_{AF2}	=	-49.046 meV/f.u.
T_N^{2nn}	=	636 K

	FM	AF1	AF2
a	6.233	6.233	6.233
c/a	1.00	1.00	1.00
m_X	0.2	0.0	0.1
m_Y	2.4	2.4	2.4
m_Z	0.0	0.0	0.0
m_{tot}	2.8	2.4	2.6
T_N^{MF}		12	43
T_N^{MC}		29	24
ζ		0.52	0.50

Ru_2FeGa

Conventional Heusler

Ground state: AF2

Literature: AF predicted [149]

ΔE	=	-0.154 eV/atom
ΔE_{H}	=	1.550 meV/atom
ΔE_{AF1}	=	57.935 meV/f.u.
ΔE_{AF2}	=	-34.122 meV/f.u.

	FM	AF1	AF2
a	5.992	—	5.992
c/a	1.00	—	1.00
m_{X}	0.2	—	0.2
m_{Y}	2.8	—	2.8
m_{Z}	0.0	—	0.0
m_{tot}	3.1	—	3.2
$T_{\mathrm{N}}^{\mathrm{MF}}$		—	344
$T_{\mathrm{N}}^{\mathrm{MC}}$		—	308
ζ		—	1.00 *

Ru_2HfMn

Unconventional Heusler

Ground state: AF2

Literature: –

ΔE	=	-0.338 eV/atom
ΔE_{H}	=	76.930 meV/atom
ΔE_{AF1}	=	85.696 meV/f.u.
ΔE_{AF2}	=	-27.160 meV/f.u.

	FM	AF1	AF2
a	6.270	—	6.270
c/a	1.00	—	1.00
m_{X}	0.1	—	0.2
m_{Y}	0.0	—	0.0
m_{Z}	3.3	—	3.4
m_{tot}	3.5	—	3.8
$T_{\mathrm{N}}^{\mathrm{MF}}$		—	260
$T_{\mathrm{N}}^{\mathrm{MC}}$		—	409
ζ		—	0.66

Ru_2MnAl

Conventional Heusler

Ground state: AF2

Literature: stable [155]

ΔE	=	-0.406 eV/atom
ΔE_{H}	=	0.000 meV/atom
ΔE_{AF1}	=	-32.079 meV/f.u.
ΔE_{AF2}	=	-52.369 meV/f.u.
$T_{\mathrm{N}}^{\mathrm{2nn}}$	=	591 K

	FM	AF1	AF2
a	5.978	5.973	5.974
c/a	1.00	1.00	1.00
m_{X}	0.2	0.0	0.0
m_{Y}	2.5	2.5	2.6
m_{Z}	0.0	0.0	0.0
m_{tot}	3.0	2.5	2.6
$T_{\mathrm{N}}^{\mathrm{MF}}$		9	76
$T_{\mathrm{N}}^{\mathrm{MC}}$		50	37
ζ		0.51	0.53

Ru_2MnGe

Conventional Heusler

Ground state: AF2

Literature: AF [20], AF2 [21]

ΔE	=	-0.262 eV/atom
ΔE_{H}	=	0.000 meV/atom
ΔE_{AF1}	=	44.578 meV/f.u.
ΔE_{AF2}	=	-36.333 meV/f.u.

	FM	AF1	AF2
a	6.005	—	6.008
c/a	1.00	—	1.00
m_{X}	0.0	—	0.1
m_{Y}	3.0	—	3.1
m_{Z}	0.0	—	0.0
m_{tot}	3.1	—	3.2
$T_{\mathrm{N}}^{\mathrm{MF}}$		—	341
$T_{\mathrm{N}}^{\mathrm{MC}}$		—	307
ζ		—	0.55

Ru_2MnSi

Conventional Heusler

Ground state: AF2

Literature: AF [22]

ΔE	=	-0.465 eV/atom
ΔE_{H}	=	0.000 meV/atom
ΔE_{AF1}	=	48.237 meV/f.u.
ΔE_{AF2}	=	-41.516 meV/f.u.

	FM	AF1	AF2
a	5.912	—	5.914
c/a	1.00	—	1.00
m_{X}	0.0	—	0.1
m_{Y}	2.9	—	3.0
m_{Z}	0.0	—	0.0
m_{tot}	3.0	—	3.2
$T_{\mathrm{N}}^{\mathrm{MF}}$		—	370
$T_{\mathrm{N}}^{\mathrm{MC}}$		—	365
ζ		—	0.80

Ru_2TiMn

Unconventional Heusler

Ground state: AF2

Literature: –

ΔE	=	-0.337 eV/atom
ΔE_{H}	=	51.389 meV/atom
ΔE_{AF1}	=	82.907 meV/f.u.
ΔE_{AF2}	=	-16.836 meV/f.u.

	FM	AF1	AF2
a	6.081	—	6.085
c/a	1.00	—	1.00
m_{X}	0.0	—	0.2
m_{Y}	0.0	—	0.0
m_{Z}	3.1	—	3.2
m_{tot}	3.2	—	3.5
$T_{\mathrm{N}}^{\mathrm{MF}}$		—	222
$T_{\mathrm{N}}^{\mathrm{MC}}$		—	348
ζ		—	0.85

Ru_2VGe

Conventional Heusler

Ground state: AF1

Literature: stable [155], paramagnetic [156]

ΔE = -0.333 eV/atom

ΔE_{H} = 0.000 meV/atom

ΔE_{AF1} = -0.320 meV/f.u.

ΔE_{AF2} = 23.824 meV/f.u.

	FM	AF1	AF2
a	6.027	6.027	—
c/a	1.00	1.00	—
m_{X}	0.1	0.0	—
m_{Y}	1.0	1.0	—
m_{Z}	0.0	0.0	—
m_{tot}	1.2	1.0	—
$T_{\mathrm{N}}^{\mathrm{MF}}$		86	—
$T_{\mathrm{N}}^{\mathrm{MC}}$		75	—
ζ		1.00 *	—

Ru_2VSi

Conventional Heusler

Ground state: AF1

Literature: stable [155]

ΔE = -0.563 eV/atom

ΔE_{H} = 0.000 meV/atom

ΔE_{AF1} = -10.450 meV/f.u.

ΔE_{AF2} = 3.107 meV/f.u.

	FM	AF1	AF2
a	5.938	5.936	—
c/a	1.00	1.00	—
m_{X}	0.0	0.0	—
m_{Y}	0.9	0.9	—
m_{Z}	0.0	0.0	—
m_{tot}	1.0	0.9	—
$T_{\mathrm{N}}^{\mathrm{MF}}$		63	—
$T_{\mathrm{N}}^{\mathrm{MC}}$		69	—
ζ		0.55	—

Sc_2CoGa

Conventional Heusler

Ground state: AF2

Literature: –

ΔE	=	-0.458 eV/atom
ΔE_{H}	=	37.258 meV/atom
ΔE_{AF1}	=	2.891 meV/f.u.
ΔE_{AF2}	=	-30.770 meV/f.u.

	FM	AF1	AF2
a	6.496	—	6.496
c/a	1.00	—	1.00
m_{X}	0.1	—	0.0
m_{Y}	0.6	—	1.0
m_{Z}	0.0	—	0.0
m_{tot}	0.7	—	1.1
$T_{\mathrm{N}}^{\mathrm{MF}}$		—	101
$T_{\mathrm{N}}^{\mathrm{MC}}$		—	82
ζ		—	0.65

Ta_2FeMn

Unconventional Heusler

Ground state: AF1

Literature: –

ΔE	=	-0.192 eV/atom
ΔE_{H}	=	37.028 meV/atom
ΔE_{AF1}	=	-0.572 meV/f.u.
ΔE_{AF2}	=	0.226 meV/f.u.

	FM	AF1	AF2
a	6.123	6.123	—
c/a	1.00	1.00	—
m_{X}	0.1	0.0	—
m_{Y}	1.0	1.1	—
m_{Z}	0.2	0.0	—
m_{tot}	1.4	1.1	—
$T_{\mathrm{N}}^{\mathrm{MF}}$		165	—
$T_{\mathrm{N}}^{\mathrm{MC}}$		139	—
ζ		1.00 *	—

Ti_2VOs

Unconventional Heusler

Ground state: AF2

Literature: –

ΔE	=	-0.354 eV/atom
ΔE_{H}	=	37.604 meV/atom
ΔE_{AF1}	=	0.596 meV/f.u.
ΔE_{AF2}	=	-70.619 meV/f.u.

	FM	AF1	AF2
a	6.220	—	6.222
c/a	1.00	—	1.00
m_{X}	0.1	—	0.0
m_{Y}	1.5	—	1.7
m_{Z}	0.0	—	0.0
m_{tot}	1.7	—	1.8
$T_{\mathrm{N}}^{\mathrm{MF}}$		—	160
$T_{\mathrm{N}}^{\mathrm{MC}}$		—	129
ζ		—	0.55

Ti_2VRe

Unconventional Heusler

Ground state: AF2

Literature: –

ΔE	=	-0.190 eV/atom
ΔE_{H}	=	68.220 meV/atom
ΔE_{AF1}	=	7.180 meV/f.u.
ΔE_{AF2}	=	-43.920 meV/f.u.

	FM	AF1	AF2
a	6.271	—	6.266
c/a	1.00	—	1.00
m_{X}	0.2	—	0.0
m_{Y}	1.7	—	1.7
m_{Z}	0.1	—	0.0
m_{tot}	2.2	—	1.8
$T_{\mathrm{N}}^{\mathrm{MF}}$		—	187
$T_{\mathrm{N}}^{\mathrm{MC}}$		—	156
ζ		—	0.94

Ti_2VRu

Unconventional Heusler

Ground state: AF2

Literature: –

ΔE	=	-0.320 eV/atom
ΔE_{H}	=	78.886 meV/atom
ΔE_{AF1}	=	11.486 meV/f.u.
ΔE_{AF2}	=	-53.221 meV/f.u.

	FM	AF1	AF2
a	6.222	—	6.222
c/a	1.00	—	1.00
m_{X}	0.1	—	0.0
m_{Y}	1.7	—	1.7
m_{Z}	0.1	—	0.0
m_{tot}	2.1	—	1.8
$T_{\mathrm{N}}^{\mathrm{MF}}$		—	125
$T_{\mathrm{N}}^{\mathrm{MC}}$		—	154
ζ		—	0.93

V_2FeOs

Unconventional Heusler

Ground state: AF2

Literature: –

ΔE	=	-0.227 eV/atom
ΔE_{H}	=	49.788 meV/atom
ΔE_{AF1}	=	19.914 meV/f.u.
ΔE_{AF2}	=	-15.011 meV/f.u.

	FM	AF1	AF2
a	5.934	—	5.934
c/a	1.00	—	1.00
m_{X}	0.1	—	0.1
m_{Y}	1.8	—	1.8
m_{Z}	0.0	—	0.0
m_{tot}	1.9	—	2.1
$T_{\mathrm{N}}^{\mathrm{MF}}$		—	129
$T_{\mathrm{N}}^{\mathrm{MC}}$		—	83
ζ		—	0.95

V_2FeRe

Unconventional Heusler

Ground state: AF1

Literature: –

ΔE	=	-0.222 eV/atom
ΔE_{H}	=	53.779 meV/atom
ΔE_{AF1}	=	-46.240 meV/f.u.
ΔE_{AF2}	=	-16.788 meV/f.u.

	FM	AF1	AF2
a	5.927	5.937	5.934
c/a	1.00	1.00	1.00
m_{X}	0.0	0.0	0.0
m_{Y}	0.0	1.2	1.0
m_{Z}	0.0	0.0	0.0
m_{tot}	0.0	1.2	1.1
$T_{\mathrm{N}}^{\mathrm{MF}}$		83	—
$T_{\mathrm{N}}^{\mathrm{MC}}$		87	—
ζ		0.58	—

V_2FeRu

Unconventional Heusler

Ground state: AF2

Literature: –

ΔE	=	-0.179 eV/atom
ΔE_{H}	=	73.540 meV/atom
ΔE_{AF1}	=	8.829 meV/f.u.
ΔE_{AF2}	=	-15.137 meV/f.u.

	FM	AF1	AF2
a	5.913	—	5.911
c/a	1.00	—	1.00
m_{X}	0.0	—	0.1
m_{Y}	1.6	—	1.7
m_{Z}	0.1	—	0.0
m_{tot}	1.8	—	2.0
$T_{\mathrm{N}}^{\mathrm{MF}}$		—	103
$T_{\mathrm{N}}^{\mathrm{MC}}$		—	79
ζ		—	0.90

Zr_2CoMn

Unconventional Heusler

Ground state: AF1

Literature: –

ΔE	=	-0.182 eV/atom
ΔE_{H}	=	68.576 meV/atom
ΔE_{AF1}	=	-4.253 meV/f.u.
ΔE_{AF2}	=	7.139 meV/f.u.

	FM	AF1	AF2
a	6.367	6.363	—
c/a	1.00	1.00	—
m_{X}	0.1	0.0	—
m_{Y}	0.4	0.6	—
m_{Z}	0.1	0.0	—
m_{tot}	0.6	0.6	—
$T_{\mathrm{N}}^{\mathrm{MF}}$		12	—
$T_{\mathrm{N}}^{\mathrm{MC}}$		9	—
ζ		0.62	—

Zr_2OsV

Unconventional Heusler

Ground state: AF2

Literature: –

ΔE	=	-0.223 eV/atom
ΔE_{H}	=	79.701 meV/atom
ΔE_{AF1}	=	32.755 meV/f.u.
ΔE_{AF2}	=	-52.492 meV/f.u.

	FM	AF1	AF2
a	6.631	—	6.626
c/a	1.00	—	1.00
m_{X}	0.0	—	0.0
m_{Y}	0.0	—	0.0
m_{Z}	2.0	—	2.0
m_{tot}	2.2	—	2.0
$T_{\mathrm{N}}^{\mathrm{MF}}$		—	243
$T_{\mathrm{N}}^{\mathrm{MC}}$		—	171
ζ		—	1.00 *

List of Figures

List of Tables

Bibliography

[1] G. A. Prinz. Science **282**, 1660 (1998). doi:10.1126/science.282.5394.1660.

[2] J. F. Gregg, I. Petej, E. Jouguelet, and C. Dennis. J. Phys. D: Appl. Phys. **35**, R121 (2002). doi:10.1088/0022-3727/35/18/201.

[3] C. Chappert, A. Fert, and F. N. Van Dau. Nat. Mater. **6**, 813 (2007). doi:10.1038/nmat2024.

[4] V. K. Joshi. Eng. Sci. Technol. an Int. J. **19**, 1503 (2016). doi:10.1016/j.jestch.2016.05.002.

[5] S. Tehrani et al. IEEE Trans. Magn. **35**, 2814 (1999). doi:10.1109/20.800991.

[6] S. A. Wolf et al. Science **294**, 1488 (2001). doi:10.1126/science.1065389.

[7] Y. Huai. AAPPS Bull. **18**, 33 (2008).

[8] C. J. Lin et al. 45nm Low Power CMOS Logic Compatible Embedded STT MRAM Utilizing a Reverse-Connection 1T / 1MTJ Cell. in *Electron Devices Meet. (IEDM), 2009 IEEE Int.*, pages 1–4, 2009.

[9] A. V. Khvalkovskiy et al. J. Phys. D: Appl. Phys. **46**, 074001 (2013). doi:10.1088/0022-3727/46/7/074001.

[10] D. Apalkov et al. ACM J. Emerg. Technol. Comput. Syst. **9**, 1 (2013). doi:10.1145/2463585.2463589.

[11] A. Kohn et al. Sci. Rep. **3**, 2412 (2013). doi:10.1038/srep02412.

[12] M. Rickart et al. Eur. Phys. J. B **45**, 207 (2005). doi:10.1140/epjb/e2005-00051-5.

[13] J. P. Nozières et al. J. Appl. Phys. **87**, 3920 (2000). doi:10.1063/1.372435.

[14] Webelements periodic table of the elements. Iridium abundance (visited on 23/02/2017). http://www.webelements.com/iridium/.

[15] Platinum group metals. (visited on 29/11/2016). http://platinum.matthey.com.

[16] European Commission. *Report on critical raw materials for the EU - Report of the Ad hoc Working Group on defining critical raw materials*. European Commision, Brussels, Belgium, 2014.

[17] M. Ali et al. Phys. Rev. B **68**, 214420 (2003). doi:10.1103/PhysRevB.68.214420.

[18] M. Meinert, B. Büker, D. Graulich, and M. Dunz. Phys. Rev. B **92**, 144408 (2015). arXiv:1501.05162, doi:10.1103/PhysRevB.92.144408.

[19] S. Ishida, S. Kashiwagi, S. Fujii, and S. Asano. Phys. B **210**, 140 (1995). doi:10.1016/0921-4526(94)00920-Q.

[20] N. Fukatani, K. Inagaki, T. Miyawaki, K. Ueda, and H. Asano. J. Appl. Phys. **113**, 17C103 (2013). doi:10.1063/1.4794133.

[21] M. Gotoh, M. Ohashi, T. Kanomata, and Y. Yamaguchi. Phys. B **213-214**, 306 (1995). doi:10.1016/0921-4526(95)00138-Y.

[22] T. Kanomata, M. Kikuchi, and H. Yamauchi. J. Alloys Compd. **414**, 1 (2006). doi:10.1016/j.jallcom.2005.06.079.

[23] N. Yamada, H. Sakai, H. Mori, and T. Ohoyama. Phys. B **149**, 311 (1988). doi:10.1016/0378-4363(88)90258-6.

[24] H. Kurt et al. Appl. Phys. Lett. **101**, 132410 (2012). doi:10.1063/1.4754123.

[25] S. Mizukami et al. Appl. Phys. Express **6**, 123002 (2013). doi:10.7567/APEX.6.123002.

[26] W. H. Meiklejohn and C. P. Bean. Phys. Rev. **105**, 904 (1957). doi:10.1103/PhysRev.105.904.

[27] J. Nogués and I. K. Schuller. J. Magn. Magn. Mater. **192**, 203 (1999). doi:10.1016/S0304-8853(98)00266-2.

[28] W. Thomson. Proceedings of the Royal Society of London **8**, 546 (1856).

[29] M. N. Baibich et al. Phys. Rev. Lett. **61**, 2472 (1988). doi:10.1103/PhysRevLett.61.2472.

[30] G. Binasch, P. Grünberg, F. Saurenbach, and W. Zinn. Phys. Rev. B **39**, 4828 (1989). doi:10.1103/PhysRevB.39.4828.

[31] W. H. Meiklejohn. J. Appl. Phys. **33**, 1328 (1962). doi:10.1063/1.1728716.

[32] D. Paccard, C. Schlenker, O. Massenet, R. Montmory, and A. Yelon. Phys. Status Solidi **16**, 301 (1966). doi:10.1002/pssb.19660160131.

[33] S. Polisetty, S. Sahoo, and C. Binek. Phys. Rev. B **76**, 184423 (2007). doi:10.1103/PhysRevB.76.184423.

[34] J. Dho, C. W. Leung, and M. G. Blamire. J. Appl. Phys. **99**, 033910 (2006). doi:10.1063/1.2169876.

[35] J. Nogués, D. Lederman, T. Moran, and I. Schuller. Phys. Rev. Lett. **76**, 4624 (1996). doi:10.1103/PhysRevLett.76.4624.

[36] K. O 'Grady, L. E. Fernandez-Outon, and G. Vallejo-Fernandez. J. Magn. Magn. Mater. **322**, 883 (2009). doi:10.1016/j.jmmm.2009.12.011.

[37] L. Néel. Annales de Physique **2**, 61 (1967).

[38] D. Mauri, H. C. Siegmann, P. S. Bagus, and E. Kay. J. Appl. Phys. **62**, 3047 (1987). doi:10.1063/1.339367.

[39] A. P. Malozemoff. Phys. Rev. B **35**, 3679 (1987). doi:10.1103/PhysRevB.35.3679.

[40] N. Koon. Phys. Rev. Lett. **78**, 4865 (1997). doi:10.1103/PhysRevLett.78.4865.

[41] T. C. Schulthess and W. H. Butler. Phys. Rev. Lett. **81**, 4516 (1998). doi:10.1103/PhysRevLett.81.4516.

[42] T. C. Schulthess and W. H. Butler. J. Appl. Phys. **85**, 5510 (1999). doi:10.1063/1.369878.

[43] P. Miltényi et al. Phys. Rev. Lett. **84**, 4224 (2000). doi:10.1103/PhysRevLett.84.4224.

[44] U. Nowak, A. Misra, and K. D. Usadel. J. Appl. Phys. **89**, 7269 (2001). arXiv:arXiv:cond-mat/0010213v1, doi:10.1063/1.1358829.

[45] U. Nowak et al. Phys. Rev. B **66**, 014430 (2002). doi:10.1103/PhysRevB.66.014430.

[46] E. Fulcomer and S. H. Charap. J. Appl. Phys. **43**, 4184 (1972). doi:10.1063/1.1660893.

[47] E. Fulcomer and S. H. Charap. J. Appl. Phys. **43**, 4190 (1972). doi:10.1063/1.1660894.

[48] M. Julliere. Phys. Lett. A **54**, 225 (1975). doi:10.1016/0375-9601(75)90174-7.

[49] W. H. Butler, X.-G. Zhang, T. C. Schulthess, and J. M. MacLaren. Phys. Rev. B **63**, 054416 (2001). doi:10.1103/PhysRevB.63.054416.

[50] J. Mathon and A. Umerski. Phys. Rev. B **63**, 220403 (2001). doi:10.1103/PhysRevB.63.220403.

[51] M. Bowen et al. Appl. Phys. Lett. **79**, 1655 (2001). doi:10.1063/1.1404125.

[52] S. Ikeda et al. Appl. Phys. Lett. **93**, 082508 (2008). doi:10.1063/1.2976435.

[53] H. X. Liu et al. Appl. Phys. Lett. **101**, 132418 (2012). doi:10.1063/1.4755773.

[54] J. C. Slonczewski. J. Magn. Magn. Mater. **159**, L1 (1996). doi:10.1016/0304-8853(96)00062-5.

[55] L. Berger. Phys. Rev. B **54**, 9353 (1996). arXiv:1102.5325, doi:10.1103/PhysRevB.54.9353.

[56] H. B. Huang et al. J. Magn. Magn. Mater. **330**, 16 (2013). doi:10.1016/j.jmmm.2012.09.031.

[57] Everspin | The MRAM Company. http://www.everspin.com.

[58] G. E. W. Bauer, E. Saitoh, and B. J. van Wees. Nat. Mater. **11**, 391 (2012). doi:10.1038/nmat3301.

[59] C. Gould et al. Phys. Rev. Lett. **93**, 117203 (2004). arXiv:cond-mat/0407735, doi:10.1103/PhysRevLett.93.117203.

[60] B. G. Park et al. Nat. Mater. **10**, 347 (2011). doi:10.1038/nmat2983.

[61] L. Neel. Magnetism and the local molecular field. Nobel prize lecture, 1970. http://www.nobelprize.org/nobelprizes/physics/laureates/1970/neel-lecture.pdf.

[62] T. Jungwirth, X. Marti, P. Wadley, and J. Wunderlich. Nat. Nanotechnol. **11**, 231 (2016). arXiv:1509.05296v1, doi:10.1038/nnano.2016.18.

[63] P. Wadley et al. Science **351**, 587 (2016). arXiv:1503.03765, doi:10.1126/science.aab1031.

[64] S. D. Ganichev et al. Nature **417**, 153 (2002). doi:doi:10.1038/417153a.

[65] F. Heusler. Verhandlungen der Dtsch. Phys. Gesellschaft **5**, 219 (1903).

[66] T. Graf, S. S. P. Parkin, and C. Felser. IEEE Trans. Magn. **47**, 367 (2011). doi:10.1109/TMAG.2010.2096229.

[67] Y. Sakuraba et al. Jpn. J. Appl. Physics **44**, L1100 (2005). doi:10.1143/JJAP.44.L1100.

[68] M. Meinert, J.-M. Schmalhorst, E. Arenholz, and G. Reiss. J. Phys. D: Appl. Phys. **44**, 215003 (2011). doi:10.1088/0022-3727/44/21/215003.

[69] M. Meinert et al. Phys. Rev. B **90**, 085127 (2014). arXiv:1402.5755, doi:10.1103/PhysRevB.90.085127.

[70] J. Winterlik et al. Phys. Rev. B **78**, 184506 (2008). arXiv:0808.2356, doi:10.1103/PhysRevB.78.184506.

[71] R. Lahiouel et al. Z. Physik B **67**, 185 (1987). doi:10.1007/BF01303979.

[72] A. Planes, L. Mañosa, and M. Acet. J. Phys. Condens. Matter **21**, 233201 (2009). doi:10.1088/0953-8984/21/23/233201.

[73] C. Li, J. S. Lian, and Q. Jiang. Phys. Rev. B **83**, 235125 (2011). doi:10.1103/PhysRevB.83.235125.

[74] Z. Bai, L. Shen, G. Han, and Y. P. Fen. Spin **02**, 1230006 (2012). doi:10.1142/S201032471230006X.

[75] C. Sterwerf, M. Meinert, and J.-m. Schmalhorst. IEEE Trans. Magn. **49**, 4386 (2013). doi:10.1109/TMAG.2013.2238220.

[76] K. Borisov et al. Appl. Phys. Lett. **108**, 192407 (2016). doi:10.1063/1.4948934.

[77] W. Kohn. Electronic structure of matter - Wave functions and density functionals. Nobel prize lecture, 1999. http://www.nobelprize.org/nobel_prizes/chemistry/laureates/1998/kohn-lecture.pdf.

[78] W. Koch and M. C. Holthausen. *A Chemist's Guide to Density Functional Theory*, volume 3. Wiley-VCH, 2001. doi:10.1002/3527600043.

[79] K. Capelle. Braz. J. Phys. **36**, 1318 (2006). arXiv:cond-mat/0211443v5, doi:10.1590/S0103-97332006000700035.

[80] P. Hohenberg and W. Kohn. Phys. Rev. **136**, B864 (1964). doi:10.1103/PhysRev.136.B864.

[81] W. Kohn and L. J. Sham. Phys. Rev. **140**, A1133 (1965). doi:10.1103/PhysRev.140.A1133.

[82] O. Gunnarsson and B. I. Lundqvist. Phys. Rev. B **13**, 4274 (1976). doi:10.1103/PhysRevB.13.4274.

[83] U. von Barth and L. Hedin. J. Phys. C: Solid State Phys. **5**, 1629 (1972). doi:10.1088/0022-3719/5/13/012.

[84] D. M. Ceperley and B. J. Alder. Phys. Rev. Lett. **45**, 566 (1980). doi:10.1103/PhysRevLett.45.566.

[85] S. H. Vosko, L. Wilk, and M. Nusair. Can. J. Phys. **58**, 1200 (1980). doi:10.1139/p80-159.

[86] J. P. Perdew and Y. Wang. Phys. Rev. B **45**, 13244 (1992). doi:10.1103/PhysRevB.45.13244.

[87] J. P. Perdew, K. Burke, and M. Ernzerhof. Phys. Rev. Lett. **77**, 3865 (1996). doi:10.1103/PhysRevLett.77.3865.

[88] G. Kresse and J. Furthmüller. Phys. Rev. B **54**, 11169 (1996). doi:10.1103/PhysRevB.54.11169.

[89] G. Kresse and D. Joubert. Phys. Rev. B **59**, 1758 (1999). doi:10.1103/PhysRevB.59.1758.

[90] Vienna ab-initio simulation package. Version 5.3.5. http://www.vasp.at.

[91] H. Ebert, D. Ködderitzsch, and J. Minár. Rep. Prog. Phys. **74**, 096501 (2011). doi:10.1088/0034-4885/74/9/096501.

[92] The Munich SPR-KKR package. Version 5.4. http://ebert.cup.uni-muenchen.de/SPRKKR.

[93] P. E. Blöchl. Phys. Rev. B **50**, 17953 (1994). doi:10.1103/PhysRevB.50.17953.

[94] P. E. Blöchl, C. J. Först, and J. Schimpl. Bull. Mater. Sci. **26**, 33 (2003). doi:10.1007/BF02712785.

[95] C. Rostgaard. arXiv (2009). arXiv:0910.1921v2.

[96] J. Korringa. Physica **13**, 392 (1947). doi:10.1016/0031-8914(47)90013-X.

[97] W. Kohn and N. Rostoker. Phys. Rev. **94**, 1111 (1954). doi:10.1103/PhysRev.94.1111.

[98] P. Mavropoulos and N. Papanikolaou. Comput. Nanosci. Do It Yourself! **31**, 131 (2006).

[99] P. Lloyd and P. V. Smith. Adv. Phys. **21**, 69 (1972). doi:10.1080/00018737200101268.

[100] A. I. Liechtenstein, M. I. Katsnelson, V. P. Antropov, and V. A. Gubanov. J. Magn. Magn. Mater. **67**, 65 (1987). doi:10.1016/0304-8853(87)90721-9.

[101] S. Blundell. *Magnetism in condensed matter*, volume 2. Oxford University Press, 2001.

[102] L. Engelhardt and C. Schröder. Simulating computationally complex magnetic molecules. in *Molecular Cluster Magnets*, volume 3 of *World Scientific Series in Nanoscience and Nanotechnology*, chapter 6, World Scientific, 2011. doi:10.1142/9789814322959_0006.

[103] L. Engelhardt, M. Luban, and C. Schröder. Phys. Rev. B **74**, 054413 (2006). doi:10.1103/PhysRevB.74.054413.

[104] A. R. Machintosh and O. K. Andersen. The electronic structure of transition metals. in *Electrons at the Fermi Surface*, edited by M. Springford, chapter 5, pages 149–224, Cambridge University Press, London, 1980.

[105] E. Şaşioğlu, L. M. Sandratskii, and P. Bruno. J. Phys. Condens. Matter **17**, 995 (2005). arXiv:cond-mat/0504679, doi:10.1088/0953-8984/17/6/017.

[106] P. W. Anderson. Solid State Phys. **14**, 99 (1963). doi:10.1016/S0081-1947(08)60260-X.

[107] N. Metropolis and S. Ulam. J. Am. Stat. Assoc. **44**, 335 (1949). doi:10.1080/01621459.1949.10483310.

[108] N. Metropolis. Los Alamos Sci. **15**, 125 (1987).

[109] D. P. Landau and K. Binder. *A guide to Monte-Carlo similations in statistical physics*, volume 3. Cambridge University Press, 2009.

[110] J. C. Walter and G. T. Barkema. Phys. A Stat. Mech. Appl. **418**, 78 (2015). arXiv:1404.0209, doi:10.1016/j.physa.2014.06.014.

[111] N. Metropolis, A. W. Rosenbluth, M. N. Rosenbluth, A. H. Teller, and E. Teller. J. Chem. Phys. **21**, 1087 (1953). doi:10.1063/1.1699114.

[112] R. F. L. Evans et al. J. Phys. Condens. Matter **26**, 103202 (2014). arXiv:1310.6143, doi:10.1088/0953-8984/26/10/103202.

[113] S. Swann. Phys. Technol. **19**, 67 (1988). doi:10.1088/0305-4624/19/2/304.

[114] BESTEC. Berlin.

[115] J. W. Criss and L. S. Birks. Anal. Chem. **40**, 1080 (1968).

[116] L. Spieß, G. Teichert, R. Schwarzer, H. Behnken, and C. Genzel. *Moderne Röntgenbeugung*, volume 2. Vieweg+Teubner, Wiesbaden, 2009. doi:10.1007/978-3-8349-9434-9.

[117] L. G. Parratt. Phys. Rev. **95**, 359 (1954). doi:10.1103/PhysRev.95.359.

[118] S. Foner. Rev. Sci. Instrum. **30**, 548 (1959). doi:10.1063/1.1716679.

[119] J. P. C. Bernards. Rev. Sci. Instrum. **64**, 1918 (1993). doi:10.1063/1.1143977.

[120] C. Leighton, M. Song, J. Nogueés, M. C. Cyrille, and I. K. Schuller. J. Appl. Phys. **88**, 344 (2000). doi:10.1063/1.373665.

[121] T. Tietze et al. New J. Phys. **10**, 055009 (2008). doi:10.1088/1367-2630/10/5/055009.

[122] J. Stöhr. J. Magn. Magn. Mater. **200**, 470 (1999). doi:10.1016/S0304-8853(99)00407-2.

[123] Y. Idzerda et al. Nucl. Instruments Methods Phys. Res. Sect. A Accel. Spectrometers, Detect. Assoc. Equip. **347**, 134 (1994). doi:10.1016/0168-9002(94)91869-4.

[124] M. L. Cohen. Solid State Commun. **107**, 589 (1998). doi:10.1016/S0038-1098(98)00213-0.

[125] J. Hafner, C. Wolverton, and G. Ceder. MRS Bull. **31**, 659 (2006). doi:10.1557/mrs2006.174.

[126] G. K. H. Madsen. J. Am. Chem. Soc. **128**, 12140 (2006). doi:10.1021/ja062526a.

[127] G. Ceder et al. Nature **392**, 694 (1998). doi:10.1038/33647.

[128] J. Greeley, T. F. Jaramillo, J. Bonde, I. B. Chorkendorff, and J. K. Nørskov. Nat. Mater. **5**, 909 (2006). doi:10.1038/nmat1752.

[129] W. Setyawan and S. Curtarolo. Comput. Mater. Sci. **49**, 299 (2010). arXiv:1004.2974, doi:10.1016/j.commatsci.2010.05.010.

[130] A. Jain et al. Comput. Mater. Sci. **50**, 2295 (2011). doi:10.1016/j.commatsci.2011.02.023.

[131] M. Ashton, R. G. Hennig, S. R. Broderick, K. Rajan, and S. B. Sinnott. Phys. Rev. B **94**, 054116 (2016). doi:10.1103/PhysRevB.94.054116.

[132] J. Lee, Y. Ikeda, and I. Tanaka. arXiv (2017). arXiv:arXiv:1702.02734.

[133] S. Sanvito et al. Sci. Adv. **3**, e1602241 (2017). doi:10.1126/sciadv.1602241.

[134] A. Jain et al. APL Mater. **1**, 011002 (2013). doi:10.1063/1.4812323.

[135] The Materials Project. http://www.materialsproject.org.

[136] S. Curtarolo et al. Comput. Mater. Sci. **58**, 227 (2012). doi:10.1016/j.commatsci.2012.02.002.

[137] Aflow - Automatic - FLOW for Material Discovery. (visited on 03/04/2017). http://www.aflowlib.org.

[138] R. H. Taylor et al. Comput. Mater. Sci. **93**, 178 (2014). arXiv:arXiv:1403.2642v2, doi:10.1016/j.commatsci.2014.05.014.

[139] C. B. Barber, D. P. Dobkin, and H. Huhdanpaa. ACM Trans. Math. Softw. **22**, 469 (1996). doi:10.1145/235815.235821.

[140] K. Momma et al. J. Appl. Crystallogr. **44**, 1272 (2011). doi:10.1107/S0021889811038970.

[141] P. Haas, F. Tran, and P. Blaha. Phys. Rev. B **79**, 085104 (2009). doi:10.1103/PhysRevB.79.085104.

[142] S. Kurth, J. P. Perdew, and P. Blaha. Int. J. Quantum Chem. **75**, 889 (1999). doi:10.1002/(SICI)1097-461X(1999)75:4/5<889::AID-QUA54>3.0.CO;2-8.

[143] S. F. Sousa, P. A. Fernandes, and M. J. Ramos. J. Phys. Chem. A **111**, 10439 (2007). doi:10.1021/jp0734474.

[144] P. Pulay. Chem. Phys. Lett. **73**, 393 (1980). doi:10.1016/0009-2614(80)80396-4.

[145] D. A. Garanin. Phys. Rev. B **53**, 11593 (1996). arXiv:cond-mat/9804040, doi:10.1103/PhysRevB.53.11593.

[146] M. Meinert. J. Phys. Condens. Matter **28**, 056006 (2016). arXiv:1601.01522, doi:10.1088/0953-8984/28/5/056006.

[147] K. Diekmann. Investigations on novel cubic ternary antiferromagnetic compounds. Master's thesis, Bielefeld University, 2017.

[148] B. Balke, S. Wurmehl, G. H. Fecher, C. Felser, and J. Kubler. Sci. Technol. Adv. Mater. **9**, 14102 (2008). doi:10.1088/1468-6996/9/1/014102.

[149] S. N. Mishra et al. Hyperfine Interact. **34**, 519 (1987). doi:10.1007/BF02072768.

[150] H. Masumoto and K. Watanabe. J. Phys. Soc. Japan **32**, 281 (1972). doi:10.1143/JPSJ.32.281.

[151] K. Yoshimura, M. Yamada, M. Mekata, T. Shimizu, and H. Yasuoka. J. Phys. Soc. Japan **57**, 409 (1988). doi:10.1143/Jpsj.57.409.

[152] M. Yin and P. Nash. J. Alloys Compd. **650**, 925 (2015). doi:10.1016/j.jallcom.2015.08.054.

[153] H. Okada et al. Appl. Phys. Lett. **92**, 062502 (2008). doi:10.1063/1.2841654.

[154] M. Hiroi et al. J. Korean Phys. Soc. **62**, 2068 (2013). doi:10.3938/jkps.62.2068.

[155] M. Yin and P. Nash. J. Alloys Compd. **634**, 70 (2015). doi:10.1016/j.jallcom.2015.02.089.

[156] S. Mizusaki et al. J. Phys. Conf. Ser. **200**, 52017 (2010). doi:10.1088/1742-6596/200/5/052017.

[157] M. Meinert and M. P. Geisler. J. Magn. Magn. Mater. **341**, 72 (2013). arXiv:1302.2487, doi:10.1016/j.jmmm.2013.04.025.

[158] N. Naghibolashrafi et al. Phys. Rev. B **93**, 104424 (2016). doi:10.1103/PhysRevB.93.104424.

[159] E. Simon, J. G. Vida, S. Khmelevskyi, and L. Szunyogh. Phys. Rev. B **92**, 054438 (2015). doi:10.1103/PhysRevB.92.054438.

[160] S. Khmelevskyi, E. Simon, and L. Szunyogh. Phys. Rev. B **91**, 094432 (2015). arXiv:1501.05116, doi:10.1103/PhysRevB.91.094432.

[161] K. Endo, H. Matsuda, K. Ooiwa, and K. Itoh. J. Phys. Soc. Japan **64**, 2329 (1995). doi:10.1143/JPSJ.64.2329.

[162] S. Mizusaki et al. J. Alloys Compd. **553**, 389 (2013). doi:10.1016/j.jallcom.2012.12.008.

[163] N. Fukatani, H. Fujita, T. Miyawaki, K. Ueda, and H. Asano. J. Korean Phys. Soc. **63**, 711 (2013). doi:10.3938/jkps.63.711.

[164] S. Mizusaki et al. J. Appl. Phys. **105**, 07E513 (2009). doi:10.1063/1.3080561.

[165] H. Danan, A. Herr, and A. J. P. Meyer. J. Appl. Phys. **39**, 669 (1968). doi:10.1063/1.2163571.

[166] R. Carpenter, N. C. Cramp, and K. O'Grady. IEEE Trans. Magn. **48**, 4351 (2012). doi:10.1109/TMAG.2012.2200246.

[167] C. C. Chang. Surf. Sci. **25**, 53 (1971). doi:10.1016/0039-6028(71)90210-X.

[168] M. Fecioru-Morariu, S. R. Ali, C. Papusoi, M. Sperlich, and G. Güntherodt. Phys. Rev. Lett. **99**, 097206 (2007). doi:10.1103/PhysRevLett.99.097206.

[169] W. F. Brinkman, R. C. Dynes, and J. M. Rowell. J. Appl. Phys. **41**, 1915 (1970). doi:10.1063/1.1659141.

[170] O. E. Taurian, M. Springborg, and N. E. Christensen. Solid State Commun. **55**, 351 (1985). doi:10.1016/0038-1098(85)90622-2.

[171] J. Faure-Vincent et al. Appl. Phys. Lett. **82**, 4507 (2003). doi:10.1063/1.1586785.

[172] A. B. Gokhale and R. Abbaschian. Bull. Alloy Phase Diagrams **11**, 460 (1990). doi:10.1007/BF02898261.

[173] G. Kádár and E. Krén. Int. J. Magn **1**, 143 (1971).

[174] A. Sugihara, K. Suzuki, S. Mizukami, and T. Miyazaki. J. Phys. D: Appl. Phys. **48**, 164009 (2015). doi:10.1088/0022-3727/48/16/164009.

[175] W. H. Butler. Sci. Technol. Adv. Mater. **9**, 014106 (2008). doi:10.1088/1468-6996/9/1/014106.

[176] J. Jeong et al. Nat. Commun. **7**, 10276 (2016). doi:10.1038/ncomms10276.

[177] H. Dohmeier. *Herstellung und Charakterisierung von $Mn_{3+x}Ge$ in dünnen gesputterten Schichten*. Diploma thesis, Bielefeld University, 2016.

[178] M. Glas. *Mn-based Heusler Compounds and CoFeB Thin Films with Perpendicular Anisotropy*. PhD thesis, Bielefeld University, 2015.

[179] N. Nagaosa, J. Sinova, S. Onoda, A. H. MacDonald, and N. P. Ong. Rev. Mod. Phys. **82**, 1539 (2010). arXiv:0904.4154, doi:10.1103/RevModPhys.82.1539.

[180] C. T. Chen et al. Phys. Rev. Lett. **75**, 152 (1995). doi:10.1103/PhysRevLett.75.152.

[181] M. Meinert et al. Phys. Rev. B **84**, 2 (2011). arXiv:arXiv:1107.0887v2, doi:10.1103/PhysRevB.84.132405.

[182] M. Meinert. *Ferrimagnetic Heusler Compounds - From first principles to thin films*. PhD thesis, Bielefeld University, 2011.

[183] P. E. Blöchl, O. Jepsen, and O. K. Andersen. Phys. Rev. B **49**, 16223 (1994). doi:10.1103/PhysRevB.49.16223.

[184] G. E. Bacon and J. S. Plant. J. Phys. F Met. Phys. **3**, 2003 (1973). doi:10.1088/0305-4608/3/11/020.

[185] M. Meinert, T. Hübner, J. Schmalhorst, G. Reiss, and E. Arenholz. J. Appl. Phys. **114**, 113908 (2013). arXiv:1307.4734, doi:10.1063/1.4821972.

[186] X. D. Tang et al. Appl. Phys. Lett. **97**, 242513 (2010). doi:10.1063/1.3526377.

[187] T. Gasi, A. K. Nayak, M. Nicklas, and C. Felser. J. Appl. Phys. **113**, 17E301 (2013). doi:10.1063/1.4794979.

[188] L. Zhang, E. Brück, O. Tegus, K. H. J. Buschow, and F. R. De Boer. Phys. B **328**, 295 (2003). doi:10.1016/S0921-4526(02)01853-7.

[189] L. Zhang, E. Brück, O. Tegus, K. H. J. Buschow, and F. R. De Boer. J. Alloys Compd. **352**, 99 (2003). doi:10.1016/S0925-8388(02)01116-7.

[190] K. R. A. Ziebeck and P. J. Webster. Philos. Mag. **34**, 973 (1976). doi:10.1080/00318087608227722.

[191] T. Roy and A. Chakrabarti. AIP Conf. Proc. **1665**, 090036 (2015). doi:10.1063/1.4918016.

[192] I. Galanakis. Phys. Rev. B **71**, 012413 (2005). arXiv:cond-mat/0407560, doi:10.1103/PhysRevB.71.012413.

Danksagungen
Acknowledgements

Diese Arbeit wurde direkt wie auch indirekt von vielen Leuten und Organisationen unterstützt, welche sehr zum Erfolg meiner Arbeit beigetragen haben. Daher möchte ich die Möglichkeit nutzen, diesen meinen Dank auszudrücken.

This work has been supported directly and indirectly by a lot of people and organizations greatly contributing to the success of this thesis. Thus, I'd like to take the chance to acknowledge these.

Meine Arbeit wurde finanziell durch das Seventh Framework Programme (FP7 / 2007-2013) der Europäischen Union im Rahmen des Projektes HARFIR (NMP3-SL-2013-604398) unterstützt. Ich möchte allen beteiligten Partnern aus York (UK), Konstanz (GER), Budapest (HU), Tohoku (JP) und Tsukuba (JP) für die angenehme Zusammenarbeit und den regen Austausch danken.

The research leading to these results has received funding from the European Union Seventh Framework Programme (FP7/2007-2013) under grant agreement no. NMP3-SL-2013-604398 (HARFIR). I would like to express my gratitude to all collaborating partners from York (UK), Konstanz (GER), Budapest (HU), Tohoku (JP), and Tsukuba (JP) for the pleasant collaboration and the active exchange.

Zunächst möchte ich GÜNTER REISS für die Betreuung, Anleitung und Begutachtung meiner Arbeit danken. Seine gelassene Art hat an vielen Stellen die nötige Ruhe eingebracht, um Probleme zu bewerkstelligen. Insbesondere möchte ich für die Möglichkeit der zahlreichen Reisen danken, die viel Inspiration durch Einblick in unterschiedliche Arbeitsgruppen, Labore und Konferenzen gebracht haben. Weiterhin danke ich ihm für die zweiwöchige Freistellung während derer ich an einer Fortbildung am Institut der Feuerwehr in Münster teilnehmen konnte.

At first, I would like to express my gratitude to GÜNTER REISS *for supervising, guiding and reviewing my work. His calm character has brought the necessary ease to solve problems at many points. Especially, I would like to thank for the possibility of numerous journeys, which inspired me a lot with impressions from different workgroups, laboratories and conferences. Furthermore, I'd like to thank*

him for his agreement of a two-week leave of absence, which allowed me to attend a further education at the Institut der Feuerwehr in Münster.

In gleicher Art danke ich THOMAS DAHM, der sich bereit erklärt hat, sich meiner Arbeit als Zweitgutachter anzunehmen.

Similarly, I thank THOMAS DAHM*, who agreed to review my thesis as well.*

Mein großer Dank gilt MARKUS MEINERT, der effektiv meine Arbeit von fachlicher Seite betreut hat. Die zahllosen Gespräche über Probleme, Entwicklungen neuer Methoden und Diskussionen von Ergebnissen sind unerlässlich für diese Arbeit gewesen.

My large gratitude goes to MARKUS MEINERT*, who effectively supervised my work from the technical point of view. The countless conversations about problems, developments of new methods, and discussions of recent results are indispensable for this thesis.*

Kevin Diekmann danke ich für die tolle Zusammenarbeit im Bereich der DFT Berechnungen. Durch seine beigesteuerte Arbeit konnten wir die Reichweite an abgedeckten Verbindungen deutlich erweitern und wertvolle Erkenntnisse sammeln.

I thank Kevin Diekmann for the nice co-work on DFT calculations. Due to the work he contributed we were able to siginificantly increase the range of investigated compounds and obtain some valuable insights.

Ich möchte JAN SCHMALHORST für die spannende Zusammenarbeit danken, aus der ich eine Menge gelernt habe. Anzuführen ist hier der beispiellos holprige Aufbau des VSMs (verursacht durch den Hersteller) und insbesondere die Strahlzeiten an der Advanced Light Source in Berkeley.

I would like to thank JAN SCHMALHORST *for the exciting cooperation from which I've learned a lot. To mention are the unprecedentedly rough establishment of the VSM (caused by the manufacturer) and especially the beamtimes at the Advanced Light Source in Berkeley.*

Um niemanden versehentlich zu vergessen möchte ich allen Mitarbeitern und Ehemaligen in der Arbeitsgruppe D2 danken für eine einmalige Arbeits- und

Gruppenathmosphäre in den letzten Jahren. Danke für immer offene Ohren, zahlreiche Diskussionen, Hilfestellungen, und nicht zuletzt die notwendigen Wartungsarbeiten an Laborgeräten und Inventar.

To prevent forgetting someone accidentally, I would like to thank all coworkers and former members of the workgroup D2 for a unique work and group atmosphere during the last years. Thank you for always open ears, numerous discussions, assistances, and last but not least the necessary maintenance of laboratory equipment and inventory.

ELKE ARENHOLZ und ihren Mitarbeitern an der Advanced Light Source in Berkeley[1] möchte ich für die absolut reibungslosen Strahlzeiten und die entsprechende Unterstützung während dieser danken.

ELKE ARENHOLZ *and her coworkers at the Advanced Light Source in Berkeley have my thanks for the absolutely smooth beamtimes and their corresponding support during our visits.*

Ich danke TEODOR HUMINIUC von der Universität York für die Präparation und Durchführung der HR-TEM Querschnittanalysen meiner Proben, welche in dieser Arbeit enthalten sind.

I thank TEODOR HUMINIUC *from the University of York for cross section preparation and HR-TEM analysis of my samples, which is included in this thesis*

Mein besonderer Dank gilt allen, die während meiner zahlreichen Reisen sich bereit erklärt haben, für meine Tiere zu sorgen. Ohne euch hätte ich viele davon einfach nicht antreten können!

My special thanks go to all the people who agreed to care for my pets during my countless journeys. Without you, I wouldn't have been able to attend a lot of them!

Unerlässlich für solch eine Arbeit sind die fleißigen Korrekturleser, die mit ihren Anmerkungen für den letzten Schliff gesorgt haben. Einen großen Dank dafür, dieses umfangreiche Werk, mitunter völlig fachfremd, gelesen zu haben!

[1] The Advanced Light Source is supported by the Director, Office of Science, Office of Basic Energy Sciences, of the U.S. Department of Energy under Contract No. DE-AC02-05CH11231.

Indispensable for such a thesis are the diligent proofreaders, who provided the finishing touches. A big thanks for reading this considerable amount of work, even without special knowledge about the content!

Mein wichtigster Dank gilt meiner Freundin, die mir wirklich zahllose Nacht- und Wochenendschichten im Labor erleichtert und mir Vieles abgenommen hat. Ohne die Unterstützung im Hintergrund hätte ich die notwendige Zeit und Konzentration für die Arbeit an vielen Stellen nicht aufbringen können und wäre oft an meine Grenzen geraten. Danke.

My most important gratitude I'd like to express to my girlfriend, who seriously facilitated many night and weekend shifts for me in the lab and relieved me of many things. Without this support in the background I wouldn't have had the necessary time and concentration to focus on my work, and would've faced my limits at many points. Thank you.